UNIVERSIDADE DE LISBOA
FACULDADE DE CIÊNCIAS
DEPARTAMENTO DE FÍSICA

PET/MR brain connectivity of brain tumour patients

Ana Carina Pereira Mendes

Mestrado Integrado em Engenharia Biomédica e Biofísica
Perfil em Engenharia Clínica e Instrumentação Médica

Dissertação orientada por:
Dr. Hugo Alexandre Ferreira, Instituto de Biofísica e Engenharia Biomédica, Departamento de Física da Universidade de Lisboa, Lisboa, Portugal
Dr. Ana-Maria Oros-Peusquens, Institute of Neurosciences and Medicine (INM-4), Forschungszentrum Jülich, Jülich, Germany

2016

Acknowledgements

First my gratitude goes to my supervisors Dr. Ana-Maria and Dr. Hugo Ferreira for the patience, guidance and support throughout this thesis. The enthusiasm and optimism showed were contagious and decisive during this journey.

To Prof. Jon Shah, I would like to express my gratitude for welcoming me into the Institute of Neuroscience and Medicine, for the words and tutelage.

I would like to express my special appreciation to the Institute of Neuroscience and Medicine at Forschungszentrum Jülich for providing me with this opportunity to develop my thesis and successfully finish my master. A special thanks to Nuno da Silva and Liliana Caldeira for the help with getting around the institute and Germany.

I would like to express my gratitude to André Ribeiro for the help provided during this whole work using the MIBCA toolbox and, for all the suggestions and tips.

I would also like to thank Dr. Karl-Josef Langen, Dr. Carolin Weiss, and remaining co-authors, André Ribeiro, Dr. Ana-Maria, Dr. Hugo Ferreira and Prof. Shah, for all the support and suggestions for the two communications resultant from this work.

To my mother and grandmother, thank you for believing in me and support me all the way through it.

To my friends, for all the support, and encouragement words when I most needed them. A special thank you to Carina Ramalho and Carla Lopes for their friendship and cheerfulness. Another special thank you to João Belbut, for the patience and support when I most needed, and that thrived me to always be the very best I can be.

And of course, thank you Ana Moital, Andreia Gaspar and Diogo Duarte. Without you these last years would have passed by, but it would not have been the same. It was a pleasure to have shared five years of my life learning alongside all of you.

The funding received from the Erasmus Programme was essential for this project. For that, I would like to thank Lisbon University for the funding. Research supported by the Edmond J. Safra Philanthropic Foundation, and by the Fundação para a Ciência e Tecnologia (FCT) and Ministério da Ciência e Educação (MCE) Portugal (PIDDAC) under grants UID/BIO/00645/2013 and PTDC/SAU-ENB/120718/2010.

Resumo

Traumas ou lesões cerebrais podem levar à reorganização/ rearranjo ou até destruição de ligações anatómicas e funcionais, o que pode levar a alterações do comportamento de regiões e redes locais. Os tumores cerebrais podem ser classificados como benignos ou malignos. Podem começar diretamente no cérebro ou resultar da invasão de tecidos circundantes através de metástases. O prognóstico e sobrevivência dos pacientes depende fortemente do tipo de tumor, e altura em que o diagnóstico é realizado, bem como da avaliação e examinação médica. Os exames que costumam ser realizados incluem: imagem por ressonância magnética (MRI, acrónimo inglês de *Magnetic Resonance Imaging*) e tomografia por emissão de positrões (PET, acrónimo inglês de *Positron Emission Tomography*). Estes permitem a caracterização tumoral (como por exemplo, a localização, tamanho, estrutura e fornecimento vascular). O uso de técnicas como a imagem por tensor de difusão (DTI, acrónimo inglês de *Diffusion Tensor Imaging*) e ressonância magnética funcional (fMRI, acrónimo inglês de *functional MRI*) permitem o estudo da substância branca e o mapeamento funcional. Estudos com DTI permitem identificar e definir a organização da substância branca, através da aplicação de algoritmos de tractografia, embora existam limitações (ocorrem nomeadamente em regiões de cruzamento de fibras). Com recurso a fMRI os médicos conseguiram proceder ao mapeamento de diferentes regiões cerebrais de acordo com a atividade que codificam, o que inclui a identificação, no córtex, de áreas responsáveis por uma dada tarefa. Este tipo de conhecimento é importante não só para o planeamento cirúrgico, mas também para um melhor prognóstico do doente em causa.

Com o trabalho desenvolvido nesta tese pretendeu-se estudar o efeito de tumores cerebrais, nomeadamente do glioblastoma multiforme, na conectividade cerebral, visto não ser um tópico muito explorado. Estudos realizados no que diz respeito a efeitos da presença de tumores na conectividade cerebral têm sido feitos através do estudo da influência local ou em redes conhecidas, como a da linguagem. Para tal, dados de técnicas como magnetoencefalografia (MEG, acrónimo do inglês *Magnetoencephalography*), fMRI, estimulação magnética transcraniana (TMS, acrónimo do inglês *Transcranial Magnetic Stimulation*) e eletroencefalografia (EEG, acrónimo do inglês *Electroencephalography*) foram usadas para obtenção de informação relacionada com alterações funcionais e DTI para alterações estruturais. No entanto, o estudo do efeito de tumores cerebrais malignos em redes de conectividade por todo o cérebro continua a ser um tópico pouco explorado.

Dado o objectivo do trabalho a desenvolver nesta tese, um grupo de pacientes com glioblastoma multiforme foi selecionado e estudado em comparação a um grupo de sujeitos saudáveis. Todos os dados foram pré-adquiridos no Forschungszentrum Jülich e no Hospital de Colónia, durante os últimos anos, e os pacientes receberam tratamento adequado. Para a análise destes dados a Multimodal Imaging Brain Connectivity Analysis (MIBCA) toolbox para MatLab foi utilizada. Os objetivos deste projeto foram: (1) usar a MIBCA para o pré-processamento dos dados multimodais e fazer a respetiva visualização de dados; (2) avaliar alterações significativas em padrões de conectividade dentro do grupo de controlo (verificação da variabilidade inter-sujeito); e (3) avaliar alterações de padrões de conectividade em regiões locais e mais distantes nos pacientes, relacionadas com a presença do tumor.

Para realizar a análise proposta, nove sujeitos com glioblastoma (5 no hemisfério esquerdo; 5 homens; pacientes com lesões do lado esquerdo com 53 ± 10 anos, e do lado direito com 42 ± 15 anos) foram submetidos a aquisições de MRI e PET simultâneas usando um sistema de MRI MAGNETOM TRIO de 3T com um BrainPET insert. O grupo de controlo foi constituído por 22 sujeitos saudáveis (11 homens; grupo com 59 ± 6 anos; apenas foram submetidos a aquisições de MRI). A aquisição simultânea destas modalidades permite o cruzamento da informação anatómica e estrutural provenientes do MRI com a informação molecular do exame PET. Imagens com ponderação T1, DTI e PET com $18^F - fluoro - etil - L - tirosina$ ($18^F - FET$) foram adquiridas e a MIBCA foi utilizada para o pré-processamento automático dos dados, permitindo a obtenção de diferentes métricas de imagem/ conectividade. Para fins do presente trabalho, as métricas estudadas incluíram: espessura cortical (CtxT, do inglês *cortical thickness*) a partir dos dados ponderados em T1; difusibilidade média (MD do inglês *mean difusivity*), fração de anisotropia (FA, do inglês *fractional anisotropy*), grau do nó (Deg, do inglês *node degree*), coeficiente de agrupamento (ClusC, do inglês *clustering coefficient*) e valores de pares de regiões-de-interesse (ROI) de resultados de tractografia; e valor padronizado de captação (SUV, do inglês *standardized uptake value*) a partir dos dados de PET. Dos dados de SUV é possível obter informação sobre a captação dos tecidos do radiofármaco usado (é de esperar que regiões tumorais apresentem um maior valor já que existe maior captação, dada a especificidade do radiofármaco usado), sendo por isso importante para definir a localização do tumor. Dados referentes a uma avaliação de diferenças intra-hemisféricas e de dados referentes ao cérebro completo foram avaliados através de duas abordagens: com o grupo de controlo composto por todos os sujeitos e um grupo de controlo com o género correspondente. Os resultados foram avaliados em conectogramas. As matrizes de conectividade e métricas de imagem foram estudadas em regiões circundantes às lesões, identificadas pelo contraste nas aquisições de MRI, e confirmadas pelo aumento de SUV.

Valores aumentados de SUV foram identificados em regiões relacionadas com a presença de lesões tumorais em todos os pacientes, como seria de esperar. Verificaram-se alterações na conectividade estrutural não relacionadas exclusivamente com regiões peritumorais, mas também com regiões mais distantes, para todos os pacientes estudados. Alterações nos valores de MD e FA foram observados em regiões perilesionais que poderão ser explicadas pelo efeito de massa/ volume provocado pela presença do tumor. Algumas destas alterações podem também ser explicadas por alterações fisiológicas locais, que podem levar ao aumento ou redução da produção de mielina. Por sua vez, esta poderia levar a alterações na constituição da membrana celular dos axónios, o que levaria a alterações na facilidade do movimento das moléculas de água através da membrana (alteração da permeabilidade). Em alguns dos casos analisados, um número aumentado de fibras numa dada conexão, associado a um valor baixo de ClusC foi também identificado, o que pode ser explicado por fortalecimento das conexões com um menor número de regiões, consequência da destruição neuronal em regiões peritumorais.

Os achados reportados por este estudo sugerem que a infiltração, característica dos glioblastomas, poderá levar não só a alterações locais, mas também a alterações em ligações estruturais mais distantes. Este estudo mostrou também que a toolbox MIBCA se mostra como uma ferramenta útil para a investigação e a construção de conhecimento quanto à organização estrutural e funcional do cérebro de pacientes com tumores cerebrais, usando uma perspetiva não invasiva com dados multimodais de imagem.

No que diz respeito a melhorias a aplicar a esta abordagem, dever-se-ia rever a aplicação das técnicas de segmentação e parcelização, de forma a evitar uma má classificação de tecidos e regiões, nomeadamente na localização de tumores. Informação não correcta proveniente de uma segmentação pobre, e consequente má parcelização, pode comprometer conclusões retiradas no

que diz respeito a alterações na conectividade resultantes da presença de tumores. Por forma a melhorar as métricas de conectividade retiradas dos dados de difusão, dados de imagem por tensor de curtose (DKI, acrónimo do inglês Diffusion Kurtosis Imaging) deveriam ser incluídos. Dada a tractografia obtida através de dados de DKI nos fornecer melhores resultados em regiões com sobreposição de fibras face a DTI (uma das limitações já referidas), espera-se que a caracterização de conectividade cerebral melhore. No que diz respeito a estudos com tumores cerebrais, a presença de edema influencia os valores obtidos de FA (retirados a partir de DTI), uma vez que o elevado conteúdo em água da região irá levar a redução de anisotropia e, consequentemente a exclusão de fibras que não são identificadas aquando da construção dos mapas de tractografia.

Em última análise, o estudo de perfis de conectividade cerebral em regiões específicas no cérebro poderia fornecer informação importante para o planeamento cirúrgico e qual a abordagem a tomar dada a situação. Desta forma poder-se-iam prevenir sequelas devidas à excisão de demasiado tecido circundante saudável. Poder-se-iam ainda estudar perfis de conectividade característicos de determinados tumores e com essa informação criar marcadores que classifiquem diferentes tipos de gliomas em momentos iniciais de desenvolvimento.

Palavras-chave: Gliobastoma, conectividade cerebral, métricas de conectividade, imagem de ressonância magnética, tomografia por emissão de positrões

Abstract

Traumatic events or lesions can lead to the reorganization/ rearrangement or even disruption of anatomical and functional connections, thus, leading to changes in the behaviour of brain regions and networks. This thesis presents a first approach on the study of whole-brain connectivity of brain tumour patients using the Multimodal Imaging Brain Connectivity (MIBCA) toolbox.

Nine patients with glioblastoma (5 left hemisphere) underwent simultaneous magnetic resonance imaging (MRI) and dynamic positron emission tomography (PET) scans using a 3T MRI scanner with a BrainPET insert. The control group comprised 22 healthy subjects (only MRI was performed). Volumetric T1-weighted, diffusion tensor imaging (DTI), and dynamic O(2-Fluorine-18-Fluoroethyl)-L-Tyrosine ($[^{18}F]$-FET) PET scans were acquired. The Multimodal Imaging Brain Connectivity Analysis (MIBCA) toolbox was used to automatically pre-process MR-PET data and to derive imaging and connectivity metrics from the multimodal data, that is, cortical thickness (CtxT) from T1-weighted data; mean diffusivity (MD), fractional anisotropy (FA), node degree (Deg), clustering coefficient (ClusC) and pairwise region-of-interest (ROI) fibre tracking from DTI data; and standardized uptake value (SUV) from the PET data. Interhemispheric differences as well as whole-brain connectivity were assessed for both patients and controls, with the whole group and gender-matched data. Results were visualised in connectograms, and both structural connectivity matrices and imaging metrics were studied in regions surrounding lesions, identified by the contrast enhanced MRI, and confirmed by increased SUV.

Increased SUV values were found in tumour regions in all patients investigated in this study. Changes in structural connectivity involving not only the tumour surroundings but more spatially distant regions were found for all patients. FA and MD alterations were observed in perilesional regions which may result from fibre packing due to tumour volume effect. In some cases, an increased number of fibres and decreased clustering coefficient value was identified which implies strengthening of connections with fewer regions.

These findings suggest that tumour infiltration may lead to alterations in both local and more distant structural connections. This study has shown that the MIBCA toolbox provides a suitable tool to gain further insight into the structural and functional connectivity of patients with brain tumours using a multimodal imaging approach.

Keywords: Glioblastoma, brain connectivity, connectivity metrics, magnetic resonance imaging, positron emission tomography

Contents

List of Figures

List of Tables

List of Abbreviations

[^{18}F]-FDG Fluorine 18 Flurodeoxyglucose. 15, 16, 18

[^{18}F]-FET O(2-Fluorine-18-Fluoroethyl)-L-Tyrosine. 17, 18, 25, 27

ADC apparent diffusion coefficient. 12, 13

AI asymmetry index. 28, 30, 34, 35

ClusC clustering coefficient. 25, 31, 32, 34–42, 44–52

CT computed tomography. 5

CtxT cortical thickness. 25, 26, 31, 32, 34–42, 44–50, 52

Deg node degree. 25, 31, 32, 34–42, 44–49, 52

DKI diffusion kurtosis imaging. 14, 55

DTI diffusion tensor imaging. 1, 13–15, 22, 23, 25, 26, 32, 34, 35, 44, 45, 52, 55

DWI diffusion weighted imaging. 11–13

EEG electroencephalography. 1, 3, 22

FA fractional anisotropy. 13–15, 23, 25, 26, 31, 32, 34–42, 44–51, 53, 55

FID free induction decay. 9, 10

fMRI functional magnetic resonance imaging. 1, 22, 23

GE gradient echo. 10

GRE gradient recalled echo. 10

LOR line of response. 17

MD mean diffusivity. 13, 25, 26, 31, 32, 34–42, 44–51, 53, 55

MEG magnetoencephalography. 1, 22, 23

MIBCA Multimodal Imaging Brain Connectivity Analysis. 1, 2, 25–27, 55

MPRAGE magnetization prepared rapid acquisition gradient echo. 10, 11, 25

MR magnetic resonance. 9, 10, 23, 25

MRI magnetic resonance imaging. 1, 3–5, 7–11, 25, 55

NMR nuclear magnetic resonance. 7

PET positron emission tomography. 1, 3, 5, 7, 15–17, 23, 25–27, 55

RA relative anisotropy. 13

RF radiofrequency. 9, 10

ROI region-of-interest. 25, 28, 30, 34, 35, 44, 45

SD standard deviation. 25, 27–29, 31–33

SE spin echo. 10

SUV standardised uptake value. 25, 26, 34, 35, 44, 45

T1-w T1-weighted. 5, 25, 26

T2-w T2-weighted. 12, 13

TE echo time. 10

TR repetition time. 10

Overview

Brain tumours are characterised by an abnormal tissue growth. Their formation can start directly in the brain or result from invading surrounding tissues and metastasis. Tumours can be classified as benign or malignant. The latter are more aggressive, often with a faster growing rate [1].

Prognosis and survival depend on multiple factors including its type and time of diagnosis. Diagnosis is often challenging since some of the signs and symptoms are shared with other illnesses. Additionally, it depends greatly on the physician evaluation and examination. Typically used neuroimaging techniques include magnetic resonance imaging (MRI) and positron emission tomography (PET), enabling tumour characterisation. This characterisation includes location, size, structure and vascular supply, which are valuable information for the choice of treatment and, in some cases, surgical planning [2].

Diffusion tensor imaging (DTI) and functional magnetic resonance imaging (fMRI) are two MRI techniques that allow the study of white matter and functional mapping, respectively. White matter studies done with DTI allow the assess to white matter tracts organisation, through the application of tractography algorithms, which make use of the anisotropic water diffusion [3]. However, the application of these algorithms presents some challenges on its usage, since most struggle in the definition of fibre overlapping regions [4, 5]. With fMRI, physicians are capable of identifying both regions related to rest and task-based activity, enabling the mapping of the cortex areas responsible for a certain function. This knowledge improves the capability to plan for and foresee the outcome after a surgical intervention [3].

Performed studies aim to understand brain tumour effects in the patient at a physical and cognitive level [6–8]. Researchers are working towards understanding brain circuitry, and in what way a lesion, such as a brain tumour, affects it in the hopes to allow for better surgical planning and prediction of resultant sequelae from the applied treatment (ie. tumoural resections) [9, 10]. However, most of these studies only look at specific functional areas using magnetoencephalography (MEG), electroencephalography (EEG) and fMRI to detect eventual changes in normal brain activity, and DTI for structural changes [6–8].

Thesis Aim

The overall aim of the work developed during the construction of this thesis was to assess the effect of brain tumours in whole brain connectivity, since it is a topic that has not yet been consistently explored. In order to do so, a group of glioblastoma multiforme patients was selected and studied along side a group of healthy subjects. Used data had already been scanned at Forschungszentrum Jülich and Cologne Hospital over the last years, and the patients received proper treatment. For the data processing and analysis, the Multimodal Imaging Brain Connectivity Analysis (MIBCA) toolbox [11] was used.

To sum up, with this project I aimed to:

- Test the viability of MIBCA toolbox usage to pre-process multimodal data and visualise results;
- Evaluate significant changes on connectivity patterns within a group of healthy subjects (assess subject variability);
- Evaluate changes of connectivity patterns in both local and more distant regions, related to the tumour.

Thesis Outlook

This thesis is divided in 7 chapters as described below.

In chapter 1 a brief introduction to human brain anatomy and to brain tumours, specifically glioblastoma multiforme, is shown.

In chapter 2 an introduction to the different imaging modalities is shown. This chapter is subdivided in two sections with the description of MRI and PET modalities. The first section presented an introduction to MRI principles and sequences used for the data acquisition. The second section presented an introduction to PET principles and used radiotracer.

Chapter 3 presented an overall introduction to connectomics and is divided in 4 sections. The first three presented the background necessary to introduce the work developed in this thesis regarding connectivity. The fourth section discussed findings in the literature regarding the influence of tumours/ lesions in the brain connectivity.

In chapter 4 a description of the used methodologies is shown within 3 sections. In the first, a description of the control and patients' sample is provided. In the second and third sections the method for the evaluation of differences and its application was presented, respectively.

Chapter 5 presented results and considerations regarding variability in control subjects with respect to all subjects and the gender-based groups. Glioblastoma patients' analysis was done in chapter 6, with a small introduction and three different sections. The first and second sections presented the individual patient analysis regarding intrahemispheric and whole-brain differences, respectively. In the last section an overview about most relevant findings was given.

Finally, the last chapter presented a summary of the most relevant findings. It also provided the limitations and future perspectives of this work.

1. The human brain

The telencephalon represents the larger portion of the human brain and consists in an upper region, related to the vault of the skull, and a lower one, which corresponds to its base. It is divided into two hemispheres, by the inter-hemispheric fissure, whose connection is guaranteed by fibres present in the corpus callosum [12, 13]. Besides this portion, the brain is comprised of by the cerebellum and brainstem. The cerebellum is responsible by the equilibrium, posture and voluntary movements, and the brainstem houses the cranial nerves nuclei [12–14].

1.1. Neuroanatomy basics

The cerebral cortex is the largest portion of the hemispheric brain and represents the highest level of the central nervous system. It is comprised of grey matter and its surface area is augmented by the existence of gyri (convolutions), which are separated by fissures or sulci (see figure 1.1)[12].

Information from all over the body is carried to the brain and processed in specific regions of the cortex, which enables its differentiation according to the type of information processed. The classification of these regions can be done using techniques such as EEG, PET and MRI [12, 14].

Division of the cerebral cortex is done into lobes: frontal, parietal, temporal and occipital (see figure 1.1). The frontal lobe is related to reasoning, planning, speech, movement, emotions and problem solving functions. The parietal lobe is related to movement, orientation, recognition and perception of stimuli. The temporal lobe is related to perception and recognition of auditory stimuli, memory and speech and finally the occipital lobe is related to visual processing. Functional regions intimately related to movement include the primary motor, premotor and supplementary motor areas found in the frontal lobe, whereas the primary, secondary and somesthetic association areas are found in the temporal lobe [14].

The limbic system (often referred as the "emotional brain") can be found deep inside the cerebrum. It comprises the thalamus, hypothalamus, amygdala and hyppocampus and is responsible for emotional behaviour [12, 14].

1.2. Brain tumours

Brain tumours are, by definition, a mass or abnormal growth of cells in or close to the brain. Intracranial tumours are most frequently represented by metastases and primary brain tumours, and are capable of altering fiber pathways [2, 16]. The growth rate can vary greatly, and this

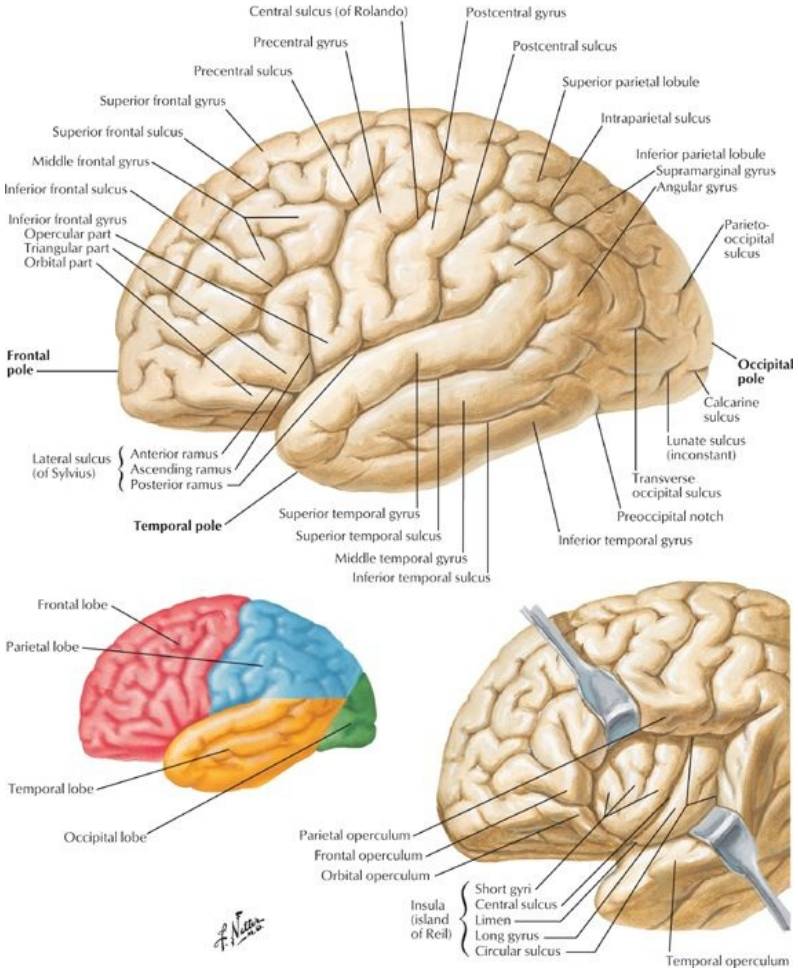

Figure 1.1.: Hemispheric cortex and lobe division of the hemispheric brain. In pink the frontal lobe, in blue the parietal lobe, in orange the temporal lobe and in green the occipital lobe [15].

factor in conjunction with the tumour location determines how it will affect the function of the nervous system. Treatment is also dependent on the type, size and tumour location [2, 16].

For the study presented on this thesis, data from patients with glioblastoma multiforme were assessed.

1.2.1. Glioblastoma multiforme

Primary glioblastoma multiforme (malignant glioma World Health Organisation [WHO] grade IV [17]) is the most frequent invasive brain tumour [18, 19]. Median survival for this type of tumour is around 12 to 14 months [20, 21]. Usually they are formed in the white matter and become very large without the patient showing any symptoms. These tumours show a highly invasive growth pattern, being characterized as an inhomogeneous mass with a hypodense center and a variable ring of enhancement surrounded by oedema in contrast-enhanced MRI scans [21, 22]. Due to this fact, the intraoperative definition of the tumour margin is usually difficult and functional tissue adjacent to the tumour bulk is at risk [21]. In the tumour, small areas of necrotizing tissue, surrounded by anaplastic cells (undifferentiated cells, characteristic of malignant neoplasms), are also identified as well as an increase of the blood flow in the region due to the presence of hyperplastic blood vessels. The mass effect caused by the presence of tumour and oedema may

not only compress the ventricles but also block the normal flow of cerebospinal fluid, leading to a builtdup of pressure (hydrocephalus) [21], as well as changes in local and distant connectivity patterns [6]. In figure 1.2 we have an example of a T1-weighted (T1-w) scan of a patient with glioblastoma multiforme.

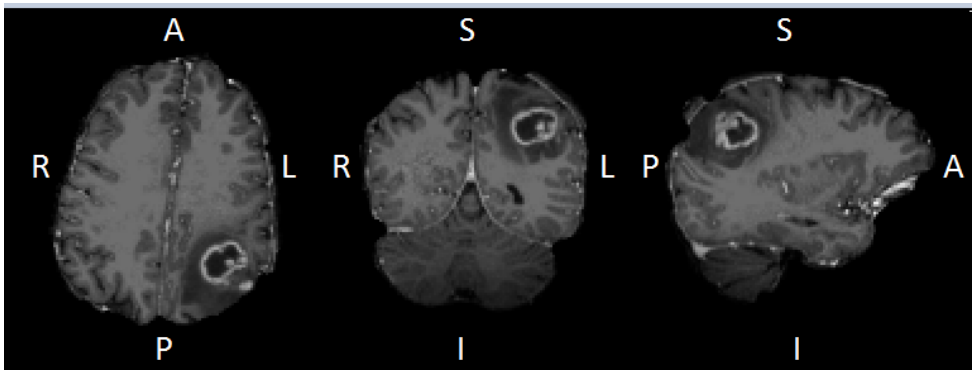

Figure 1.2.: Contrast-enhanced T1-weighted axial, coronal and sagittal cuts of a patient with glioblastoma multiforme located in the left hemisphere (L-left, R - right, A - anterior, P - posterior, I - inferior, S - superior). In this image we can see an area of decreased density (necrotic tissue) surrounded by a bright ring from concentration of the enhancing contrasted dye, which gives us the tumour location. The low signal region surrounding the lesion corresponds to oedema presence.

Diagnosis makes use of imaging techniques, including contrast-enhanced MRI and computed tomography (CT), and PET, plus, a histological study of the affected tissue through biopsy or by analysis of the excised tumour mass during surgery [2, 21, 23].

Surgery is the first line of treatment, where the surgeon tries to remove as much tumour tissue as possible, followed by radiotherapy or chemotherapy in order to kill the remaining tumour cells, or to slow the growth rate when surgery is not possible. Since it is crucial for quality of life, adjuvant treatment and overall resection to achieve not only gross survival but also to preserve brain function [2], exact knowledge of important inter- and intrahemispheric connections in the tumoural and peritumour regions should be very helpful for the surgeon [19, 20].

2. Medical imaging

Medical imaging comprises a group of non-invasive techniques that allow the obtention of images from the human body. This enables physicians to improve their diagnosis which leads to better treatment choices and surgical planning. Besides direct contribution in the provided health care, medical imaging has also added value to present knowledge concerning the human body, namely about the brain. Nowadays, a wide range of medical imaging methods are available, including MRI and PET, whose basic concepts will be introduced in this chapter.

2.1. Magnetic Resonance Imaging

MRI or nuclear magnetic resonance (NMR) is a chemical analytical technique developed under the NMR principle described by Eduard PurcelL and Felix Bloch in 1946 [24]. Since it uses no ionisation radiation, and it has the capability of providing high resolution morphological images, with high contrast sensitivity, it has been pointed as an election technique for use in clinical practice [25]. It uses the hydrogen atom magnetic properties (such as the quantum number spin), due to the large amount of water present in the human body [26]. Nowadays, with the technological advances and novel techniques development, simple changes on acquisition parameters enable the visualisation of distinct structures.

2.1.1. Basic principles

MRI makes use of the body magnetic properties in order to produce detailed images. Due to its abundance in live tissue, the hydrogen nucleus is used for imaging purposes. Hydrogen, a single proton nucleus, can be approximated to a small magnet, a magnetic dipole (with a north-south pole), spinning in its axis. This spinning behaviour is commonly referred as spin, a form of angular momentum. These characteristics give the hydrogen nuclei an associated magnetic momentum. Under normal circumstances (ie. no excitation from external fields) nuclei spin in random directions (axes are randomly aligned). The relationship between nuclei properties and external magnetic fields present the basis to MRI principles [25–27].

If we take the resultant magnetic momentum sum vector of a certain volume we will have a total net magnetisation M of zero, since all the protons are spinning in different directions (see figure 2.1 (A)). The influence of a magnetic field on a tissue is described by the alignment and precessing movement of the nucleus within two possible orientations (parallel or anti-parallel, see figure 2.1 (B)). In this case M will assume the orientation of the applied magnetic field [26, 27].

The resultant precessing frequency value, known as Larmor frequency w, after the application of an external magnetic field is given by equation 2.1 [26].

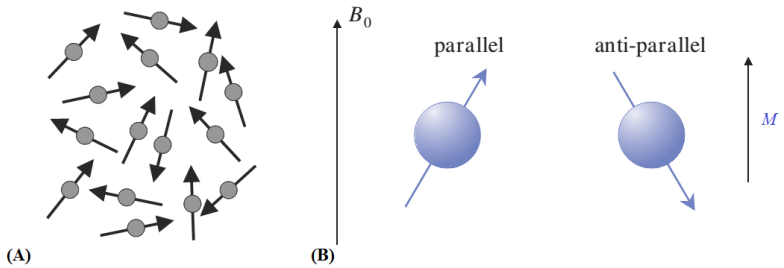

Figure 2.1.: (A) Nuclei without the application of a magnetic field. (B) Nuclei after the application of a magnetic field B. Spin orientation is parallel or anti-parallel to B. The magnetisation vector M is parallel to B. Adapted from [25, 26].

$$w = \gamma B_0 \tag{2.1}$$

Where B_0 is the magnetic field intensity in Tesla (T) and γ is the gyromagnetic ratio given in MHz/T. Each nucleus has its own Larmor frequency so when considering hydrogen, this constant takes the value of -42.57 MHz/T [26].

Changes measured in MRI correspond to field perturbations. When the magnetic field is applied parallel to the z axis, the longitudinal magnetisation, M_z, will have a value different from zero. However, the transverse magnetisation, M_{xy}, will be zero. In order to induce a perturbation in the field, excitation pulses (commonly known as RF-pulses) are applied, causing the magnetic moments to flip. The frequency of these pulses is equal to Larmor's, and is applied perpendicularly to the longitudinal axis. Magnetic moment flip, known as flip angle (see figure 2.2), can be controlled through RF-pulse duration and intensity. Most common flip angles are $\pi/2$ and π, responsible for magnetisation flip by 90° and 180°, respectively [26, 27].

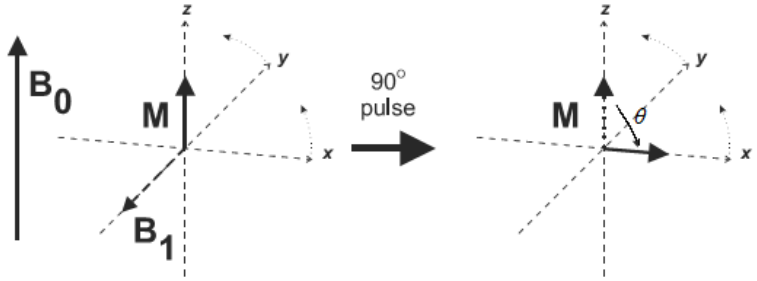

Figure 2.2.: Representation of a 90° RF-pulse effect. The magnetisation vector M is originally aligned with B_0. After the application of the RF-pulse, $B_1(t)$, along y axis, M rotates in xy plane according the flip angle θ. Adapted from [25].

After the RF-pulse is turned off, M returns to its equilibrium state and magnetisation loss can be measured (see figure 2.3).

T1, or *spin-lattice* relaxation, corresponds to M_z recovery. This results from the energy released from excited protons (*spin*) to their surroundings (*lattice*) [25–27]. T1 period is characterised by recovery of 63% of the initial magnetisation M_0. It is the time constant for the growth process verified during the magnetisation recovery (see figure 2.3), τ time after the RF-pulse application, described by equation 2.2 [25].

$$M(\tau) = M_0 \left(1 - exp^{-\tau/T1}\right) \tag{2.2}$$

T2 or *spin-spin* relaxation, represents the required time to M_{xy} decay 63% (reach 37% of M_0). Due to field inhomogeneities there is additional signal suppression, and T2 effect does not account for them. Because of this, it is necessary the introduction of an additional relaxation time, T2*, capable of taking into account field inhomogeneities (T2') and the T2 relaxation, as described in equation 2.3 [26, 27].

$$\frac{1}{T2^*} = \frac{1}{T2'} + \frac{1}{T2} \tag{2.3}$$

With this in mind after RF-pulse application, the loss of M_{xy} is described by an exponential process with the T2* constant, τ time after the pulse, as represented in equation 2.4 [25].

$$M_{xy}(\tau) = M_{xy_{max}} exp^{-\tau/T2^*} \tag{2.4}$$

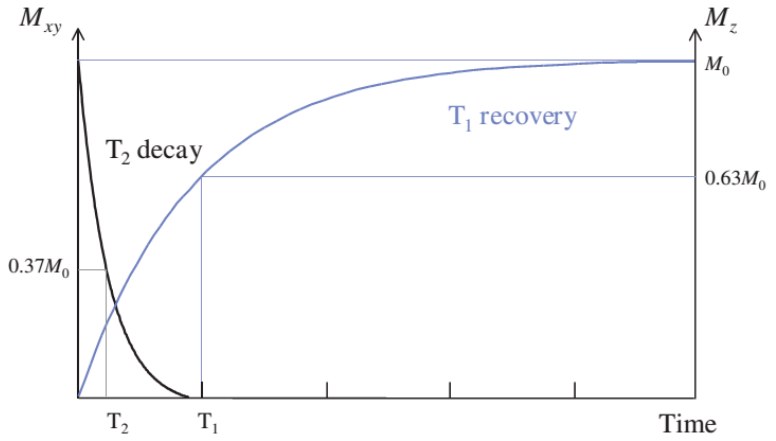

Figure 2.3.: Loss of transverse (M_{xy}) and recovery of longitudinal (M_z) magnetisation, giving T2 and T1 relaxation times respectively with the application of a 90° RF-pulse [26].

With the progressive loss of energy, and reorientation around B_0, an electric current known as free induction decay (FID) is produced. Its initial magnitude depends on M_0 value after the RF-pulse application. FID takes a sinusoidal form and it decays with T2*. When a 90° RF-pulse is applied, followed by successive 180° pulses, FID maximum amplitude decreases with T2 (see figure 2.4) [25, 28].

2.1.2. Sequences

Different contrasts in MRI are obtained through the application of magnetic resonance (MR) sequences. These enable the encoding of information, provenient from radiofrequency (RF) pulses and gradient profiles (resultant signal from MRI),that can be translated in an image through the application of adequate reconstruction algorithms.

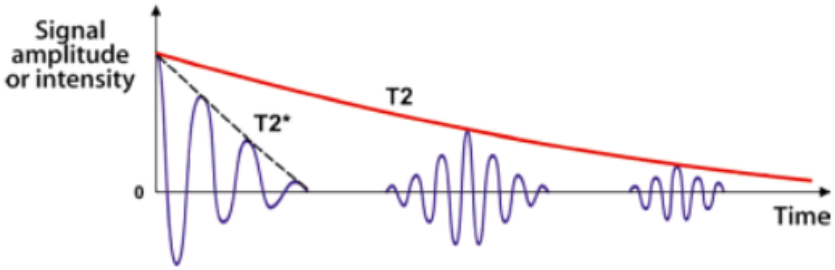

Figure 2.4.: After the RF-pulse suppression, M keeps precessing around B_0, being detectable by a RF coil, therefore presenting the FID effect. Its attenuation is due to the loss of M_{xy}, so T2* decay curve fits FID. With the repetition of echoes, the maximum amplitude of FID signal decreases with T2 [28].

In this section an overview of the fundamental MR sequences will be given, including spin echo (SE), gradient echo (GE) and magnetization prepared rapid acquisition gradient echo (MPRAGE).

SE is characterized by its long acquisition times. A simultaneous 90° RF pulse and a slice selection gradient is applied, followed by a 180° refocusing RF pulse after a time t (see figure 2.5). The rate at which the phase is accumulated does not vary, since protons present a difference of 0° in phase, t time after the refocusing pulse application. Two parameters that define the obtained contrast can be defined: echo time (TE) and repetition time (TR). TE corresponds to the time between the excitatory pulse and the echo reading, and TR to the time between consecutive excitatory pulses [29, 30].

Unlike SE, GE presents shorter acquisition times. A simultaneous RF pulse with a flip angle lower than 90° and a slice selection gradient is applied. Once the RF pulse is turned off, the protons dephase and phase encoding occurs in the y direction. Magnetization is tipped in the transverse plane and while this happens a negative frequency encoding is applied in the x direction in order to induce faster dephasing. Afterwards, a positive frequency encoding is applied in order to rephase protons while the echo is measured (see figure 2.5). Proton dephase and rephase is achieved through the application of negative and positive gradients [29, 30].

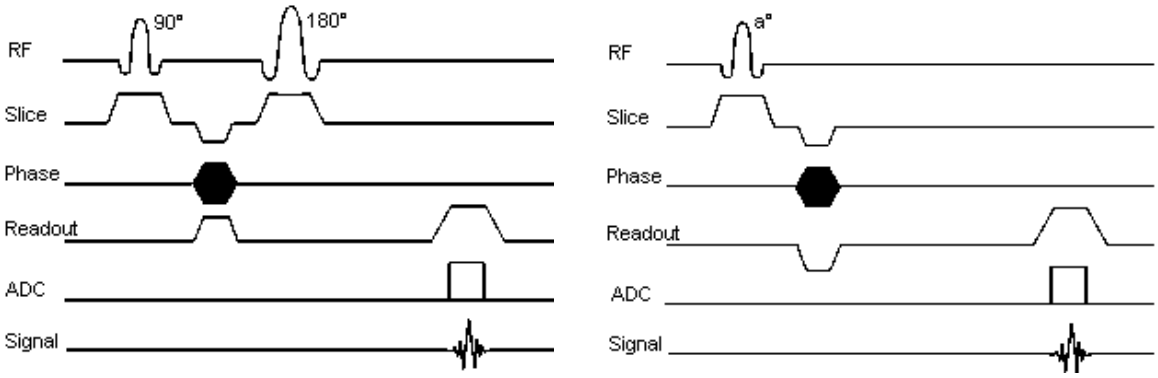

Figure 2.5.: Diagram of the SE (right) and the GE (left) sequences. Adapted from [31].

Three-dimensional MPRAGE is a MRI sequence that was first proposed by Mugler and Brook [32]. It consists in a gradient recalled echo (GRE) imaging sequence preceded by a 180° inversion pulse. The three dimensionality is obtained through the application of a secondary phase

encoding in the slice selection direction. This sequence enables acquisitions with great tissue contrast, high space resolution and full brain coverage with short scan time [32, 33]. A diagram of this sequence is shown in figure 2.6.

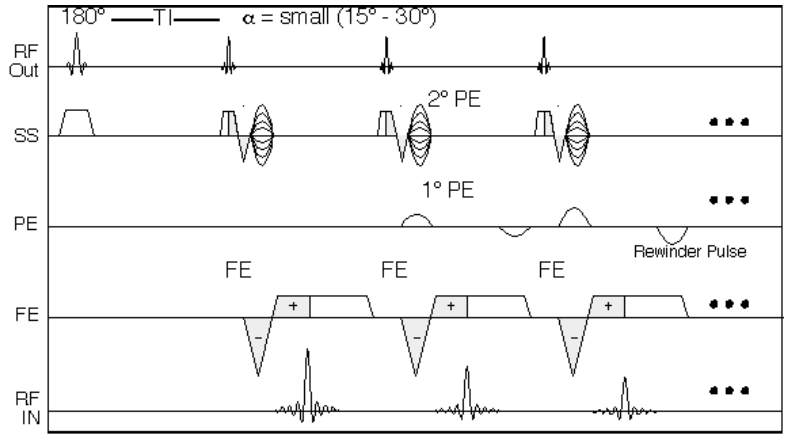

Figure 2.6.: Diagram of the MPRAGE sequence [34].

To sensitize a sequence to diffusion, an additional gradient pulse with the same amplitude but opposite direction is applied. After some time, with the loss of magnetization, the refocusing for protons that moved between the pulse application will not be perfect and the signal is reduced. This method was derived by Stejskal and Tanner who derived equation 2.5 that explains the signal (S) after the application of the pulse gradient, if S_0 is the baseline signal, and relates it to the amount of diffusion occurring. The intensity of the pulse is explained by the constant b-value, b, which depends on the strength, duration and spacing of the gradients [35].

$$S = S_0 exp^{-bD} \tag{2.5}$$

$$with b = \gamma^2 G^2 \delta^2 \left(\Delta - \frac{\delta}{3}\right)$$

where S_0 and S are the initial and after the pulse application signal, respectively, γ is the gyromagnetic ration, G the strength of the gradient pulse, δ the pulse duration, $\Delta$the time between two pulses, and D the diffusion coefficient.

2.1.3. Diffusion weighted imaging

Diffusion weighted imaging (DWI) is a non-invasive MRI technique that makes use of diffusion concepts. It allows collection of information concerning cerebral structures, through water molecules movement quantification.

Diffusion is a physical process, first described by Robert Brown, as a random displacement of particles in a fluid [36]. The laws behind this process were described later by Adolf Fick, who established that matter diffusion is proportional to the concentration gradient (particles move from the hypertonic to the hypotonic medium) The ability to quantify this movement was only possible after quantification of the diffusion coefficient, a result from Einstein studies [36]. However, Fick's law fails at a molecular level. Since the diffusion coefficient is a medium property

that depends on temperature, particle sizes and viscosity, in the thermodynamic equilibrium (temperature or concentration equal to zero) we will have no flux [36]. Nowadays, we know that the particle movement persists [37].

In order to apply the diffusion contrast, the most commonly used method is the pulsed gradient spin echo sequence. This contrast behaves like an inverse T2-weighted (T2-w) image, where the watery tissues with many mobile molecules present lower signal, and the solid tissues stronger signal intensity (see figure 2.7) [26].

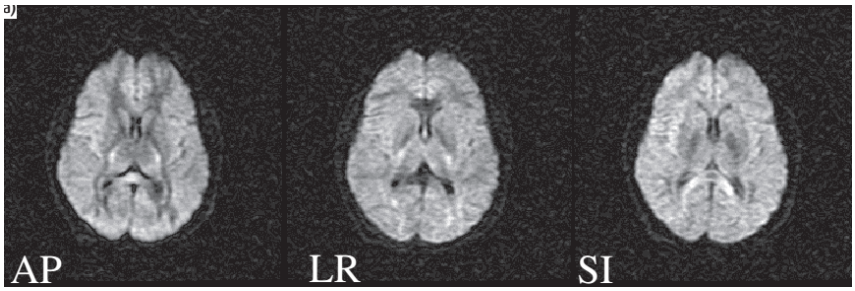

Figure 2.7.: Example of a DWI image set. Each image encodes a different diffusion direction: AP denotes anterior-posterior; LR, left-right and SI, superior-inferior [26].

Despite what we measure with this sequence being related with the actual diffusion coefficient, it may have some contribution from other sources, like micro circulation and transport. Because of this, the apparent diffusion coefficient (ADC) is calculated from information concerning the T2-w and DWI. It is also possible to determine the ADC value from multiple images, applying a least squares fit to the data later [26].

Water molecules movement can be classified in three types: bulk, isotropic and restricted (see figure 2.8). The latter is influenced by numerous factors, namely some restrictions in the medium, such as cell membranes, cytoskeletons and even some macromolecules. In these cases if an obstruction that interrupts the flow exists (e.g. during a stroke), there will be a hypersignal in the DWI scan. On the other hand, a tissue with high diffusion constant, or high ADC, will present a hyposignal in the DWI scan [26].

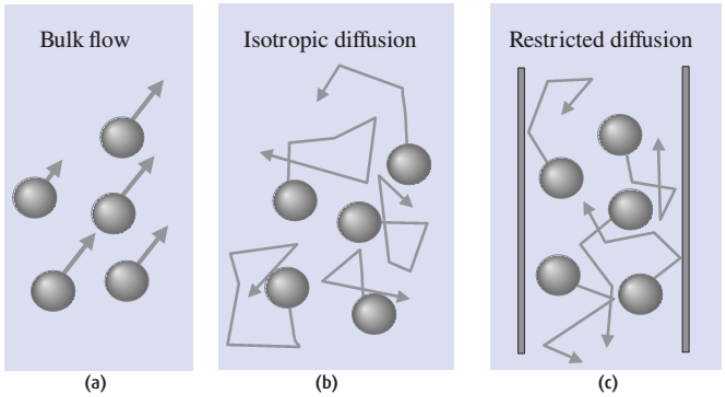

Figure 2.8.: (a) Bulk flow (active transport); (b) isotropic motion, corresponds to the brownian motion; (c) restricted motion includes the cases where there exist physical barriers such as the cell membrane [26].

2.1.4. Diffusion Tensor Imaging

DWI enables water molecules characterisation in one direction. However, we know water molecules movement in our brain is anisotropic, and the ability to characterise the amount of anisotropy in a medium enables diffusion quantification [26]. This characteristic is referred to a restricted type of diffusion present in regions delimited by membranes, creating a preferred path, for example along nerve fibres. With this, we can access the different white matter fibres orientation, thus identifying paths between various cortex regions.

DTI presents itself as a non-invasive technique capable of anisotropic medium characterisation through water molecules displacement evaluation. However, this task is not trivial and requires a tensor definition. According to our needs the tensor can be represented as [26, 38]:

$$DT = \begin{bmatrix} D_{xx} & D_{xy} & D_{xz} \\ D_{yx} & D_{yy} & D_{yz} \\ D_{zx} & D_{zy} & D_{zz} \end{bmatrix}$$

Where the first and second subscript letter represent the body and gradient orientation, respectively. In order to compute the ADC value in an anisotropic tissue we need an unweighted diffusion image (to take in account the T2-w image) besides the tensor [26].

Diffusivity can be described by the three eigenvalues of the diffusion tensor, which represent the axes of an ellipsoid. The reason to use ellipsoid bounds is related to anisotropic medium characteristics (see figure 2.9). In this case, we can assess the average displacement of the molecules in case they would diffuse in that area. It is important to notice that each ellipsoid is related to a single voxel, where each one of the main axes correspond to the primary diffusion direction. Ellipsoid eccentricity is related with anisotropy level, and dimension asymmetry to diffusivity. Diffusion direction is determined by the biggest eigenvalue [26, 38].

As stated earlier it is possible to compute diffusion related variables, including mean diffusivity (MD), fractional anisotropy (FA) and relative anisotropy (RA) indices, which are important measures to serve as markers in clinic diagnose [38, 40]. The expression to obtain MD is given by equation 2.6, FA by 2.7 and finally RA by 2.8 [38].

$$MD = \frac{D_{xx} + D_{yy} + D_{zz}}{3} = \frac{Trace(DT)}{3} \tag{2.6}$$

$$FA = \sqrt{\frac{3\left[(\lambda_1 - \langle\lambda\rangle)^2 + (\lambda_2 - \langle\lambda\rangle)^2 + (\lambda_3 - \langle\lambda\rangle)^2\right]}{2\left[(\lambda_1)^2 + (\lambda_2)^2 + (\lambda_3)^2\right]}} \tag{2.7}$$

$$RA = \sqrt{\frac{\left[(\lambda_1 - \langle\lambda\rangle)^2 + (\lambda_2 - \langle\lambda\rangle)^2 + (\lambda_3 - \langle\lambda\rangle)^2\right]}{3\langle\lambda\rangle}} \tag{2.8}$$

$$with \langle\lambda\rangle = \frac{\lambda_1 + \lambda_2 + \lambda_3}{3}$$

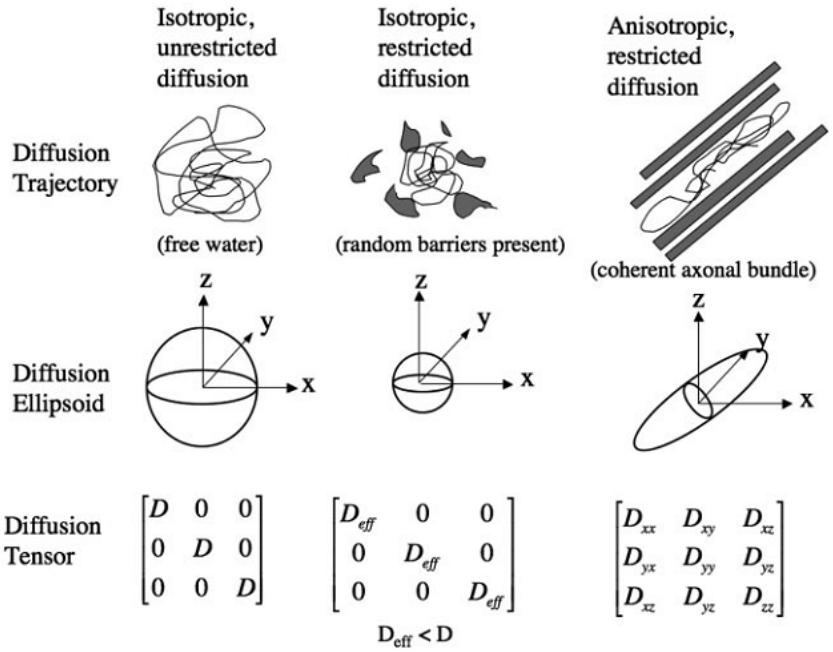

Figure 2.9.: In the first line we have the type of diffusion, in the second, the ellipsoid representation and finally in the third line the diffusion tensor. In the anisotropic condition we see that the diffusion ellipsoid has the flow direction, while in the other two situations is represented by a sphere [39].

However, models used to apply the quantification algorithms rely on a gaussian model that struggles in the crossing fibres regions and also in the presence of restrictions, such as cell membranes, leading to errors when obtaining the diffusion anisotropy index and its direction. This happens when we have a group instead of a single fibre in one voxel [3]. Researchers acknowledge this limitation and work towards the development of new techniques and algorithms to surpass it. One example is diffusion kurtosis imaging (DKI) [5, 41, 42].

2.1.4.1. Tractography

The ability of reconstructing white matter fibres from the diffusion pattern, using resultant data from the application of the techniques presented in previous sections, enables not only to access information about brain pathways, but also the capability to build three dimensional maps [39].

This tool allowed the study of white matter micro-structure in various diseases, including brain tumours, schizophrenia and Alzheimer [39].

In order to construct these images, DTI metrics are used, especially FA. In tractography three kinds of fibres are identified, named accordingly to their location and connections: associative, projection and commissural fibres. Associative fibres connect regions from the same hemisphere (anterior to posterior); projection fibres are responsible by signal transmission between cortex and subcortical region (superior to inferior) and commissural fibres connect both hemispheres (left to right) (see figure 2.10) [39].

In order to construct the tractography maps, various algorithms can be used, from three distinct natures: deterministic, probabilistic and global.

One deterministic model is the fibre assignment by continuous tracking, initiating fibres trajectories from the user defined voxels. This algorithm works by following the value of the first eigenvalue from voxel to voxel. Its constraints allow the maintenance of the streamline propagation, enssuring that only regions with fibres where the diffusion tensor represents realistically, are considered paths [39].

Probabilistic methods incorporate uncertainty measures, related to noise, movement and distortion from artefacts, allowing production of connectivity metrics for each voxel. These techniques do not delineate a greater portion of a white tract but disperse it. However it faces some problems, including limited knowledge about the diffusion tensor and usage of a probability density function that is limited to the methods used to build it [39].

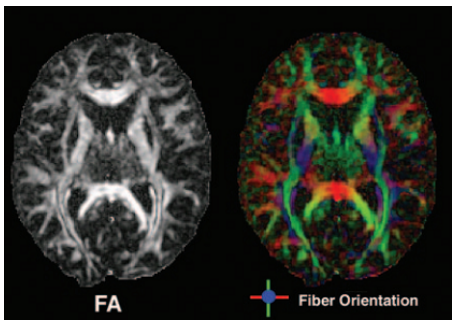

Figure 2.10.: Tractography image obtained from DTI FA information. This represents a colour scale dependent on fibre orientation (given by the first eigenvalue of the diffusion tensor) and FA value. Green fibres correspond to a left to right orientation; red, anterior to posterior and blue from superior to inferior. Adapted from [39].

2.2. Positron Emission Tomography

PET is an imaging technique that uses radioisotopes administered to patients (by injection or inhalation), in order to measure physiological and biochemical processes *in vivo* [43]. Specific biomolecules can be labelled with radioisotopes, allowing scanners to detect and image the molecules spatial distribution by detecting the isotope decay. There is a wide variety of positron-emitting radioisotopes and one of the most common for brain imaging is ^{18}F, used to label flurodeoxyglucose. Fluorine 18 Flurodeoxyglucose ([^{18}F]-FDG) is used to label glucose molecules, which provides information where there is a lesion due to the usual larger glucose uptake in these cases, helping its classification [43, 44].

2.2.1. Basic principles

Nuclear imaging techniques are dependent on the use of radioisotopes. In the particular case of PET, positron emitting nuclides are used due to its dependence in beta decay (represented by expression 2.9) [43, 45].

$$ {}^{A}_{Z}X \longrightarrow {}_{Z-1}{}^{A}X_{n-1} + \beta^{+} + \nu \tag{2.9} $$

In this reaction a positron, β, and a neutrino, ν, are released, from the positron emitting nuclide, ${}^{A}_{Z}X$ (mass number A and atomic number Z), characteristic of the beta decay.

PET uses the tracer principle, which states that a radioactive material is integrated in metabolic reactions. This way, if a patient is administered with a positron emitting radioisotope, such as [^{18}F]-FDG, it will be possible to measure the uptake of radiotracer during the observation time. Since positrons interact with matter, they will react with nearby electrons forming a pair, resulting in positron annihilation and the conversion of their mass in two photos of equal energy (511 keV) that scatter in opposite directions (180°) (see figure 2.11) [43, 45].

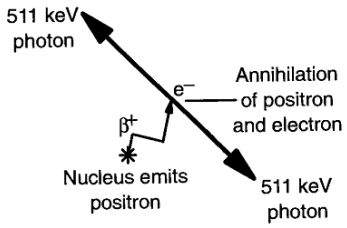

Figure 2.11.: Positron electron pair annihilation and subsequent production of two 511 keV electrons. Adapted from [43].

However, since these photons are created inside the subject body, they are susceptible to different types of matter interaction. These can be pair production, photoelectric and compton effect (see figure 2.12). Even though they are not directly related to the image production, they end up affecting it, producing changes in the final image that require correction. Pair production occurs when high energy photons (double the mass of the electron) interact with the electrons or the nuclei field, representing the least common interaction. Photoelectric effect consists on the emission of an electron, after a photon transferred energy to it. It is more common for photons with lower energies (around 100 keV) and elements with higher atomic number. Compton effect describes an inelastic collision between a photon and a free electron, and the photon is scattered with lower energy in a different direction [43, 45, 46].

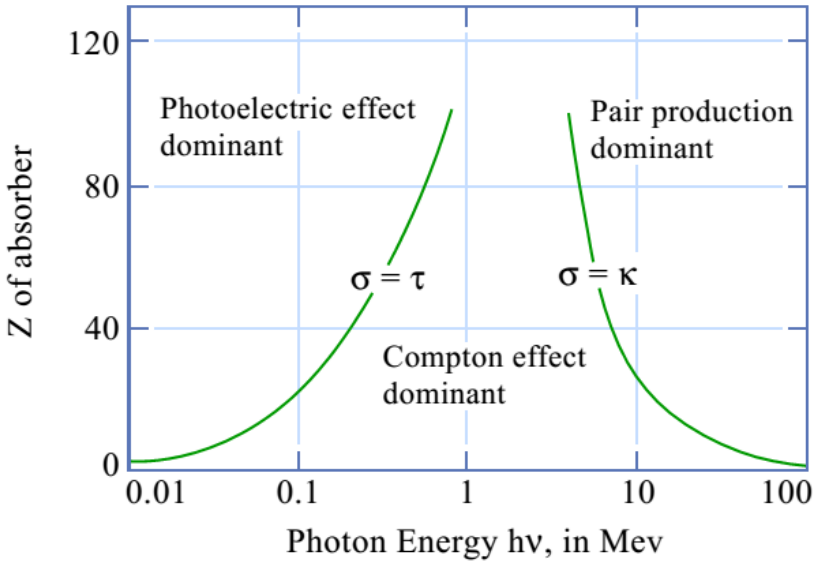

Figure 2.12.: In this graphic we can see the influence of a material atomic number and photon energy. Photoelectric and compton effect are the most common in the energy range of the produced photons during the pair annihilation in PET imaging [46].

Besides interaction with matter, distance travelled by the positron also affects spatial resolution of the final image, since the interaction occurred farther from the point where the tracer actually is [45].

PET scanners use a ring of detectors that record the occurrence of coincident events. These correspond to simultaneous detection of the photons created in the annihilation process (these must be within a defined energy and time range, limited by the scanner resolution). Each of these events is assigned to a line of response (LOR), and used later when applying the reconstruction algorithms. However, not all events detected by the system are true events and may be designated by scatter, random and multiple (see figure 2.13 for the first three types). The scatter events occur when at least one photon interacts with matter in one of the previous described forms. Random events represent the possibility of detecting two photons in the same LOR from different annihilation's, and the corresponding ones are not detected. Finally multiple events refer to the case when more than two photons are detected in different detectors within the scanner time range resolution. These events deteriorate image quality, thus the need of correction mentioned earlier [43].

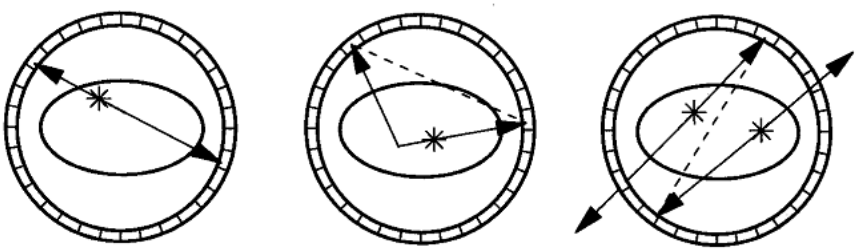

Figure 2.13.: True (left), scatter (centre) and random (right) events. [43].

As mentioned before, there is need to correct the final image due to the photons interaction with matter. However, some corrections related with scanner characteristics are also necessary. Concerning the photon interaction, corrections involving scatter, attenuation, random and multiple events should be undertaken. Relative to the scanner, these are related with detector efficiency, dead time, normalisation and partial volume correction. Besides these factors, patient motion must be taken into account [43, 45].

2.2.2. O(2-Fluorine-18-Fluoroethyl)-L-Tyrosine ([^{18}F-FET)

O(2-Fluorine-18-Fluoroethyl)-L-Tyrosine ([^{18}F]-FET) is a tracer based in tyrosine, and ^{18}F is an radioisotope with a half-life of 110 minutes, which does not limit its use to places equipped with a cyclotron [47]. [^{18}F]-FET is produced via a two-step process described in [48]. In figure 2.14 we have the representation of the initial and fluorinated L-tyrosine isomer.

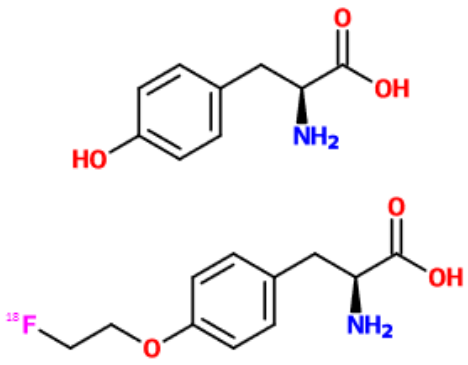

Figure 2.14.: Representation of natural isomer, L-Tyrosine (up), used to produce 18F-FET (bottom).

Being based in tyrosine, [^{18}F]-FET is a labelled amino acid, allowing the study of tumour tissue

through the evaluation of its uptake. It is important to notice that [^{18}F]-FET is not incorporated in proteins, does not participate in any metabolic pathway [49], but it can be transported across the epithelium and epithelial blood barrier, thus the possibility of its use for tumour detection [49, 50]. Due to the stereospecificity and mediation by amino acids transporters, characteristic of tumour cells, added to its long half life, it has been incorporated in clinical use for glioma imaging [23, 47, 50].

Usage of this tracer has showed capability to distinguish tumour recurrence from radiation-induced changes in cases of high- and low- grade glioma presence [51]. Since it is an amino acid based tracer it is also referred as being better than [^{18}F]-FDG to detect primary tumours, which leads to improvement of target biopsies and information concerning the tumour extension that can be incorporated in surgery and radiotherapy planning [23]. Although [^{18}F]-FDG is a good marker for the evaluation of tumour grade and prognosis of brain gliomas, the high cerebral metabolism makes it difficult to define the tumour borders [50]. The advantage of using [^{18}F]-FET relies on the fact of not depending on metabolism, but just trades between the neoplastic cells and its surroundings, allowing the definition of the tumour by identifying its borders (presence of a ring around necrotic tissue in brain gliomas) [50, 51].

3. Connectomics

Connectomics is the field of study interested in functional and anatomical brain connections. Development of this field resulted from the interest in unravelling the underlying circuitry and mechanisms, responsible for the capability of performing complex tasks. Some authors are optimistic regarding the incorporation of this analysis to clinical routine as a marker to some brain pathologies [10, 52, 53].

Over the last decades we seen an increasing interest in how the human brain works, leading to investment in neuroscience research. With ever more powerful technology to study the human brain, scientists are able to access information about structure, morphology and even function, especially thanks to the development of non-invasive neuroimaging tools. Nowadays, one of the biggest point of interest of this community stands on brain connectivity [6, 7, 10, 54–56]. This concept relies on the assumption of the white matter tracts as links and the various points in the cortex as nodes (where the links meet). Therefore, we can identify a complex network that allows different brain regions to communicate [55, 57]. One on-going work in this field is the Human Connectome Project, which aims to map the human brain connections [58].

The identification of a network is based firstly on its type, which can be divided in structural, functional and effective [52, 59]. Structural connectivity is related to direct connections between different brain regions via white matter tracts. Functional connectivity refers to temporal correlation between two distinct regions activity [60, 61]. Effective connectivity requires causality, not implying a direct physical connection but the influence a brain regions causes over another either direct or indirectly [61].

3.1. Networks: definition and properties

Network is a mathematical representation of a complex system formed by nodes (vertices) and links (edges). When assuming the brain as the system we desire to describe, nodes correspond to brain regions and links to the structural, functional or effective connectors (see figure 3.1).

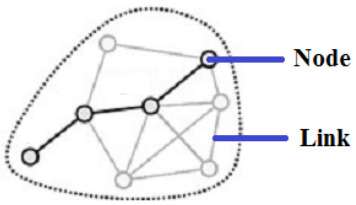

Figure 3.1.: Node and link representation in a network. Adapted from [62].

The nature of nodes and links is determined by the combination of various brain mapping methods, anatomical parcellation schemes and different types of connectivity measures. Parcellation schemes should include the whole cortex area enssuring that individual nodes do not overlap.

When comparing connectivity data between subjects it is important to use the same parcellation scheme in order to achieve a coherent comparison. Links, presented as the connectors, are differentiated according to their weight and directionality. In matters of weight, it gives information concerning structural (size, density and length of white matter tracts) and functional or effective (magnitude of correlational or causal interactions) strengths. Directionality verifies the direction of the information flow, accessing not only the existence of a connection but in which sense it is established. On the other hand, using binarised links enables the verification of existence or non-existence of connectivity (see figure 3.2) [62].

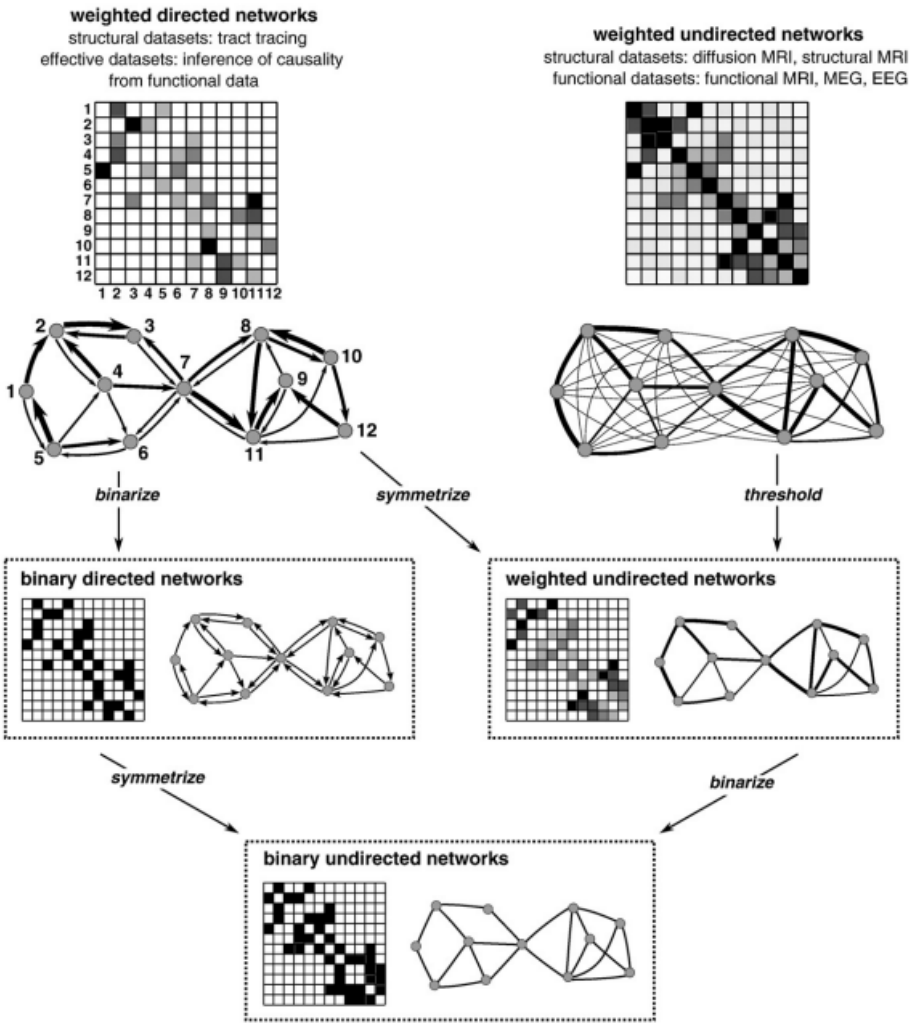

Figure 3.2.: In this figure we can see the connectivity matrices and correspondent graphs. It is important to refer that the directed network presents the connections direction (in which the information flows) and non-binarised networks have different links intensity (representing the connection strength: darker links correspond to stronger connections) [62].

3.2. Brain networks

Connectivity matrices give a large amount of information considering a single network. In this way, more information about, not only brain structure, but also its relation with functionality ca be gathered. Studies show the human brain cortex as a group of clusters linked to each other. With this, various theories to explain this phenomenon emerged, but it is the small-world model

that attracts more agreement among researchers [52, 53, 62, 63]. This model assumes that, in a network, the path taken by the information is always as short as possible, which is the common behaviour found in human brain connections, with high clustering coefficients and occasional long connections (see figure 3.3) [53, 62].

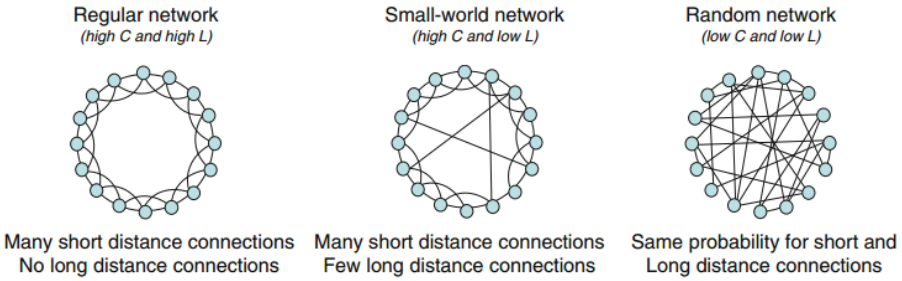

Figure 3.3.: Comparison between regular, small-world and random networks. **C** stands for clustering and **L** for the path length. Small-world and regular networks present a high clustering level, but the latter has a higher path length. On the other hand, random networks show low cluster level and small paths. Adapted from [53].

3.3. Network measures

In order to better understand the used terminology in connectomics, and the used terms throughout this thesis, a brief explanation can be found below [60, 62]. In figure 3.4 a scheme with some of these metrics can be found.

- **Nodes:** brain region.
- **Links:** axonal tracts (structural connections); functional connections (related with correlated activation).
- **Degree:** number of connections a node has.
- **Strength:** sum of all neighbouring links weights.
- **Clustering coefficient:** fraction of triangles around an individual node.
- **Modularity:** statistic that establishes the number of groups that can be delineated without overlapping.
- **Characteristic path length:** average smallest path between all nodes in a network.
- **Global efficiency:** inverse of the average shortest path.
- **Motifs:** patterns of local connectivity.
- **Hub:** node that interacts with various regions facilitating the transmission of information.
- **Closeness centrality:** inverse of the average shortest path length from one node to the rest.

- **Betweenness centrality:** fraction of all the shortest paths that pass through a given node.

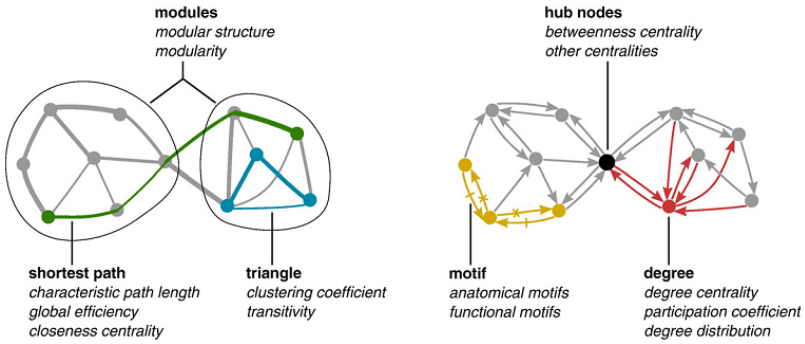

Figure 3.4.: Network measures have usually basic connectivity properties (gray). Integration measures include the shortest path (green), while segmentation is usually based on clustering coefficients (blue) but also on sophisticated module division (ovals). Measures of centrality can be based in node degree (red) or length and number of shortest paths. Hubs (black) usually take part in various short paths and often have high betweenness centrality. Patterns of local connectivity are quantified by network motifs (yellow) [62].

3.4. Connectivity in brain tumours

Traumatic events or lesions of the central nervous system can lead to the reorganisation/ rearrangement or even disruption of anatomical and functional connections, thus leading to changes in the behaviour of brain regions and networks [6].

Investigating brain connectivity in the surrounding of intracranial tumours is not only of scientific interest but can also provide clinically important information in order to enable function-preserving tumour resection (as mentioned in section 1.2.1).

Performed connectivity studies aimed to understand how physical and cognitive function is affected in the presence of brain lesions. This kind of information might be useful for the characterisation of each clinical case, allowing presurgical planning, and the prediction of sequelae from certain interventions, such as gross total tumour resection [19]. Most published studies have used MEG, fMRI, transcranial magnetic stimulation and EEG to assess functional changes, and DTI for structural changes [6–9, 64], to study the effect in networks directly affected by the lesion.

Bartolomei et al., 2006, hypothesised the influence of brain tumours in the disruption of functional connectivity brain networks. In order to test this hypothesis MEG was used, and reported findings included higher loss of functional connectivity in patients with brain tumours, not exclusively confined to peritumoural regions. In some cases, alterations were verified in the contralateral hemisphere, which the authors suggest to additionally explain the cognitive dysfunction that patients experienced. Both structural and functional changes in remote areas were associated with the diaschisis (functional disconnection between a portion of the brain and a distant, damaged, brain region) phenomenon in subcortical regions and cerebellum, with structural changes evaluated using tractography derived from DTI [6].

Guggisberg et al., 2008, aimed to map the functionality of brain areas according to functional connectivity measures, in patients with brain lesions (including tumours), following the assump-

tion that healthy areas were functionally disconnected from the damaged regions. Reported results showed decreased connectivity in patients with lesion-induced neurological deficits in some regions when compared with the intact matched contralateral region [9].

Martino et al., 2011, studied functional connectivity (resting state) in patients with tumours located in eloquent areas using MEG. According the authors, the verified loss in functional connectivity between eloquent areas and the rest of the brain is hypothesised to be due to tumour infiltration. Results of this study suggested that decreased cortical connectivity around a tumour should result in a lower capability of using intraoperative electrical stimulation (neurosurgical technique to identify functional regions), when MEG seems able to distinguish between healthy and damaged tissue. On the other hand, with activation similar or greater to the homologous contralateral region, MEG has an inferior performance, being unable to distinguish correctly eloquent areas that needed to be preserved during surgical tumour resection [8].

Briganti et al., 2012, investigated the influence of brain gliomas in the language network using fMRI. Results of this study included decreased activation of the language networks in patients with tumours, and reduced within selected regions of the affected hemisphere, with additional changes between the temporoparietal junction of the two hemispheres. The authors suggested the presence of the tumour as the cause of the reduced degree of activation between language-related brain regions. However, it was also observed that although the pattern of activation was activated by tumour position it was not restricted to the areas immediately surrounding it, since this behaviour was identified between remote and contralateral areas, leading to the supposition that tumours may distort normal whole-brain activity [7].

Neuschmelting et al., 2015, evaluated the possibility of reverting deficits caused by tumour infiltration of the motor network, by indirect mass effects and/ or perifocal oedema with a multimodal (MR-PET) approach. Patients with tumours in the neighbourhood of the motor region may present motor impairment, and some may deteriorate after surgery. The authors also used DTI in order to characterise the structural connectivity within the tumour and surrounding tissue, including quantification of the integrity of fibre tracts. Additionally, the ongoing debate on how to use the diffusion metrics in the differentiation of glial-versus-metastatic growth patterns in white matter is pointed out, and the fact that increased and reduced FA on regions related to glial tumours are present in the literature [65–67]. Presented conclusions embrace the usage of a multimodal approach in order to predict motor impairment and predict surgery-associated functional outcome, which is believed to contribute for risk-evaluation in presurgical planning in patients with brain tumours [64].

Notwithstanding the above, the effect of malignant brain tumours on whole-brain connectivity is a topic that has not yet been consistently explored.

4. Methodologies

4.1. Material

Nine patients with glioblastoma multiforme, adjacent to the primary motor area, underwent simultaneous MRI and dynamic [^{18}F]-FET PET. The control group comprised twenty-two healthy subjects (only MRI was performed). Information with the groups characterisation can be found in Table 4.1.

Table 4.1.: Control and patients group characterisation according gender. Patients are divided into two groups considering the side where the tumour is localised. Age is given in years old (y.o.) with mean±standard deviation (SD) and with the respective range.

	Control group	**Patients - Left hemisphere lesions**	**Patients - Right hemisphere lesions**
N	22	5	4
Gender	11M / 11F	3M / 2F	2M / 2F
Age (y.o.) by gender	59±7 / 59±6 [50 - 68] / [50 - 70]	51±6 / 55±18 [46 - 58] / [42 - 68]	37±10 / 48±22 [30 - 44] / [32 - 63]
Age (y.o.) group total	59±6 [50 - 70]	53±10 [42 - 68]	42±15 [30 - 63]

Neuroimaging data were acquired on a hybrid MR-PET scanner, consisting of a 3T Siemens scanner with a BrainPET insert [68]. A birdcage transmit coil and an 8-element receive array were used for radiofrequency transmit and signal receive respectively. The MRI protocol included volumetric T1-w MPRAGE (1x1x1 mm^3), DTI (patients: dir=30, b-value=800 s/mm^2, 2 averages, 2x2x2 mm^3; controls: dir=30, b-value=1000 s/mm^2, 1 averages, 2x2x2 mm^3) and contrast enhanced volumetric T1-w MPRAGE (1x1x1 mm^3) sequences. The amino acid [^{18}F]-FET was produced via nucleophilic ^{18}F-fluorination with a specific radioactivity of more than 200 GBq/μmol [69]. Time activity curves of [^{18}F]-FET uptake were generated and mean and maximum tumour-to-brain ratios were determined by region-of-interest (ROI) analysis. Tumour volumes in [^{18}F]-FET-PET images were calculated from images containing the integrated intensity (20-60 min) using threshold-based volume-of-interest analyses that included voxels with a tumour-to-brain ratio of at least 1.6. This cutoff was based on a biopsy-controlled study in cerebral gliomas in that a lesion-to-brain ratio of 1.6 best separated tumour from peritumour tissue [50].

The MIBCA toolbox (`http://www.mibca.com`, [11]) was used to automatically pre-process MR-PET data (including brain parcellation) and to derive imaging and connectivity metrics from the multimodal data, that is, cortical thickness (CtxT) from contrast enhanced T1-w data; FA, MD, clustering coefficient (ClusC), node degree (Deg) and pairwise ROI fibre tracking from DTI data; and standardised uptake value (SUV) from PET data. For each extracted imaging/connectivity metric, mean and SD values were automatically calculated for the control group.

To do so, MIBCA uses various tools including: the NIfTI tools[1], FreeSurfer[2] [70], Statistical Parametric Mapping (SPM)[3], FSL[4] and TrackVis[5]. First step for all modalities is the data conversion to NIfTI, if needed. The pre-processing was divided into four main steps: (1) contrast-enhanced T1-w, (2) DTI and (3) PET data pre-processing, and (4) results integrity check.

For the contrast-enhanced T1-w data pre-processing the full FreeSurfer pipeline was implemented, which included the registration of each volume to the MNI305 atlas (uses talairach coordinates) followed by skull striping. Classification of white matter and corresponding surface identification (labelled white surface) came next. Identification of the surface between grey matter and cerebrospinal fluid (labelled pial surface) was done considering differences between them. Finally, we proceeded to the parcellation step where cortical and subcortical labelling took place. From this step a parcellation map was created (according the maps in appendix B, figures B.1 and B.2). This process is fundamental for the remaining modalities analysis. The parcellation information ensures that we looked to the same place when analysing other imaging data [71, 72]. Structural metrics were then computed (e.g. CtxT using the distance between the two white and pial surfaces) by structure.

For DTI data pre-processing a FSL and TrackVis were used. FSL algorithms were used to correct eddy currents. TrackVis functions were used to estimate FA and MD, and tractography. These images were then co-registered to our structural image, using SPM, in order to get the corresponding transformation matrix. The inverse of the obtained matrix was then applied to the parcellation map. With the map co-registered to the diffusion images dataset different diffusion metrics were extracted, giving us values for each metric by structure.

Finally, for PET data pre-processing, used data had the SUVs already computed. SPM was used to co-register it to our structural image, similarly to the DTI process described above. The inverse of the obtained transformation matrix was then applied to the parcellation map. This resulted in a map co-registered with the PET image, allowing the extraction of SUV values by region.

After doing this for each subject/ patient, data was manually checked to look for inconsistencies, incorrect co-registrations or segmentations. When segmentation/ parcellation problems occurred (problem during T1-w pre-processing step), reference points were given to FreeSurfer to improve the algorithm application. Co-registration to other modalities was also checked, and corrected as needed by re-running MIBCA to run SPM again and giving it reference points.

In patients, due to the tumour presence, an inspection of how well the parcellation map was adjusted in regards to the altered brain topology was performed. This was possible by overlapping the obtained map on top of the structural and the PET image. Since we expected higher SUV in the tumour region, and that the tumour mass should be classified as something else (not white or grey matter), these regions should not have any labels on them.

Results were written in Matlab structures and saved in .mat files. The toolbox created a structure for each subject that included all different evaluated metrics and corresponding values by structure. In every run, two additional structures were created containing: (1) information for

[1] NIfTI tools, `https://www.mathworks.com/matlabcentral/fileexchange/8797-tools-for-nifti-and-analyze-image?requestedDomain=www.mathworks.com`

[2] FreeSurfer, `http://freesurfer.net/`

[3] SPM, `http://www.fil.ion.ucl.ac.uk/spm/`

[4] FSL, `https://fsl.fmrib.ox.ac.uk/fsl/fslwiki`

[5] Ruopeng Wang, Van J. Wedeen, TrackVis.org, Martinos Center for Biomedical Imaging, Massachusetts General Hospital. `http://trackvis.org/`

all pre-processed subjects in that run and, (2) resultant mean and SD values for all metrics by structure. These were later used to apply the statistical analysis described in the following sections and loaded for visualisation purposes using the MIBCA toolbox.

For all patients, regions directly related (identified by increased uptake in [^{18}F]-FET-PET) and surrounding the tumour (to the extent of the present oedema, verified by the diffusion images) were identified and can be found in Table 4.2.

Table 4.2.: Peritumour regions for each patient identified by increased uptake in [^{18}F]-FET-PET and to the extent of the present oedema identified in diffusion images. Each patient structural image and corresponding parcellation map can be viewed in appendix C.

Patient - Lesion	Peritumour regions
A - Left Parietal Lobe	Lh-PoCG, Lh-SPL, Lh-IPL, Lh-PCG, Lh-SMG
B - Left Parietal Lobe	Lh-PoCG, Lh-PCG, Lh-SMG, Lh-parsOP, Lh-STG, Lh-Ins, Lh-SPL, Lh-TTG
C - Left Parietal Lobe	Lh-PCG, Lh-PoCG
D - Left Temporal Lobe	Lh-STG, Lh-SMG, Lh-PoCG, Lh-PCG, Lh-parsOP, Lh-MTG, Lh-Pt, Lh-Ins, Lh-TTG
E - Left Temporal Lobe	Lh-Ins, Lh-parsO, Lh-PCG, Lh-ITG
F - Right Frontal Lobe	Rh-SFG, Rh-PCG, Rh-pCG, Rh-PoCG, Rh-PaCG, Rh-PCn, Rh-iCG, Rh-caCG
G - Right Temporal Lobe	Rh-SMG, Rh-PCG, Rh-parsOP, Rh-PoCG, Rh-ITG, Rh-MTG, Rh-bankssts, Rh-STG, Rh-parsT
H - Right Frontal Lobe	Rh-PCG, Rh-caMFG, Rh-rMFG, Rh-SFG, Rh-parsT, Rh-parsOP
I - Right Temporal Lobe	Rh-SMG, Rh-bankssts, Rh-MTG, Rh-PoCG, Rh-IPL, Rh-STG, Rh-Ins, Rh-TTG

Lh – Left hemisphere; Rh – Right hemisphere; G – Gyrus; L – Lobule; C – Cortex.
ITG – inferior temporal; MTG – medial temporal; STG – superior temporal; TTG – transverse temporal; SMG – supra marginal; SPL – superior parietal; IPL – inferior parietal; SFG – superior frontal; rMFG – rostral middle frontal; caMFG – caudal middle frontal; pCG – posterior cingulate; iCG – isthmus of the cingulate; caCG – caudal anterior cingulate; PCG – precentral; PoCG – postcentral; PaCG – paracentral; parsT – pars triangularis; parsO – pars otbitalis; parsOP – pars opercularis; PCn – precuneus; bankssts – banks of the superior temporal sulcus; Pt – putamen; Ins – Insula.

4.2. Normal range intervals

Control based variation ranges enable the assessment of differences present in patient data. This is done evaluating how different the data from patients is when compared to a healthy population, in this case the control group.

Data analysis was focused in two different approaches: evaluation of intrahemispheric differences and changes in full brain connectivity. For both cases mean and standard deviation, SD, values from the control group were used to build variation ranges, as explained in the following subsections.

4.2.1. Intrahemispheric differences

For the evaluation of alterations considering intrahemispheric differences, three distinct ranges were built using the control group mean and associated error, assessed from SD data. The first range was obtained using all the data from the control group, the second using only data from healthy males and the third using data only from healthy females.

First the asymmetry index (AI) for each metric and the total number of fibres difference was calculated as follows.

For each connectivity metric, the values obtained for each distinct region of a hemisphere were subtracted to their corresponding contralateral value. So, the values for the structures in the right hemisphere were subtracted from those on the left side. Following this, an AI can be evaluated according to:

$$\begin{aligned} AI_l &= \frac{V_l - V_r}{V_l + V_r} \\ AI_r &= \frac{V_r - V_l}{V_r + V_l} \end{aligned} \tag{4.1}$$

where AI_l and AI_r stand for the left and right asymmetry indices, and V_l and V_r are the left and right structures' values, respectively.

Pairwise ROI fibre tracking data for each hemispheric region were subtracted from the values of the contralateral region, according to:

$$\begin{aligned} NF_{ldif} &= NF_l - NF_r \\ NF_{rdif} &= NF_r - NF_l \end{aligned} \tag{4.2}$$

where NF_{ldif} and NF_{rdif} correspond to the difference of left fibres subtracted from the right and of right subtracted from the left-sided ROIs, respectively. NF_l and NF_r correspond the total number of fibres of connections from left and right hemispheres, respectively.

Finally, for each imaging/ connectivity metric, the calculated SD was used to obtain the error, δ, associated with the AIs (equation 4.3), as well as the calculated fibre counts differences between contralateral ROIs (equation 4.4).

$$\begin{aligned} \delta\left(AI_{ldif}\right) &= \left|AI_{ldif}\right| \sqrt{\left(\frac{\delta\left(V_l - V_r\right)}{V_l - V_r}\right)^2 + \left(\frac{\delta\left(V_l + V_r\right)}{V_l + V_r}\right)^2} \\ \delta\left(AI_{rdif}\right) &= \left|AI_{rdif}\right| \sqrt{\left(\frac{\delta\left(V_r - V_l\right)}{V_r - V_l}\right)^2 + \left(\frac{\delta\left(V_r + V_l\right)}{V_r + V_l}\right)^2} \\ & \qquad with, \\ \delta\left(V_{l/r} - V_{r/l}\right) &= \delta\left(V_{l/r} + V_{r/l}\right) = \sqrt{\delta\left(V_{l/r}\right)^2 + \delta\left(V_{r/l}\right)^2} \end{aligned} \tag{4.3}$$

$$\delta\left(NF_{l/rdif}\right) = \sqrt{\delta\left(NF_l/r\right)^2 + \delta\left(NF_r/l\right)^2} \tag{4.4}$$

For the work developed in this thesis, built ranges for each metric could deviate from one to three times the calculated error values, and had the following structure:

$$Normal\ range\ variation = [AI - n \times \delta(AI); AI + n \times \delta(AI)],$$

where n can take the value 1 (1thres), 2 (2thres) or 3 (3thres), depending on the desired sensitivity for latter patient threshold.

4.2.2. Whole-brain assessment

For whole brain connectivity assessment, ranges were constructed using the mean and SD values for all metrics. Similarly, as in the intrahemispheric case, three distinct ranges were built: using data from the whole group, only healthy males and only healthy females volunteers.

For the work developed in this thesis, built ranges for each metric could deviate from one to three times the SD values, and had the following structure:

$$Normal\ range\ variation = [mean - n \times SD; mean + n \times SD]$$

where n can take the value 1, 2 or 3, depending on the desired sensitivity for latter patient threshold.

4.2.3. Control Variability

Subject data from the control group were studied in order to evaluate how much it varied among the subjects.

Variability assessment of the control group enables the subsequent usage to identify alterations present in the patients brains due to the tumour presence. In order to verify how much the built groups varied, mean and SD values were plotted for each connectivity/ imaging metric.

4.3. Patient group analysis

For both approaches, each patient was studied individually considering the application of normal variation ranges built from the whole control group data and from gender-matched data. Considering these ranges, in order to analyse the data, an approximation to a normal distribution was used. However, due to the nature of this study (first approach to whole-brain analysis with multimodal data), and to the small control sample size ($N = 22$ for the all subjects and $N = 11$ for the gender-based groups), it is not possible to ensure data normality, thus uncorrected p-values relative to 1, 2 and 3 deviations from the mean were used, which give us: p-value (unc.) = 0.159, 0.025, 0.0015.

Conjoint patient analysis was not performed since regional changes could be masked due to the differences introduced by the presence of glioblastoma in each patient.

4.3.1. Intrahemispheric differences

Similarly to the procedure presented in subsection 4.2.1, the AI was calculated for the connectivity metrics applying equation 4.1, using individual patient data. With regard to fibre counts, equation 4.2, also from subsection 4.2.1 was used in order to obtain the fibres counts difference.

In order to assess regional changes for the studied regions regarding the evaluated metrics, the normal range intervals built in subsection 4.2.1 were used, with three different threshold levels (one, two and three times the calculated error). Resultant data were visualised in a connectogram, showing the cortical and subcortical structures only on the lesion side.

4.3.2. Whole-brain assessment

For this case, individual patient values for each one of the metrics were masked using the range presented in subsection 4.2.2. Significant changes corresponded to ROIs with metric values that would fall off the used range.

Resultant data were visualised in a connectogram assessing changes of the patient values when compared to the mean value of the control group as shown in:

$$visualised\ value = \frac{P_v - C_{av}}{C_{av}},$$

with P_v the patient metric value for each structure and C_{av} the corresponding average value of the used control group. These connectograms show cortical and subcortical structures of the whole brain.

5. Analysis in control subjects

In this section, the previous built groups were evaluated in order to look for differences among them.

In appendix A additional data concerning the distribution of the individual control values, in the intrahemispheric and whole-brain cases, versus the different built ranges is presented. In figures A.1 and A.2 the intrahemispheric data were gathered and plotted against the corresponding calculated error, and in figures A.3 and A.4, the left and right-sided structures individual values against the standard deviation of the group-corresponding data.

5.1. Results

In figures 5.1 and 5.2 the control group mean values for each structures and corresponding SD are plotted for all studied connectivity metrics (CtxT, FA, MD, ClusC, Deg). In each graphic, values for the full, only females and only males controls were presented.

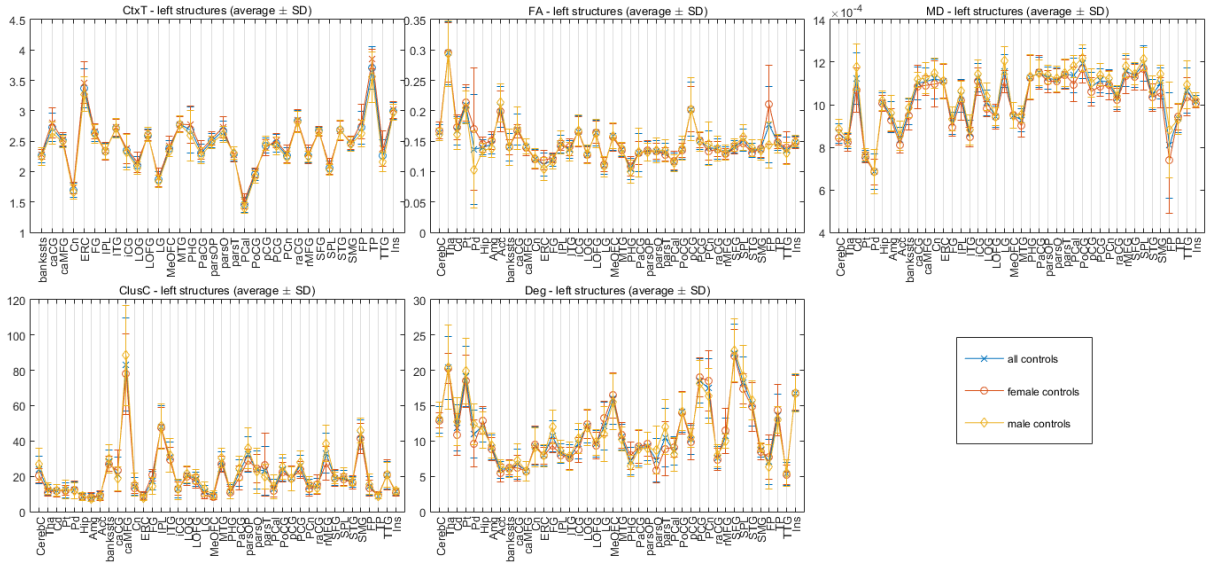

Figure 5.1.: Mean values of individual left-sided structures for each studied metric. Error bars correspond to the standard deviation values. Cortical thickness (CtxT) and mean diffusivity (MD) are presented in mm and mm^2/s, respectively. Blue, orange and yellow correspond to data from the full control group ($N = 22$), only female subjects ($N = 11$) and only male subjects ($N = 11$), respectively.

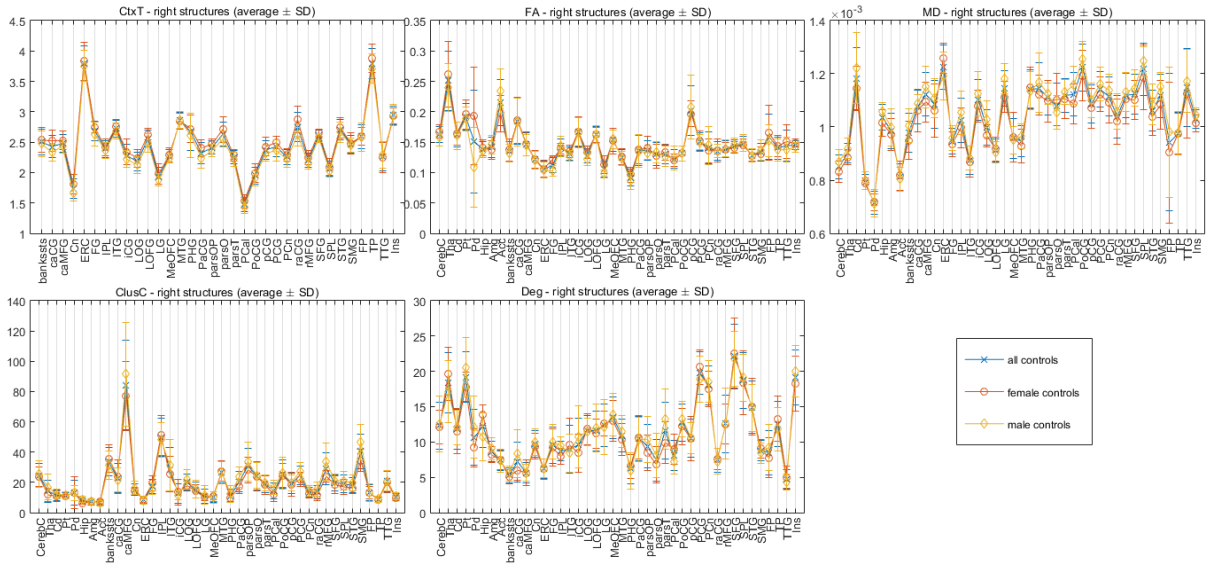

Figure 5.2.: Mean values of individual right-sided structures for each studied metric. Error bars correspond to the standard deviation values. Cortical thickness (CtxT) and mean diffusivity (MD) are presented in mm and mm^2/s, respectively. Blue, orange and yellow correspond to data from the full control group ($N = 22$), only female subjects ($N = 11$) and only male subjects ($N = 11$), respectively.

5.2. Considerations

Graphics in figures 5.1 and 5.2 show a similar behaviour concerning values measured in each structure across all groups. Looking at mean values for each one of the gender-based groups, the male group shows consistently slightly higher values in metrics derived from DTI (additional increased SD [e.g. FA - Acc, pCG; MD, ClusC and Deg - consistent for most regions]). It has been recognised that the male human brain is in overall larger, and that females have a higher proportion of grey matter [73]. The slightly increased value of CtxT in the female group, in some regions (with additional increased SD [e.g. in the ERC, TP and raCG]) could be explained by the fact presented before. On the other hand, while differences regarding white matter have not been as studied as grey matter [74], some studies point the occurrence of differences gender-based [73, 75]. Measures based from DTI are not only influenced by gender but also by age. Studies suggest that with ageing, there is loss of microstructural white matter organization, which leads to loss of anisotropy in the medium, thus, consequently loss of FA, especially in anterior regions, accompanied by increased MD [76]. Due to the control group range of ages, one could expect to be in presence of anisotropy loss in older controls which could explain some larger standard deviation values observed in anterior regions of the brain (such as areas from the frontal lobe) [76].

Due to the differences described above between the male and female brain a gender-matched analysis was proposed, in order to account for that variability.

6. Gliobastoma patient analysis

In the following section results for the patient analysis are presented and discussed considering the usage of a full and gender-matched control group.

Results include connectograms with p-values (unc.) of 0.159 and 0.0015 for a intrahemispheric differences and whole-brain analysis, respectively, which correspond to the application of 1thres and 3 SD (3 times the standard deviation), respectively. For each of these cases two different connectograms groups were obtained, using the whole and gender-matched analysis approach.

Additional connectograms results with the three threshold levels created in chapter 4 concerning the patient analysis can be found in appendices D. In figures D.1 and D.2 we have additional connectograms for left and right-sided lesions for intrahemispherical differences using the full control group and in figures D.3 and D.4 with the gender-matched group. In figures D.5 and D.6, for left and right-sided for whole-brain analysis when using the full control group, and figures D.7 and D.8 with the gender-matched group.

It is also important to notice that reported findings in point "*2. Gender-matched data*" for each subject - in both approaches - only mention metrics' alterations that follow one of the cases: **(1)** not observed when using the full control group; **(2)** not observed when using the gender-matched, but reported with the full group.

6.1. Intrahemispheric differences

6.1.1. Results

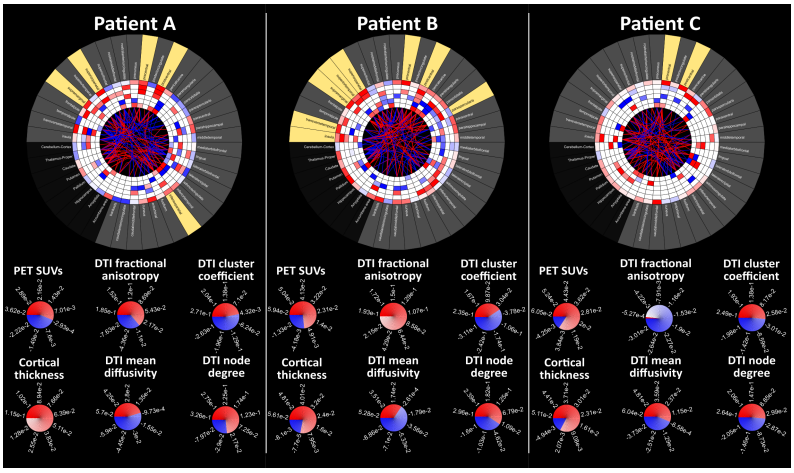

Figure 6.1: Figure is continued in the next page.

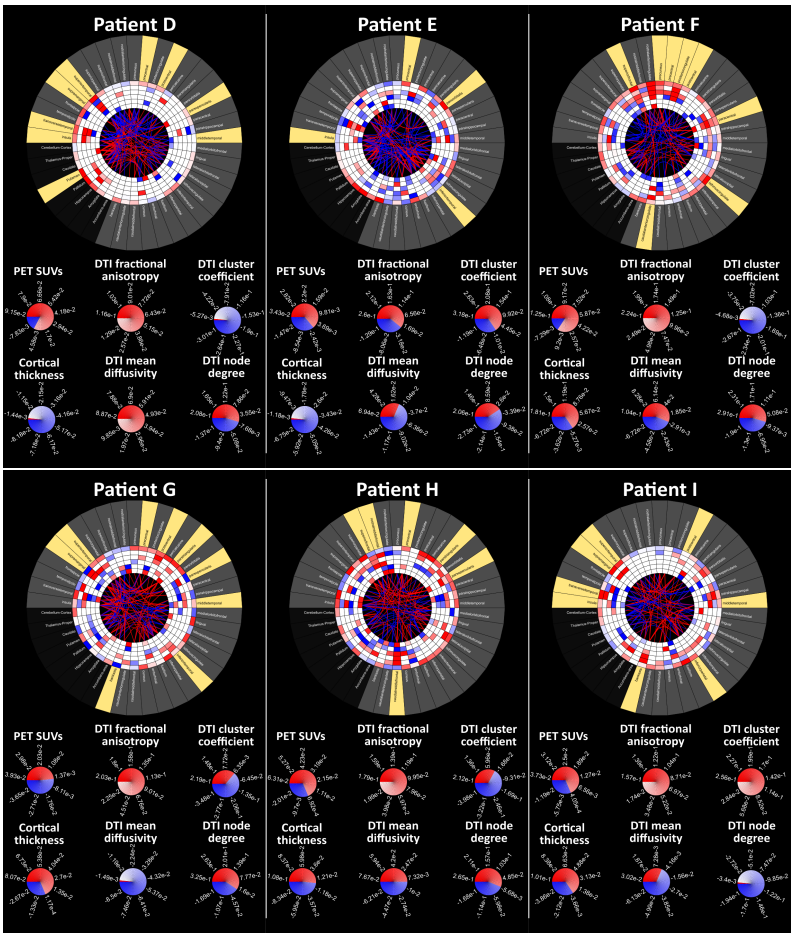

Figure 6.1 ***(previous page)*****:** Connectograms with patients' AI data using the whole control group (p-val (unc.) = 0.159). From the outer to the inner rings we have: cortical (dark grey) and subcortical (black) regions/structures; SUV; CtxT; FA; MD; Deg and ClusC. Connections in the middle correspond to DTI tractography. Regions in yellow represent peritumoural sites.
Values presented in these connectograms represent the differences between left/right and right/left structures for patients A to E/F to I, regarding studied imaging and connectivity metrics.
Patients A to E/F to I: Red/Blue blocks/lines - left/right hemispherical ROI presents higher/lower values than the right/left hemispherical ROI; White - differences are within the normal variation range.
Information concerning affected regions is available in table E.1 (appendix E).

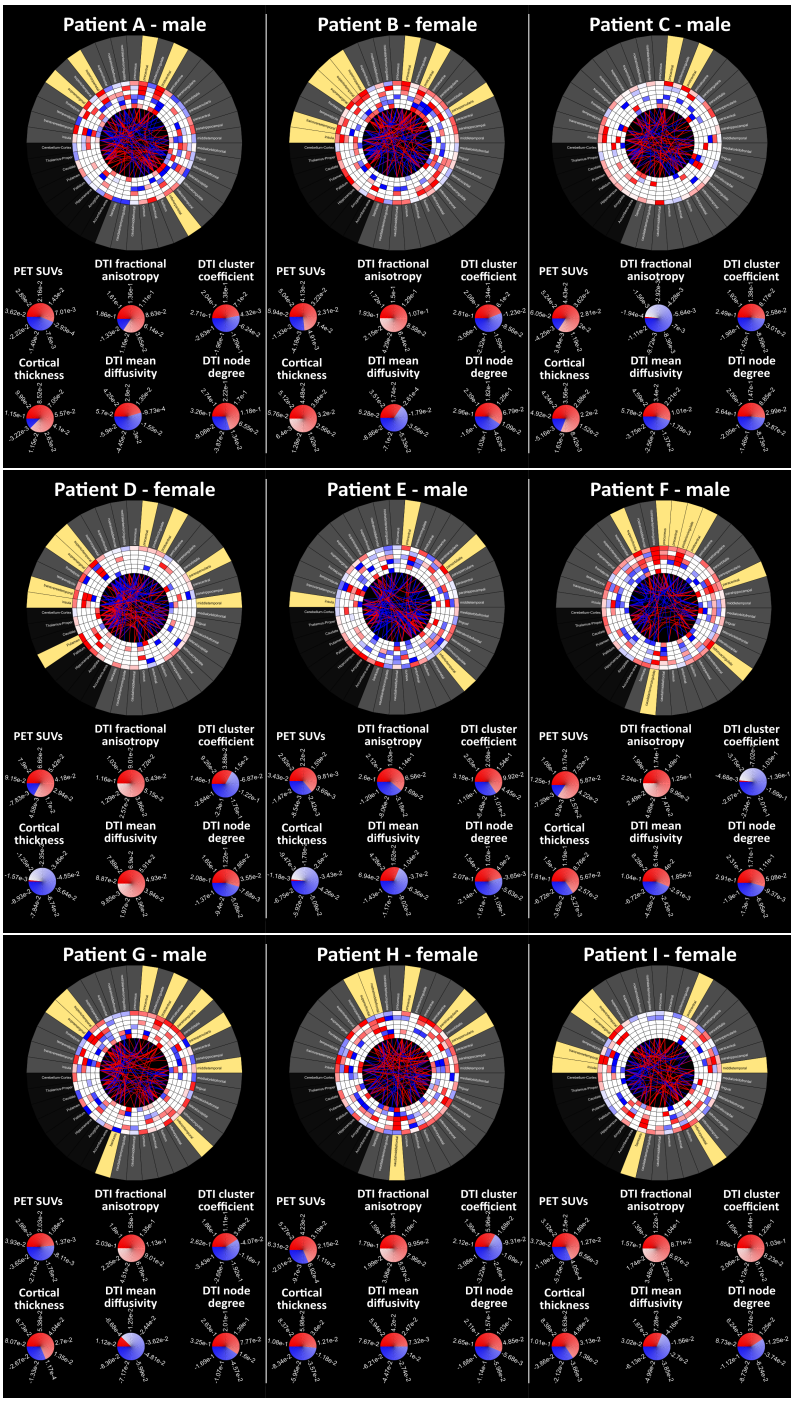

Figure 6.2.: Connectograms with patients' AI data using the gender-matched control groups (p-val (unc.) = 0.159). From the outer to the inner rings we have: cortical (dark grey) and subcortical (black) regions/structures; SUV; CtxT; FA; MD; Deg and ClusC. Connections in the middle correspond to DTI tractography. Regions in yellow represent peritumoural sites.
Values presented in these connectograms represent the differences between left/right and right/left structures for patients A to E/F to I, regarding studied imaging and connectivity metrics.
Patients A to E/F to I: Red/Blue blocks/lines - left/right hemispherical ROI presents higher/lower values than the right/left hemispherical ROI; White - differences are within the normal variation range.
Information concerning affected regions is available in table E.2 (appendix E).

6.1.2. Discussion

6.1.2.1. Patient A

[Lesion region: left Parietal lobe. Peritumoural regions: postcentral, precentral and supra marginal gyrus, and inferior and superior parietal lobule.]

1. Non gender-matched analysis

Regarding structural connectivity (figure 6.1), increased number of fibres were identified in connections with peritumoural regions. These include connections between the postcentral/ thalamus, and middle and inferior temporal gyrus; the precentral/ insula; the superior parietal lobule/ inferior temporal gyrus; and the inferior parietal lobule/ thalamus, and insula. Decreased number of fibres were identified between the superior parietal lobule/ rostral middle frontal gyrus, and putamen; the supramarginal gyrus/ pars opercularis; and the inferior parietal lobule/ rostral middle frontal gyrus and pars opercularis. Alterations in connections between other frontal and subcortical structures and between temporal and parietal structures distant to the tumour region were also registered.

Concerning connectivity/ imaging metrics (figure 6.1), there are noticeable differences at 1thres for all metrics. Changes in peritumoural regions included increased cortical thickness (CtxT), fractional anisotropy (FA) and node degree (Deg) in the precentral and postcentral gyrus, and FA and clustering coefficient (ClusC) in the supramarginal gyrus. increased FA and Deg were also identified in the superior and inferior parietal lobule. Additional FA changes were found at 2thres in the superior parietal lobule and precentral gyrus. Other changes in spatially distant regions were also identified (available in table E.1).

2. Gender-matched analysis

In terms of structural connectivity (figure 6.2), additional increased number of fibres in connections between the postcentral gyrus/ thalamus; and the precentral gyrus/ putamen were identified. Decreased number of fibres was also observed in the connection between the superior parietal lobule/ superior temporal gyrus.

Additional changes in connetivity/ imaging metrics (figure 6.2) included findings concerning increased CtxT and decreased mean diffusivity (MD) in the superior parietal lobule. Decreased MD values were additionally found in the inferior parietal lobule, precentral and postcentral gyrus, and decreased Deg in the supramarginal gyrus (this information, plus alterations in distant sites, are compiled in table E.2).

6.1.2.2. Patient B

[Lesion region: left Parietal lobe. Peritumoural regions: postcentral, precentral, supra marginal, superior and transverse temporal gyrus, pars opercularis, insula and superior parietal lobule.]

1. Non gender-matched analysis

Structural connectivity (figure 6.1) changes included alterations in connections between various structures. Concerning connections related to peritumoural regions, increased number of fibres were found between the insula/ putamen, lateral orbitofrontal cortex, postcentral gyrus and pars opercularis; supramarginal/ inferior and superior temporal, and postcentral gyrus; the superior temporal/ postcentral and inferior temporal gyrus, and pars orbitalis; the superior parietal

lobule/ banks of the superior temporal sulcus, inferior temporal and lateral occipital gyrus; the precentral/ superior frontal gyrus and pars opercularis; the banks of the superior temporal sulcus/ thalamus; and the pars opercularis/ caudal medial frontal cingulate. Decreased number of fibres were found in connections between the insula/ rostral anterior cingulate and paracentral gyrus; and the superior temporal gyrus/ inferior parietal lobule. Alterations in other structures included reduction in the number of fibres between subcortical structures such as between the caudate and parietal/ frontal regions. Connections with regions from the parietal lobe also present more changes concerning a higher number of fibres to structures from the lesion side.

Changes in all connectivity/ imaging metrics (figure 6.1) were present at 1thres. Regarding peritumoural regions, changes in fractional anisotropy (FA) included increased values in pars opercularis, postcentral and supramarginal gyrus, and insula. mean diffusivity (MD) changes included increased values in postcentral gyrus and decreased in pars opercularis and transverse temporal gyrus. Decreased clustering coefficient (ClusC) was identified in postcentral and superior temporal gyrus, and increased node degree (Deg) in superior temporal and postcentral gyrus, and in superior parietal lobule. At 2thres, changes were only identified in FA and MD metrics, with changes in peritumoural regions comprising increased FA in pars opercularis, and at 3thres no changes were identified. Remaining changes were identified in regions distant to the tumour (available in table E.1).

2. Gender-matched analysis

Additional changes in structural connectivity (figure 6.2) comprised increased number of fibres in the connections between the supramarginal gyrus/ superior parietal lobule; and the pars opercularis/ caudal middle frontal gyrus and pallidum. Decreased number of fibres were identified between the precentral/ paracentral and superior temporal gyrus, and inferior parietal lobule; the superior parietal lobule/ precuneus; and the insula/ entorhinal.

Connectivity/ imaging metrics (figure 6.2) differences included the absence of reduced MD in the pars opercularis. On the other hand, additional findings regarding increased Deg and decreased ClusC were identified in the supramarginal gyrus, and increased cortical thickness (CtxT) in the precentral gyrus (this information, plus alterations in distant sites, are compiled in table E.2).

6.1.2.3. Patient C

[Lesion region: left Parietal lobe. Peritumoural regions: precentral and postcentral gyrus.]

1. Non gender-matched analysis

This subject presents the least significant differences concerning both structural connectivity (figure 6.1) and connectivity/ imaging metrics.

Structural connectivity differences show increased number of fibres in connections between the precentral/ putamen, and the caudal middle frontal gyrus; and the postcentral/ paracentral gyrus.

Connectivity/ imaging metrics showed differences through all metrics at 1thres, with the following changes in peritumoural regions: reduced cortical thickness (CtxT) in the precentral gyrus, mean diffusivity (MD) in the precentral and postcentral gyrus; and in increased clustering coefficient (ClusC) in precentral gyrus. Remaining changes were registered in regions spatially distant to the tumour location (available in table E.1).

2. Gender-matched analysis

Regarding structural connectivity (figure 6.2) a single additional occurrence of increased number of fibres between the precentral/ caudate was observed.

No additional changes in connectivity/ imaging metrics (figure 6.2) were found (this information, plus alterations in distant sites, are compiled in table E.2).

6.1.2.4. Patient D

[Lesion region: left Temporal lobe. Peritumoural regions: supra marginal, postcentral, precentral, superior, medial and transverse temporal gyrus, pars opercularis, putamen and insula.]

1. Non gender-matched analysis

Structural connectivity (figure 6.1) changes included increased number of fibres in connections between the putamen/ insula, entorhinal, transverse temporal, superior temporal, rostral middle frontal and lateral occipital gyrus; the insula/ postcentral gyrus, pars opercularis, inferior parietal lobule, pallidum and superior entorhinal; the transverse temporal gyrus/ inferior parietal gyrus and pallidum; the supramarginal/ superior temporal and lateral occipital gyrus; the superior temporal/ fusiform gyrus, medial orbitofrontal cortex, accumbens, hippocampus, pallidum, caudate and temporal pole; the postcentral gyrus/ caudate; and between the pars opercularis/ triangularis, Connections with reduced number of fibres were found between the putamen/ superior frontal and precentral gyrus; the insula/ superior parietal lobule, pars triangularis and operculais, supeior frontal and rostral middle frontal gyrus; the transverse temporal/ precentral gyrus and superior parietal loobule; the superior temporal/ postcentral gyrus and superior parietal lobule; the precentral gyrus/ pallidum; the pars opercularis/ supeior parietal lobule; and between the medial temporal gyrus/ superior parietal lobule. An overall increase of the number of fibres was identified in connections related to subcortical structures, and reduced number of fibres in conenctions with the superior parietal lobule, superior frontal and rostral middle frontal gyrus.

Connectivity/ imaging (figure 6.1) metrics changes were observed for all metrics at 1thres. Peritumoural regions metrics alteration included decreased cortical thickness (CtxT) and clustering coefficient (ClusC) in the superior temporal gyrus, with additional changes in ClusC found in the transverse temporal and superior temporal gyrus. Increased fractional anisotropy (FA) and mean diffusivity (MD) were identified in the insula, transverse temporal and superior temporal gyrus and additionally for MD in the putamen. Increased node degree (Deg) was found in the pars opercularis. At 2thres only changes in increased FA survived with significant differences in the insula and transverse temporal gyrus. Remaining changes at 1thres in places significantly to the tumour were observed for all metrics (available in table E.1).

2. Gender-matched analysis

In terms of changes in structural connectivity (figure 6.2) no longer observed we identified the increased number of fibres between the insula/ postcentral gyrus; superior temporal gyrus/ hippocampus; and pars opercularis/ pars triangularis. Additional changes included increased values between the putamen/ supramarginal gyrus; the insula/ pars opercularis, inferior parietal lobule, entorhinal; the supramarginal/ superior temporal gyrus; the superior temporal gyrus/ putamen; and the pars opercularis/ caudal middle frontal gyrus.

Additional connectivity/ imaging metrics (figure 6.2) findings included increased and decreased

ClusC in the pars opercularis and medial temporal gyrus, respectively, and decreased Deg in the putamen (this information, plus alterations in distant sites, are compiled in table E.2).

6.1.2.5. Patient E

[Lesion region: left temporal lobe. Peritumoural regions: insula, pars ocularis, precentral and inferior temporal gyrus.]

1. Non gender-matched analysis

Structural connectivity changes (figure 6.1) in connections related to peritumoural regions included increased number of fibres between the inferior temporal/ postcentral, supramarginal and superior temporal gyrus; and the insula/ caudate, putamen and pallidum. Reduced number of fibres were identified between the inferior temporal/ transverse temporal and fusiform gyrus, and the bank of the temporal sulcus; the precentral/ supramarginal gyrus; and between the insula/ cerebellum, thalamus, hippocampus, fusiform, paracentral, superior frontal, rostral middle frontal and the rostral anterior cingulate gyrus.

Connectivity/ imaging metrics changes (figure 6.1) were identified throughout all metrics at 1thres for both local and distant regions relative to the tumour. Peritumoural changes included reduced cortical thickness (CtxT), and increased fractional anisotropy (FA), mean diffusivity (MD) and node degree (Deg) values in the inferior temporal gyrus. Increased MD was also identified in the pars orbitalis; reduced FA in the precentral gyrus; and increased clustering coefficient (ClusC) and decreased Deg ub the insula. At 2thres no changes were identified for CtxT and FA, and increased MD values were identified in pars orbitalis and the inferior temporal gyrus. Finally, at 3thres, single FA changes for spatially distant regions were found (available in table E.1).

2. Gender-matched analysis

Structural connectivity (figure 6.2) changes no longer reflected increased number of fibres in the connection between the inferior temporal gyrus/ insula, but instead a reduced value of this metric. Additional increased value of this metric was identified between the insula/ postcentral gyrus.

Regarding additional connectivity/ imaging metrics (figure 6.2) decreased MD value in the postcentral gyrus was found (this information, plus alterations in distant sites, are compiled in table E.2).

6.1.2.6. Patient F

[Lesion region: right Frontal lobe. Peritumoural regions: superior frontal, precentral, posterior central, postcentral, paracentral, isthmus of the cingulate and caudal anterior cingulate gyrus, and precuneus.]

1. Non gender-matched analysis

Structural connectivity alterations (figure 6.1) reflected increased number of fibres in connections between the caudal anterior cingulate gyrus/ thalamus; the isthmus of the cingulate/ posterior cingulate and paracentral gyrus, cuneus and precuneus; the postcentral/ rostral middle frontal and superior frontal gyrus; and between the precuneus/ hippocampus. Decreased number of fibres were found in connection between the isthmus of the cingulate/ superior frontal gyrus;

the postcentral/ medial temporal gyrus, insula and the banks of the superior temporal sulcus; the posterior cingulate gyrus/ accumbens; the precentral/ medial temporal gyrus; and between the precuneus gyrus/ lateral orbitofrontal cortex.

Concerning connectivity/ imaging metrics (figure 6.1), changes were identified at 1thres, with increased cortical thickness (CtxT), fractional anisotropy (FA), mean diffusivity (MD) and node degree (Deg) in the superior frontal and paracentral gyrus. Increased CtxT and FA were also found in the precuneus and posterior cingulate, and in the isthmus of the and caudal anterior cingulate gyrus for CtxT. Other tumour-related regions with increased FA and decreased MD values were the precentral and postcentral gyrus, and increased MD values in the posterior cingulate gyrus. At 2thres no changes were identified in both clustering coefficient (ClusC) and Deg. Concerning increased CtxT and FA values, these were identified in the superior frontal gyrus, and increased CtxT and MD in the posterior cingulate and caudal anterior cingulate gyrus. Increased FA and decreased MD were found in the precentral gyrus, and decreased MD in the postcentral gyrus. At 3thres only changes in CtxT survived, showing differences in the posterior central and caudal anterior cingulate gyrus (available in table E.1).

2. Gender-matched analysis

Differences found before for increased structural connectivity in connections related to the caudal cingulate gyrus were no longer identifiable. Additional increased number of fibres was observed between the postcentral gyrus/ pars opercularis, precuneus. Reduced number of fibres in connections between the postcentral/ transverse temporal gyrus: and the precentral gyrus/ pars triangularis, were additionaly found.

Regarding additional connectivity/ imaging metrics (figure 6.2) decreased Deg value in the isthmus of the cingulate gyrus was found (this information, plus alterations in distant sites, are compiled in table E.2).

6.1.2.7. Patient G

[Lesion region: right Temporal lobe. Peritumoural regions: supra marginal, precentral, postcentral, inferior, medial and superior temporal gryus, pars opercularis and triangularis, and banks of the temporal sulcus.]

1. Non gender-matched analysis

Changes in structural connectivity (figure 6.1) showed significant differences in the number of fibres in multiple connections, including ones related with peritumoural regions. Increased number of fibres were found between the supra marginal/ transverse temporal, inferior temporal and postcentral gyrus, insula, putamen, bank of the temporal sulcus, and pars triangularis; the superior temporal gyrus/ putamen, and bank of the superior temporal sulcus; the precentral gyrus/ pars triangularis and opercularis; the postcentral/ superior frontal gyrus, and pars opercularis; the pars triangularis/ superior parietal lobule, transverse temporal and caudal middle frontal gyrus; the pars opercularis/ insula; and between the medial temporal/ laateral occipital and inferior temporal gyrus. Decreased number of fibres were found in connections between the medial temporal gyrus/ medial orbitofrontal cortex and pallidum; the inferior temporal gyrus/ thalamus; and the bank of the temporal sulcus/ superior temporal lobule.

Regarding connectivity/ imaging metrics (figure 6.1), changes in all metrics were identified at 1thres, including alterations in peritumoural regions. Increased cortical thickness (CtxT) and fractional anisotropy (FA) values were found in the supramarginal, postcentral and inferior

temporal gyrus; increased FA and clustering coefficient (ClusC) in the medial temporal gyrus. At 2thres no alterations in CtxT, ClusC and node degree (Deg) were registered, and increased FA values were found in the supramarginal, superior temporal and medial temporal gyrus, and in the pars opercularis. At 3thres no changes were found. Remaining changes at both 1thres and 2thres were identified in spatially distant regions (available in table E.1).

2. Gender-matched analysis

Regarding structural connectivity (figure 6.2) previous changes related to increased values in connections with the precentral gyrus were found. On the other hand, additional findings included increased number of fibres in connections between the supramarginal/ medial temporal and inferior temporal gyrus; the superior temporal/ postcentral gyrus; and the precentral gyrus/ pars triangularis. Reduced number of fibres were found between the precentral gyrus/ insula; the medial temporal gyrus/ medial orbitofrontal cortex; inferior temporal gyrus/ entorhinal; and the banks of the temporal sulcus/ superior parietal lobule.

Additional changes regarding connectivity/ imaging metrics (figure 6.2) included increased mean diffusivity (MD) and Deg values in the supramarginal gyrus, and increased ClusC in the banks of the temporal sulcus (this information, plus alterations in distant sites, are compiled in table E.2).

6.1.2.8. Patient H

[Lesion region: right Frontal lobe. Peritumoural regions: precentral, caudal middle, rostral and superior frontal gyrus, and pars opercularis and trinagularis.]

1. Non gender-matched analysis

Structural connectivity changes (figure 6.1) occurred in both local and distant regions to the tumour. Regarding alterations in connections with peritumoural regions, these included increased number of fibres between the superior frontal/ rostral middle frontal gyrus and lateral orbitofrontal cortex, and pallidum; the rostral middle frontal gyrus/ pars opercularis; the precentral/ caudal middle frontal gyrus, pars opercularis and insula; the pars triangularis/ opercularis, and lateral orbitofrontal cortex; the pars opercularis/ postcentral gyrus; and the caudal middle frontal/ medial temporal gyrus, pallidum and the banks of the temporal sulcus. Reduced number of fibres were found between the superior frontal gyrus/ accumbens, putamen and insula; the precentral/ inferior temporal gyrus; the pars opercularis/ inferior temporal gyrus; and the caudal middle frontal gyrus/ insula.

Changes in connectivity/ imaging metrics (figure 6.1) were registered for all studied metrics at 1thres, including significant findings in peritumoural regions. Increased cortical thickness (CtxT), fractional anisotropy (FA), mean diffusivity (MD) and node degree (Deg) were found in the superior frontal and caudal middle frontal gyrus, and pars opercularis. The rostral middle frontal gyrus also presented increased CtxT, FA and Deg. Increased FA values were also identified in pars triangularis. Reduced clustering coefficient (ClusC) values were identified in the rostral middle frontal and caudal middle frontal gyrus. At 2thres no ClusC and Deg significant changes were identified. Regarding increased CtxT and FA, these were found in caudal middle frontal gyrus for both metrics, and in superior frontal and rostral middle frontal gyrus for CtxT, and in pars opercularis for FA. Finally, at 3thres, only CtxT significant changes were identified, in the same peritumoural regions found at 2thres. Other changes in regions spatially distant to the tumour were also identified (available in table E.1).

2. Gender-matched analysis

Regarding structural connectivity decreased number of fibres between the superior frontal gyrus/ putamen was no longer identifiable.

Connectivity/ imaging metrics (figure 6.2) differences include the absence of reduced MD in the pars triangularis. On the other hand, additional findings regarding decreased CtxT value in the precentral gyrus were identified (this information, plus alterations in distant sites, are compiled in table E.2).

6.1.2.9. Patient I

[Lesion region: right Temporal lobe. Peritumoural regions: supra marginal, medial, transversal and superior temporal, and postcentral gyrus, banks of the temporal sulcus and inferior parietal lobule.]

1. Non gender-matched analysis

Structural connectivity (figure 6.1) significant differences were found between both local and distant regions. Regarding the connections including peritumoural regions, increased number of fibres were identified between the insula/ inferior parietal lobule; the supramarginal/ precentral and inferior temporal gyrus; the superior temporal/ inferior temporal gyrus; the medial temporal/ inferior temporal gyrus, and the bank of the temporal sulcus; and the inferior parietal lobule/ putamen, and the bank of the temporal sulcus. Reduced number of fibres were identified between the insula/ temporal pole and pallidum; the postcentral gyrus/ thalamus; and the medial temporal gyrus/ pars opercularis.

Regarding connectivity/ imaging metrics (figure 6.1), at 1thres, increased cortical thickness (CtxT), fractional anisotropy (FA) and mean diffusivity (MD) were identied in the bank of the temporal sulcus. Other significant changes regarding increased values included the tranverse temporal gyrus for CtxT and the supramarginal, superior temporal, postcentral and medial temporal gyrus, and the inferior parietal lobule for FA. Reduced MD and node degree (Deg) were identied in insula, and additionally in the transverse temporal gyrus for MD. At 2thres no CtxT, clustering coefficient (ClusC) and Deg differences were significant. At this level increased FA was identified in the insula, bank of the temporal sulcus, supramarginal, superior temporal and medial temporal gyrus and decreased MD values were found in the insula and supramarginal gyrus. At 3thres no significant changes were identified. Other changes in regions spatially distant to the tumour were also identified (available in table E.1).

2. Gender-matched analysis

Regarding structural connectivity (figure 6.2) increased number of fibres was found additionally in connections between the supramarginal gyrus/ pars opercularis and putamen; and the superior temporal gyrus/ pars triangularis. Decreased values were observed in connections between the insula/ pars orbitalis; and the postcentral gyrus/ caudate.

Regarding additional connectivity/ imaging metrics (figure 6.2) increased Deg value in the banks of the temporal sulcus was identified (this information, plus alterations in distant sites, are compiled in table E.2).

6.2. Whole-brain connectivity assessment

6.2.1. Results

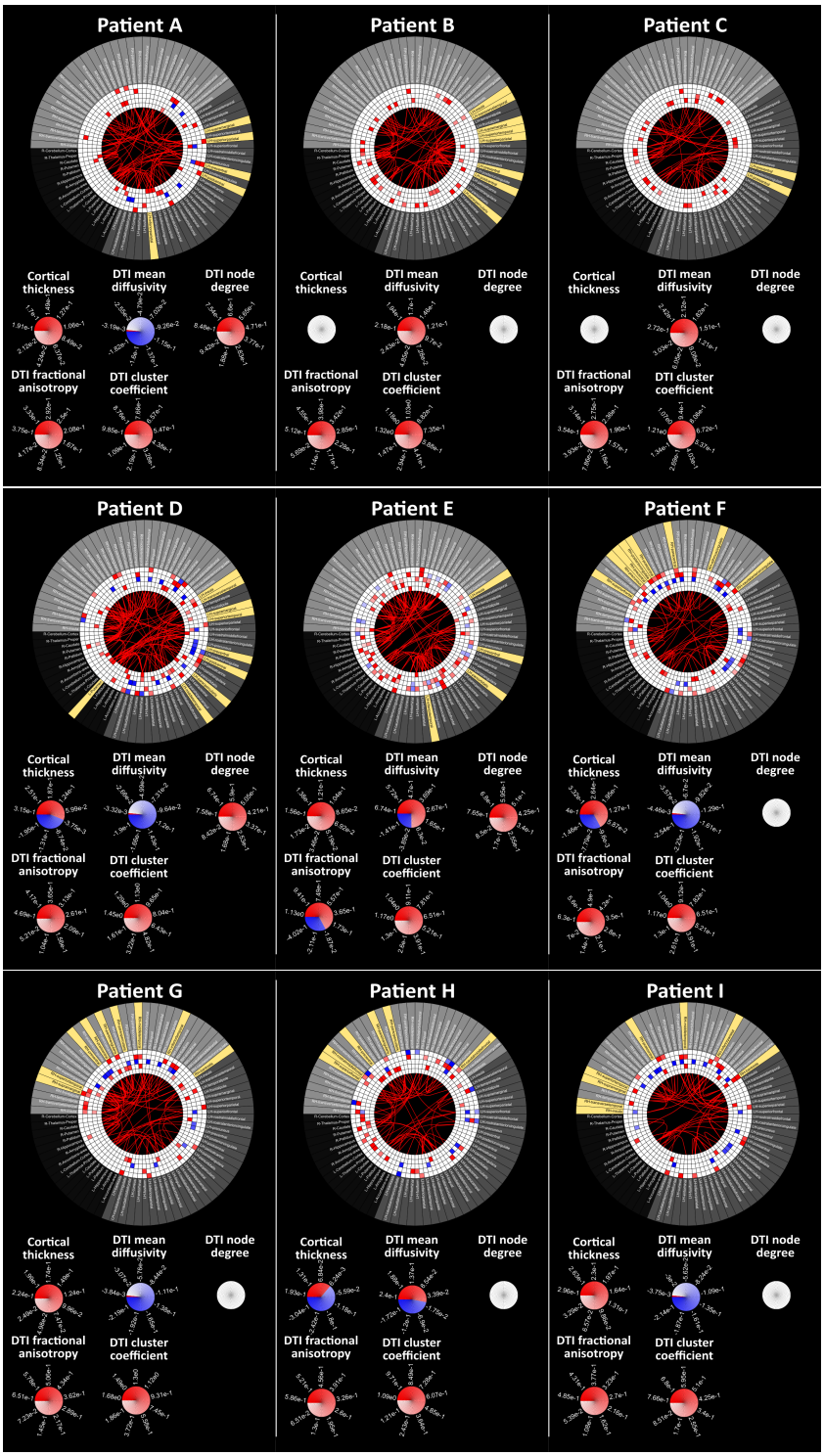

Figure 6.3 ***(previous page)*****:** Connectograms with data for all patients, using the whole control group (p-val (unc.) = 0.0015). From the outer to the inner rings we have: left (dark grey) and right (light grey) cortical and subcortical (black) regions/structures; SUV; CtxT; FA; MD; Deg and ClusC. Connections in the middle correspond to DTI tractography. Regions in yellow represent the peritumoural sites.
Values presented in these connectograms represent the increased or decreased ratio of the patient values related to the mean value of the control group. Red/Blue blocks/lines - ROI presents higher/lower values than the mean value of the control group; White - values are within the normal variation range.
Information concerning affected regions is available in table E.3 (appendix E).

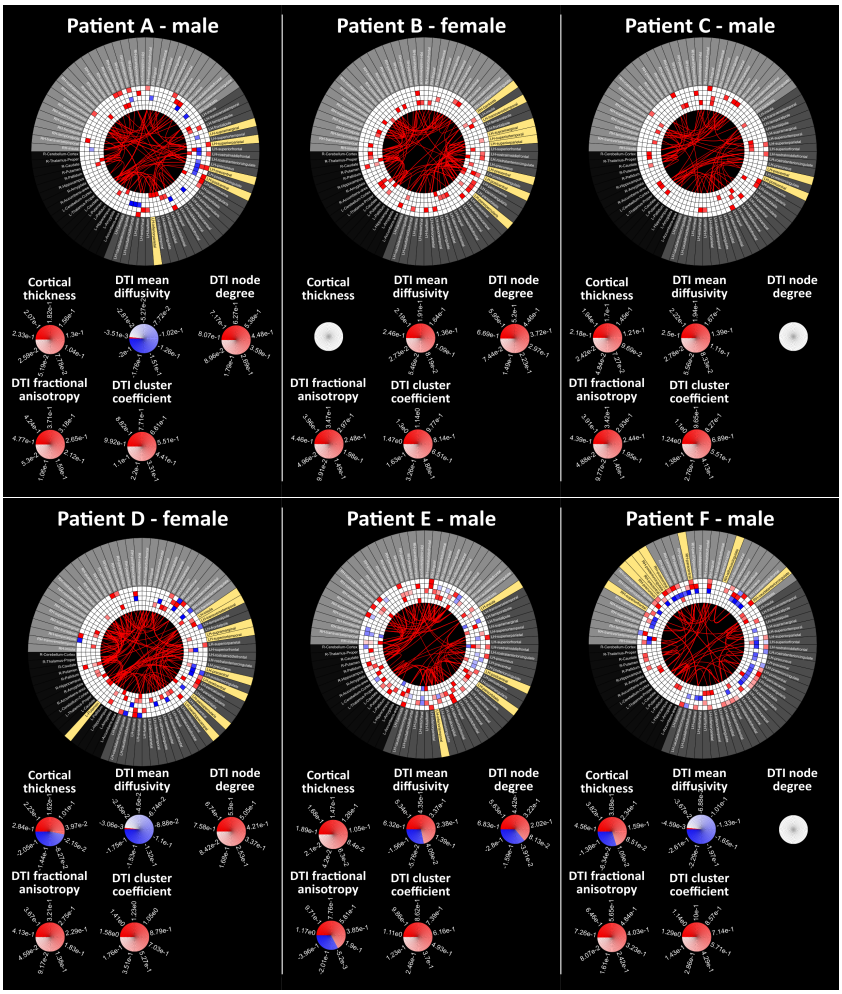

Figure 6.4: Figure is continued in the next page.

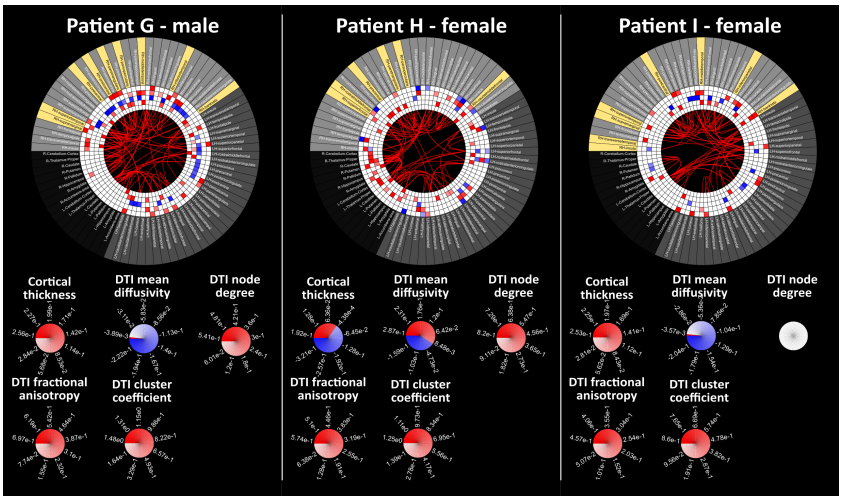

Figure 6.4 ***(previous page)*****:** Connectograms with data for all patients, using the gender-matched control groups (p-val (unc.) = 0.0015). From the outer to the inner rings we have: left (dark grey) and right (light grey) cortical and subcortical (black) regions/structures; SUV; CtxT; FA; MD; Deg and ClusC. Connections in the middle correspond to DTI tractography. Regions in yellow represent the peritumoural sites.
Values presented in these connectograms represent the increased or decreased ratio of the patient values related to the mean value of the control group. Red/Blue blocks/lines - ROI presents higher/lower values than the mean value of the control group; White - values are within the normal variation range.
Information concerning affected regions is available in table E.4 (appendix E).

6.2.2. Discussion

6.2.2.1. Patient A

[Lesion region: left Parietal lobe. Peritumoural regions: postcentral, precentral and supra marginal gyrus, and inferior and superior parietal lobule.]

1. Non gender-matched analysis

Structural connectivity (figure 6.3) reflects an increased number of fibres throughout the whole brain.

Connectivity/ imaging metrics (figure 6.3) changes were registered for all studied metrics, with increased cortical thickness (CtxT), fractional anisotropy (FA), clustering coefficient (ClusC) and node degree (Deg) and decreased values for mean diffusivity (MD) in peritumoural regions. Increased values were identified in precentral gyrus for CtxT and FA, postcentral gyrus and superior parietal lobular for CtxT and inferior parietal lobular for Deg, and decreased values in the precentral gyrus for ClusC. Other changes in regions spatially distant to the tumour, in both hemispheres, were also identified in the referred metrics (available in table E.3).

2. Gender-matched analysis

No significant differences regarding findings in the non gender-matched analysis were found for structural connectivity (figure 6.4).

Regarding connectivity/ imaging metrics (figure 6.4), additional peritumoural regions with changes include increased CtxT in the inferior parietal lobular and decreased MD values in the postcentral and supra marginal gyrus. Other regions spatially distant to the tumour in both hemispheres presented changes in the metrics referred before (this information, plus alterations in distant sites, are compiled in table E.4).

6.2.2.2. Patient B

[Lesion region: left Parietal lobe. Peritumoural regions: postcentral, precentral, supra marginal, superior and transverse temporal gyrus, pars opercularis, insula and superior parietal lobule.]

1. Non gender-matched analysis

Regarding structural connectivity (figure 6.3) changes reflected in increased number of fibres, with more connections in temporal and parietal regions from the left hemisphere.

Connectivity/ imaging metrics (figure 6.3) changes in peritumoural regions included increased values in the insula and pars opercularis for fractional anisotropy (FA), postcentral gyrus for mean diffusivity (MD), and precentral and transverse temporal gyrus for clustering coefficient (ClusC). Other changes in regions spatially distant to the tumour, in both hemispheres, were identified, mostly in parietal and temporal structures, and additionally subcortical structures with significant alterations in MD values (available in table E.3).

2. Gender-matched analysis

Structural connectivity (figure 6.4) findings relative to the full group approach showed increased number of fibres in fewer connections between left-sided structures.

Concerning connectivity/ imaging metrics (figure 6.4), additional findings included increased values in the postcentral gyrus for FA and node degree (Deg), in the superior temporal gyrus for FA, in the transverse temporal gyrus for MD and in the pars opercularis for ClusC. However, the transverse temporal gyrus does show increased ClusC with the gender-matched data. Other changes include structures of both hemispheres spatially distant to the tumour in parietal and temporal regions, namely concerning Deg findings (this information, plus alterations in distant sites, are compiled in table E.4).

6.2.2.3. Patient C

[Lesion region: left Parietal lobe. Peritumoural regions: precentral and postcentral gyrus.]

1. Non gender-matched analysis

Regarding structural connectivity (figure 6.3), an increased number of fibres was identified through both hemispheres.

Connectivity/ imaging metrics (figure 6.3) changes were identified for fractional anisotropy (FA), mean diffusivity (MD) and clustering coefficient (ClusC) values, in regions spatially distant to the tumour. Changes in MD values were found mostly in subcortical structures of both hemispheres (available in table E.3).

2. Gender-matched analysis

No significant additional differences regarding findings in the non gender-matched analysis were found for structural connectivity (figure 6.4).

Connectivity/ imaging metrics (figure 6.4) changes with the gender-matched group were identified exclusively in regions, of both hemispheres, spatially distant to the tumour, for increased cortical thickness (CtxT), FA, MD and ClusC values (this information, plus alterations in distant sites, are compiled in table E.4).

6.2.2.4. Patient D

[Lesion region: left Temporal lobe. Peritumoural regions: supra marginal, postcentral, precentral, superior, medial and transverse temporal gyrus, pars opercularis, putamen and insula.]

1. Non gender-matched analysis

Structural connectivity (figure 6.3) changes concerning an increased number of fibres were identified between subcortical and parietal structures from the right hemisphere.

Concerning connectivity/ imaging metrics (figure 6.3), changes were identified in peritumoural regions. Values in postcentral gyrus showed increased cortical thickness (CtxT) and decreased mean diffusivity (MD), transverse temporal gyrus and insula increased fractional anisotropy (FA), and supramarginal and medial temporal gyrus increased clustering coefficient (ClusC). Other parietal and temporal structures, from both hemispheres, also showed changes across all metrics (available in table E.3).

2. Gender-matched analysis

Regarding structural connectivity (figure 6.4) changes relatively to the full-group analysis consisted in fewer connections with increased number of fibres in the right hemisphere.

Connectivity/ imaging metrics (figure 6.4) changes with the gender-matched group were identified exclusively in regions spatially distant to the tumour, namely for the ClusC (this information, plus alterations in distant sites, are compiled in table E.4).

6.2.2.5. Patient E

[Lesion region: left temporal lobe. Peritumoural regions: insula, pars ocularis, precentral and inferior temporal gyrus.]

1. Non gender-matched analysis

Regarding structural connectivity (figure 6.3) there is an overall increase in the number of fibres in connections between right hemispheres structures.

Changes in connectivity/ imaging metrics (figure 6.3) were found mostly in left hemisphere structures. Metrics with alterations in peritumour regions included decreased FA in the precentral gyrus and increased MD in inferior temporal gyrus and pars opercularis. Other changes in increased cortical thickness (CtxT), fractional anisotropy (FA), mean diffusivity (MD), clustering coefficient (ClusC) and node degree (Deg) values, and decreased MD and FA values, were also registered in spatially distant regions to the tumour. These alterations were more predominant in parietal and temporal structures and in subcortical regions for FA and MD changes. These

last two metrics were the most affected, with the greatest number of regions with alterations (available in table E.3).

2. Gender-matched analysis

No additional differences regarding findings in the non gender-matched analysis were found for structural connectivity (figure 6.4).

Regarding connectivity/ imaging metrics (figure 6.4), additional peritumoural region insula showed increased MD. Other alterations include increased CtxT and decreased MD and Deg in regions spatially distant to the tumour, predominantly in left hemisphere structures (this information, plus alterations in distant sites, are compiled in table E.4).

6.2.2.6. Patient F

[Lesion region: right Frontal lobe. Peritumoural regions: superior frontal, precentral, posterior central, postcentral, paracentral, isthmus of the cingulate and caudal anterior cingulate gyrus, and precuneus.]

1. Non gender-matched analysis

Structural connectivity (figure 6.3) changes included an overall increased number of fibres, more evident in connections between left hemisphere structures.

Regarding connectivity/ imaging metrics (figure 6.3), changes in peritumoural regions were found. These included increased values in the paracentral gyrus for cortical thickness (CtxT) and fractional anisotropy (FA), in the postcentral gyrus for CtxT and mean diffusivity (MD), in the caudal anterior cingulate gyrus and precuneus for CtxT, in the superior frontal gyrus for FA, and precentral gyrus in MD. Other changes in regions spatially distant to the tumour were also identified for the above mentioned metrics plus decreased CtxT and increased clustering coefficient (ClusC). These corresponded mainly to temporal and parietal structures. Changes were also identified throughout both hemispheres, but were more predominant in the lesion side (available in table E.3).

2. Gender-matched analysis

Structural connectivity (figure 6.4) changes when using gender-matched data showed an increased number of fibres in more connections between left hemisphere relatively to the right hemisphere.

Changes in connectivity/ imaging metrics (figure 6.4) in peritumoural regions include additional increased FA for the precentral gyrus. Other regions spatially distant to the tumour presented alterations for increased CtxT, FA and ClusC, and decreased CtxT and values. These were distributed in parietal and temporal structures of both hemispheres (this information, plus alterations in distant sites, are compiled in table E.4).

6.2.2.7. Patient G

[Lesion region: right Temporal lobe. Peritumoural regions: supra marginal, precentral, postcentral, inferior, medial and superior temporal gryus, pars opercularis and triangularis, and banks of the temporal sulcus.]

1. Non gender-matched analysis

Regarding structural connectivity (figure 6.3), changes in increased number of fibres were identified across both hemispheres.

Concerning connectivity/ imaging metrics (figure 6.3) changes in cortical thickness (CtxT), fractional anisotropy (FA), mean diffusivity (MD) and clustering coefficient (ClusC) were identified in peritumour regions. Increased values were found in the postcentral gyrus for CtxT, in the supra marginal gyrus for CtxT and FA, in the medial and superior temporal gyrus for FA and ClusC, in the inferior temporal gyrus for FA, and in the banks of the superior temporal sulcus, pars opercularis and precentral gyrus for ClusC, and decreased MD values in the pars opercularis and precentral gyrus. Other alterations in spatially distant regions to the tumour for these metrics were also found for some left hemisphere regions and also temporal and parietal right hemisphere structures (available in table E.3).

2. Gender-matched analysis

No additional relevant differences regarding findings in the non gender-matched analysis were found for structural connectivity (figure 6.4).

Connectivity/ imaging metrics (figure 6.4) showed additional changes in the peritumour regions pars opercularis for increased FA, supra marginal gyrus for increased node degree (Deg), and pars triangularis and superior temporal gyrus for decreased MD. Previous findings of decreased FA in the supramarginal gyrus were not reported. Other alterations in regions spatially distant to the tumour were identified for all metrics in structures of both hemispheres (this information, plus alterations in distant sites, are compiled in table E.4).

6.2.2.8. Patient H

[Lesion region: right Frontal lobe. Peritumoural regions: precentral, caudal middle, rostral and superior frontal gyrus, and pars opercularis and trinagularis.]

1. Non gender-matched analysis

Regarding structural connectivity (figure 6.3) changes across both hemispheres were identified, with a greater number of connections between right hemisphere structures presenting increased number of fibres.

Connectivity/ imaging metrics (figure 6.3) showed alterations in peritumour regions regarding cortical thickness (CtxT), fractional anisotropy (FA), mean diffusivity (MD) and clustering coefficient (ClusC) values. These included increased values in the caudal middle frontal gyrus for CtxT and MD, in the middle frontal gyrus for CtxT, in the superior frontal gyrus for FA, and in the pars triangularis and precentral for ClusC. Other changes included altered metrics values in regions spatially distant to the tumour, and additional decreased CtxT and MD. These regions corresponded mainly to subcortical, parietal and frontal structures of both hemispheres (available in table E.3).

2. Gender-matched analysis

No significant additional differences regarding findings in the non gender-matched analysis were found for structural connectivity (figure 6.4).

Regarding connectivity/ imaging metrics (figure 6.4) changes in peritumoural regions included

increased Deg in the caudal middle frontal and middle frontal gyrus. Other alterations in more distant regions reflected the same behaviour as when using the full-group data (this information, plus alterations in distant sites, are compiled in table E.4).

6.2.2.9. Patient I

[Lesion region: right Temporal lobe. Peritumoural regions: supra marginal, medial, transversal and superior temporal, and postcentral gyrus, banks of the temporal sulcus and inferior parietal lobule.]

1. Non gender-matched analysis

Structural connectivity (figure 6.3) changes included an increased number of fibres in connections between parietal, temporal and frontal structures, mainly from the right hemisphere.

Connectivity/ imaging metrics (figure 6.3) changes included increased cortical thickness (CtxT), fractional anisotropy (FA) and clustering coefficient (ClusC), and decreased mean diffusivity (MD) values for peritumour regions. Increased values in the banks of the temporal sulcus for CtxT, FA and ClusC, in the inferior parietal lobe for CtxT, in medial temporal gyrus for FA and ClusC, and in the superior temporal gyrus for FA were identified, and decreased values in the postcentral gyrus and insula were found for MD. Other regions with changes spatially distant to the tumour comprised subcortical, frontal and parietal structures (available in table E.3).

2. Gender-matched analysis

No significant additional differences regarding findings in the non gender-matched analysis were found for structural connectivity (figure 6.4).

Changes in connectivity/ imaging metrics (figure 6.4) in peritumoural regions included not observing reduced MD values in the postcentral gyrus. Other alterations with significant changes included regions spatially distant to the tumour as reported before (this information, plus alterations in distant sites, are compiled in table E.4).

6.3. Overall changes

In all cases increased FET uptake was observed in the area of suspected tumour location in MRI, which confirms the presence of tumour tissue [23].

All studied patients had lesions in the motor and pre-motor regions.

The intrahemispheric analysis results showed isolated increases of FA values in peritumoural regions, identified in patients A (superior parietal lobule, precentral gyrus), B (pars opercularis), D (insula, transverse temporal gyrus), F (superior parietal lobule, precentral gyrus), G (supramarginal and medial temporal gyrus, superior parietal lobule, pars opercularis), H (pars opercularis) and I (superior temporal, supramarginal and medial temporal gyrus, banks of the superior temporal sulcus).

Regarding the whole-brain assessment results, increased FA values were found in patients A (precentral gyrus), B (insula, pars opercularis), D (insula, transverse temporal gyrus), F (superior frontal and paracentral gyrus), G (supramarginal, medial and inferior temporal gyrus), H

(superior frontal gyrus), I (superior and medial temporal gyrus, banks of the temporal sulcus). Decreased values of this metric were found in patient E (precentral gyrus).

These results may mirror increased fibre density as a result of tumour mass effect. On the other hand, reduction of this same metric may be explained by axonal destruction, and consequently loss of directionalty. Possible causes for this event could be the pathways destruction, which can be explained in turn by the tumour presence and its infiltrative profile as well as, by oedema presence in its surroundings, like the event found in patient E (precentral gyrus) [67, 77]. Findings concerning the correlation between FA values and fibre density are documented by Robert et al., 2005 [78] who has correlated this metric with the fibre density (increased FA relates to higher fibre density whereas decreased values relates to lower fibre density measures). This effect was observed in patients E (inferior temporal gyrus), F (posterior cingulate and superior frontal gyrus), G (supramarginal gyrus, pars opercularis), H (caudal middle frontal gyrus, pars opercularis), and I (supramarginal and middle temporal gyrus, banks of the temporal sulcus), accordingly.

From the intrahemispheric analysis an isolated MD value increase was observed in patients E (pars orbitalis, inferior temporal gyrus), F (posterior cingulate gyrus, caudal anterior cingulate gyrus) and H (caudal and rostral middle frontal gyrus). One isolated reduced value was identified in patient E (precentral gyrus).

Regarding the whole-brain connectivity assessment analysis, increased MD values were registered in patients B (postcentral gyrus), E (insula, pars orbitalis inferior temporal gyrus) and H (caudal middle frontal gyrus), and decreased values in patients A (precentral gyrus), D (precentral and postcentral gyrus, pars opercularis), F (precentral and postcentral gyrus), G (precentral gyrus, pars opercularis) and I (postcentral gyrus).

In terms of MD results, the presence of oedema surrounding the tumour region may explain an isolated increased value of this metric. On the other hand, isolated MD decreased values may be explained by a larger presence of tumoural cells, resultant from tumour growth and infiltration characteristic from glioblastomas [79].

Findings regarding FA and MD in the whole-brain analysis approach showed some differences presumably due to the elimination of the hemispheric symmetry assumption needed in order to apply the intrahemispheric analysis.

ClusC alterations observed in the intrahemispheric analysis included augmented values in patients A (supra marginal gyrus), C (precentral gyrus), E (insula) and G (medial temporal gyrus). Reduced values of this metric were observed in patients B (postcentral and superior temporal gyrus), D (transverse and superior temporal gyrus) and H (rostral and caudate middle frontal gyrus).

Registered alterations in the whole-brain assessment include occurrences with increased values in patients B (transversal temporal gyrus), D (supra marginal ad medial temporal gyrus), G (medial temporal, superior temporal and precentral gyrus, banks of the temporal sulcus, pars opercularis), H (pars triangularis, precentral gyrus) and I (banks of the temporal sulcus, medial temporal gyrus) and a single reduced value in patient A (precentral gyrus).

ClusC measures a level of segregation, structural at a first level. Based on the characterisation done previously it measures functional segregation at a second level. Given the nature of brain tumours, we could expect for alterations in this metric assuming connectivity patterns reor-

ganisation, due to the induced tissue destruction [62]. Findings in the first approach suggest a reorganisation of structural connections that more peritumoural regions are connected with their neighbours. The same behaviour is observed when analysing results obtained from the whole-brain assessment analysis, where we can refer to patient G, which presents a higher number of regions with high ClusC. However, even with a single node connected to more neighbours, this does not imply that there is an increased registered value of Deg for this same regions, as presented below.

Concerning Deg findings, with the intrahemispheric analysis, increased values were found in patients A (precentral and postcentral gyrus, superior and inferior parietal lobule), B (superior temporal and postcentral gyrus, superior parietal lobule), D (pars opercularis), E (inferior temporal gyrus), F (superior frontal and paracentral gyrus) and H (superior frontal, caudal and rostral middle frontal gyrus, pars opercularis). Decreased values of this metric were observed in patients E and I (both in insula).

Regarding the whole-brain assessment analysis, increased values were only found in patient A (inferior parietal lobule) and D (pars opercularis).

With respect to Deg results we would expect for lower degree in peritumoural regions, due to regional alterations induced by the tumour, including accumulation of necrotic tissue, characteristic of glioblastoma [21, 62]. This connectivity measure value is related to the interaction of a node with the remaining nodes in the network, either structurally or functionally. In this specific case we were interested in structural connectivity, since Deg values corresponded to a DTI derived metric. However, findings from the intrahemispheric differences assessment analysis shown increased Deg in various peritumoural regions for 6 patients. On the other hand, whole-brain assessment results have only shown 2 patients with increased Deg around the tumour site, and no other patient presented altered values for either local or more distant structures.

CtxT results for the intrahemisperic analysis included increased values in patients A (precentral and postcentral gyrus), F (superior frontal, pparacentral, posterior cingulate, isthmus of the cingulate and caudal anterior cingulate gyrus, precuneus), G (supra marginal, postecentral and inferior temporal gyrus), H (superior frontal, caudal and rostral middle frontal gyrus, pars opercularis) and I (banks of the temporal sulcus, transverse temporal gyrus). Reduced values were observed in patients C (precentral gyrus), D (superior temporal gyrus), E (inferior temporal gyrus).

Concerning CtxT findings whith the whole-brain assessment analysis, only increased values, in peritumoural sites, were registered, in patients A (precentral and postcentral gyrus, superior temporal lobe), D (postcentral gyrus), F (paracentral, postcentral and caudate anterior cingulate gyrus, precuneus), G (postcentral and supra marginal gyrus), H (caudal middle frontal and middle frontal gyrus) and I (bank of the temporal sulcus, inferior parietal lobe).

In terms of findings regarding CtxT these could indicate changes at the cortex level, such as a higher number of axons' cellular bodies in a certain site. These measures could be dependent on tumour location, and influence the observed values by having patients with tumours nearer the cortex presenting higher CtxT values (some of it could just be necrotic or tumoural tissue, identified as grey matter), and ones located in the white matter presenting lower CtxT values, as a result of the cortex compression exerted by the tumour.

In regards to results when using the gender-matched group, it was expected to see some differences of affected regions. This hypothesis was supported by evidence of different connectivity

patterns present in the female (analytical and intuitive processing) and male (perception and coordinated actions) and also the overall brain size, since men tend to have larger crania, and higher percentage of white matter, whereas females tend to present higher concentrations of grey matter [74, 80]. Reported findings reflected some changes in additional regions for the studied connectivity/ imaging metrics in both approaches.

Overall these findings also suggest that, in this study, right-sided tumours have more generalised effects when compared to the left-sided tumours, since more differences were found at a higher threshold in both approaches for right-sided lesions. Findings of this work also imply the tumour presence influence in whole-brain connectivity, with alteration of different connectivity measures throughout both hemispheres. Possible causes of this effect are the above mentioned fibre packing due to the tumour mass effect and structural re-organization due to the loss of white matter integrity in the adjacent tumour regions [21]. Additionally, changes in axons membranes resultant from the tumour presence in local regions may occur. These could result from increased myelin production by adjacent cells to the tumour region, due to its local influence in cellular processes [81]. With excessive myelin production we could expect to have thicker myelin coats in the axons which would have an impact on the water molecules transport (ie. more directionality), hence higher FA and lower MD, ultimately strengthening local connections.

Final Remarks

From the intrahemispheric analysis, patients C and D presented the least significant differences. On the other hand, patient E and all with right-sided lesions presented differences in connectivity/imaging metrics at 2thres, suggesting larger difference in brain reorganization, when comparing to the healthy controls group data. With regards to the whole-brain assessment results, patient C presented the least significant changes, and the same patients mentioned above had higher number of significant changes. However, in this approach, changes at 3 standard deviations regarding structural connectivity showed exclusively increased number of fibres in various connections, in relation to the control group. Overall, regarding all cases from both analysis approaches, most significant changes refer to the number of fibres, suggesting that the presence of tumour lesions influence whole-brain connectivity. These results could be explained by the fibre packing due to the tumour mass effect, and to structural re-organisation due to integrity loss in white matter, in adjacent tumour sites. Additionally, changes at a molecular level could be in place, since tumoural cells have the ability of influence local cellular processes, which could relate to production of larger myelin quantities. In turn, this could relate to thicker myelin coats in axon membranes, ultimately strengthening local connections (higher FA and lower MD measures).

Ultimately, this work presents a novel approach for whole-brain connectivity assessment of brain tumour patients using MIBCA to integrate anatomical and diffusion MRI and metabolic PET data. Findings suggest that tumours cause connectivity changes not only locally but also in more distant brain regions. However, the small number of control subjects used in this study (total number of subjects: $N = 22$; number of subjects in the gender-based groups: $N = 11$) and the small number of patients included in this pilot study ($N = 9$), does not allow drawing definitive conclusions regarding this aspect. Further confirmation of the hypothesis in a larger study is required.

Future work should look into further detail in brain segmentation when in presence of tumours. Improving parcellation, erroneous segmentation and, thus, wrong assignment of tumour to a distinct region could be avoided. Obviously, misassignment can be misleading when drawing conclusions regarding tumour-derived changes in connectivity. In addition, DKI tractography should be included, in order to improve obtained metrics from diffusion data.

Since tractography based on the kurtosis tensor provides richer results than DTI-based tractography [42], we expect the characterisation of brain connectivity to improve with this approach. Regarding brain tumours, one limitation is the oedema presence for fibre tracking. Since the oedematous region has lower FA than healthy tissue, due to its increased water content, many fibres are not accounted for tractography once entering the tumour region.

Ultimately, the goal of this approach was to investigate if and how connectivity studies can help in presurgical planning. For instance, the study of specific brain networks would be able to provide information on the best anatomical approach to the tumour and influence surgical decision-making, with regard to the prevention of sequelae. Another possibility could be the

characterisation of tumour regarding their connectivity profile, using it as a marker to, for instance, classify the type of glioma in an early stage of development.

In appendix F a list of communications and awards resultant from the work developed through the thesis is presented.

Bibliography

[1] "Brain Tumor." National Cancer Institute, [Online], `http://www.cancer.gov/cancertopics/types/brain` (Accessed 06-12-2015).

[2] C. Alafaci, F. Granata, M. Cutugno, M. Caffo, G. Caruso, and F. Maria, "Modern Neuroimaging Techniques in The Diagnosis of Brain Tumours," in *Clinical Management and Evolving Novel Therapeutic Strategies for Patients with Brain Tumors* (T. Lichtor, ed.), InTech, Apr. 2013.

[3] S. Jbabdi and H. Johansen-Berg, "Tractography: Where Do We Go from Here?," *Brain Connectivity*, vol. 1, pp. 169–183, Sept. 2011.

[4] M. Rowe, H. G. Zhang, N. Oxtoby, and D. C. Alexander, "Beyond Crossing Fibers: Tractography Exploiting Sub-voxel Fibre Dispersion and Neighbourhood Structure," in *Information Processing in Medical Imaging* (J. C. Gee, S. Joshi, K. M. Pohl, W. M. Wells, and L. Zöllei, eds.), no. 7917 in Lecture Notes in Computer Science, pp. 402–413, Springer Berlin Heidelberg, Jan. 2013.

[5] J.-W. Jeong, E. Asano, F.-C. Yeh, D. C. Chugani, and H. T. Chugani, "Independent component analysis tractography combined with a ball–stick model to isolate intravoxel crossing fibers of the corticospinal tracts in clinical diffusion MRI," *Magnetic Resonance in Medicine*, vol. 70, pp. 441–453, Aug. 2013.

[6] F. Bartolomei, I. Bosma, M. Klein, J. C. Baayen, J. C. Reijneveld, T. J. Postma, J. J. Heimans, B. W. van Dijk, J. C. de Munck, A. de Jongh, K. S. Cover, and C. J. Stam, "How do brain tumors alter functional connectivity? A magnetoencephalography study," *Annals of Neurology*, vol. 59, pp. 128–138, Jan. 2006.

[7] C. Briganti, C. Sestieri, P. A. Mattei, R. Esposito, R. J. Galzio, A. Tartaro, G. L. Romani, and M. Caulo, "Reorganization of Functional Connectivity of the Language Network in Patients with Brain Gliomas," *American Journal of Neuroradiology*, vol. 33, pp. 1983–1990, Nov. 2012.

[8] J. Martino, S. M. Honma, A. M. Findlay, A. G. Guggisberg, J. P. Owen, H. E. Kirsch, M. S. Berger, and S. S. Nagarajan, "Resting functional connectivity in patients with brain tumors in eloquent areas," *Annals of Neurology*, vol. 69, pp. 521–532, Mar. 2011.

[9] A. G. Guggisberg, S. M. Honma, A. M. Findlay, S. S. Dalal, H. E. Kirsch, M. S. Berger, and S. S. Nagarajan, "Mapping Functional Connectivity in Patients with Brain Lesions," *Annals of Neurology*, vol. 63, pp. 193–203, Feb. 2008.

[10] J. Shao, N. Myers, Q. Yang, J. Feng, C. Plant, C. Böhm, H. Förstl, A. Kurz, C. Zimmer, C. Meng, V. Riedl, A. Wohlschläger, and C. Sorg, "Prediction of Alzheimer's disease using

individual structural connectivity networks," *Neurobiology of Aging*, vol. 33, pp. 2756–2765, Dec. 2012.

[11] A. Santos Ribeiro, L. M. Lacerda, and H. A. Ferreira, "Multimodal Imaging Brain Connectivity Analysis toolbox (MIBCA)," *PeerJ*, p. 3:e1078, 2014.

[12] C. L. VanPutte and R. R. Seeley, *Seeley's anatomy & physiology.* New York, NY: McGraw-Hill, 10th ed., 2014.

[13] J. A. E. Pina, *Anatomia Humana da Relação.* Lisboa: Lidel, 4th ed., 2009.

[14] R. S. Snell, *Clinical Neuroanatomy.* Philadelphia: Lippincott Williams & Wilkins, 7th ed., 2010.

[15] F. H. Netter, *Atlas of Human Anatomy.* Philadelphia: Elsevier Health Sciences, 5th ed., May 2010.

[16] L. M. DeAngelis, "Brain Tumors," *New England Journal of Medicine*, vol. 344, pp. 114–123, Jan. 2001.

[17] D. N. Louis, H. Ohgaki, O. D. Wiestler, and W. K. Cavenee, *WHO Classification of Tumours*, vol. 1 of *IARC WHO Classification of Tumors.* WHO, 4th ed., 2007.

[18] Andrej Pala, Georg Karpel-Massler, Christian Rainer Wirtz, and Marc-Eric Halatsch, "Epithelial to Mesenchymal Transition and Progression of Glioblastoma," in *Clinical Management and Evolving Novel Therapeutic Strategies for Patients with Brain Tumors*, InTech, Apr. 2013.

[19] M. J. McGirt, D. Mukherjee, K. L. Chaichana, K. D. Than, J. D. Weingart, and A. Quinones-Hinojosa, "Association of surgically acquired motor and language deficits on overall survival after resection of glioblastoma multiforme," *Neurosurgery*, vol. 65, no. 3, 2009.

[20] C. Adamson, O. O. Kanu, A. I. Mehta, C. Di, N. Lin, A. K. Mattox, and D. D. Bigner, "Glioblastoma multiforme: a review of where we have been and where we are going," *Expert Opinion on Investigational Drugs*, vol. 18, pp. 1061–1083, Aug. 2009.

[21] H. B. Newton and F. A. Jolesz, eds., *Handbook of Neuro-Oncology Neuroimaging.* Amsterdam: Academic Press, Nov. 2007.

[22] J. Rees and P. Y. Wen, *Neuro-Oncology.* Blue Books of Practical Neurology, Philadelphia: Saunders/Elsevier, 2010.

[23] N. Galldiks and K. J. Langen, "Applications of PET imaging of neurological tumors with radiolabeled amino acids," *The Quarterly Journal of Nuclear Medicine and Molecular Imaging*, vol. 59, pp. 70–82, Mar. 2015.

[24] R. W. Brown, Y.-C. N. Cheng, E. M. Haacke, M. R. Thompson, and R. Venkatesan, *Magnetic Resonance Imaging: Physical Properties and Sequence Design.* John Wiley & Sons, Apr. 2014.

[25] M. A. Brown and R. C. Semelka, *MRI: basic principles and applications*. Hoboken, N.J.: Wiley-Liss, 2003.

[26] D. W. McRobbie, *MRI from picture to proton*. Cambridge, UK; New York: Cambridge University Press, 2006.

[27] V. Kuperman, *Magnetic Resonance Imaging: Physical Principles and Applications*. Academic Press, Mar. 2000.

[28] H. S. Chrysikopoulos, *Clinical MR Imaging and Physics: A Tutorial*. Springer Science & Business Media, Nov. 2008.

[29] M. A. Bernstein, K. F. King, and X. J. Zhou, *Handbook of MRI pulse sequences*. Amsterdam; Boston: Academic Press, 2004.

[30] R. Bitar, G. Leung, R. Perng, S. Tadros, A. R. Moody, J. Sarrazin, C. McGregor, M. Christakis, S. Symons, A. Nelson, and T. P. Roberts, "MR Pulse Sequences: What Every Radiologist Wants to Know but Is Afraid to Ask," *RadioGraphics*, vol. 26, pp. 513–537, Mar. 2006.

[31] "Pulse sequence timing diagram." [Online], `http://www.mr-tip.com/serv1.php?type=db1&dbs=Pulse%20Sequence%20Timing%20Diagram`, (Accessed 20-07-2015).

[32] J. P. Mugler and J. R. Brookeman, "Three-dimensional magnetization-prepared rapid gradient-echo imaging (3d MP RAGE)," *Magnetic Resonance in Medicine*, vol. 15, pp. 152–157, July 1990.

[33] J. Wang, L. He, H. Zheng, and Z.-L. Lu, "Optimizing the Magnetization-Prepared Rapid Gradient-Echo (MP-RAGE) Sequence," *PLoS ONE*, vol. 9, p. e96899, May 2014.

[34] "3D MPRAGE sequence diagram." [Online], `http://www.simplyphysics.com/MARS/data/level_3/3DMPRAGE-GIF.htm`, (Accessed 20-07-2015).

[35] E. O. Stejskal and J. E. Tanner, "Spin Diffusion Measurements: Spin Echoes in the Presence of a Time-Dependent Field Gradient," *The Journal of Chemical Physics*, vol. 42, pp. 288–292, Jan. 1965.

[36] R. Plonsey and R. C. Barr, *Bioelectricity: A Quantitative Approach*. Springer Science & Business Media, Jan. 2000.

[37] H. Johansen-Berg and T. E. J. Behrens, *Diffusion MRI: From Quantitative Measurement to In vivo Neuroanatomy*. Academic Press, Nov. 2013.

[38] D. Le Bihan, J.-F. Mangin, C. Poupon, C. A. Clark, S. Pappata, N. Molko, and H. Chabriat, "Diffusion tensor imaging: concepts and applications," *Journal of Magnetic Resonance Imaging*, vol. 13, no. 4, pp. 534–546, 2001.

[39] P. Mukherjee, J. I. Berman, S. W. Chung, C. P. Hess, and R. G. Henry, "Diffusion Tensor MR Imaging and Fiber Tractography: Theoretic Underpinnings," *American Journal of Neuroradiology*, vol. 29, pp. 632–641, Apr. 2008.

[40] R. Liang, X. Wang, M. Li, Y. Yang, J. Luo, Q. Mao, and Y. Liu, "Potential role of fractional anisotropy derived from diffusion tensor imaging in differentiating high-grade gliomas from low-grade gliomas: a meta-analysis," *International Journal of Clinical and Experimental Medicine*, vol. 7, pp. 3647–3653, Oct. 2014.

[41] E. Fieremans, J. H. Jensen, and J. A. Helpern, "White Matter Characterization with Diffusional Kurtosis Imaging," *NeuroImage*, vol. 58, pp. 177–188, Sept. 2011.

[42] R. Neto Henriques, M. M. Correia, R. G. Nunes, and H. A. Ferreira, "Exploring the 3d geometry of the diffusion kurtosis tensor—Impact on the development of robust tractography procedures and novel biomarkers," *NeuroImage*, vol. 111, pp. 85–99, May 2015.

[43] J. T. Bushberg and J. M. Boone, *The Essential Physics of Medical Imaging*. Philadelphia: Lippincott Williams & Wilkins, Dec. 2011.

[44] I. Neuner, J. B. Kaffanke, K.-J. Langen, E. R. Kops, L. Tellmann, G. Stoffels, C. Weirich, C. Filss, J. Scheins, H. Herzog, and N. J. Shah, "Multimodal imaging utilising integrated MR-PET for human brain tumour assessment," *European Radiology*, vol. 22, pp. 2568–2580, Dec. 2012.

[45] W. E. Brant and C. A. Helms, *Fundamentals of Diagnostic Radiology*. Philadelphia: Lippincott Williams & Wilkins, Mar. 2012.

[46] "Lecture Notes | Introduction to Ionizing Radiation | Nuclear Science and Engineering | MIT OpenCourseWare." [Online], `http://ocw.mit.edu/courses/nuclear-engineering/` (Accessed in 10-12-2014).

[47] "Radionuclide half-life measurments." NIST, [Online], `http://www.nist.gov/pml/data/halflife-html.cfm` (Accessed 06-08-2015).

[48] H. J. Wester, M. Herz, W. Weber, P. Heiss, R. Senekowitsch-Schmidtke, M. Schwaiger, and G. Stöcklin, "Synthesis and Radiopharmacology of O-(2-[18F]fluoroethyl)-L-Tyrosine for Tumor Imaging," *Journal of Nuclear Medicine*, vol. 40, pp. 205–212, Jan. 1999.

[49] K.-J. Langen, K. Hamacher, M. Weckesser, F. Floeth, G. Stoffels, D. Bauer, H. H. Coenen, and D. Pauleit, "O-(2-[18F]fluoroethyl)-l-tyrosine: uptake mechanisms and clinical applications," *Nuclear Medicine and Biology*, vol. 33, pp. 287–294, Apr. 2006.

[50] D. Pauleit, F. Floeth, K. Hamacher, M. J. Riemenschneider, G. Reifenberger, H.-W. Müller, K. Zilles, H. H. Coenen, and K.-J. Langen, "O-(2-[18F]fluoroethyl)-l-tyrosine PET combined with MRI improves the diagnostic assessment of cerebral gliomas," *Brain*, vol. 128, pp. 678–687, Mar. 2005.

[51] F. W. Floeth, D. Pauleit, M. Sabel, G. Reifenberger, G. Stoffels, W. Stummer, F. Rommel, K. Hamacher, and K.-J. Langen, "18F-FET PET differentiation of ring-enhancing brain lesions," *Journal of Nuclear Medicine*, vol. 47, no. 5, pp. 776–782, 2006.

[52] Y. He and A. Evans, "Graph theoretical modeling of brain connectivity," *Current Opinion in Neurology*, pp. 341–350, June 2010.

[53] M. Guye, G. Bettus, F. Bartolomei, and P. J. Cozzone, "Graph theoretical analysis of

structural and functional connectivity MRI in normal and pathological brain networks," *Magnetic Resonance Materials in Physics, Biology and Medicine*, vol. 23, pp. 409–421, Dec. 2010.

[54] O. Sporns, "From simple graphs to the connectome: Networks in neuroimaging," *NeuroImage*, vol. 62, pp. 881–886, Aug. 2012.

[55] G. Gong, Y. He, L. Concha, C. Lebel, D. W. Gross, A. C. Evans, and C. Beaulieu, "Mapping Anatomical Connectivity Patterns of Human Cerebral Cortex Using In Vivo Diffusion Tensor Imaging Tractography," *Cerebral Cortex*, vol. 19, pp. 524–536, Mar. 2009.

[56] M. Kaiser, "A tutorial in connectome analysis: topological and spatial features of brain networks," *NeuroImage*, vol. 57, no. 3, pp. 892–907, 2011.

[57] J. P. Lerch, K. Worsley, W. P. Shaw, D. K. Greenstein, R. K. Lenroot, J. Giedd, and A. C. Evans, "Mapping anatomical correlations across cerebral cortex (MACACC) using cortical thickness from MRI," *NeuroImage*, vol. 31, pp. 993–1003, July 2006.

[58] "Human Connectome Project | Mapping the human brain connectivity." Laboratory of Neuro Imaging and Martinos Center for Biomedical Imaging at Massachusetts General Hospital, [Online], `http://www.humanconnectomeproject.org/` (Accessed 08-12-2014).

[59] R. E. Passingham, "What we can and cannot tell about the wiring of the human brain," *NeuroImage*, vol. 80, pp. 14–17, Oct. 2013.

[60] Z. J. Chen, Y. He, P. Rosa-Neto, J. Germann, and A. C. Evans, "Revealing Modular Architecture of Human Brain Structural Networks by Using Cortical Thickness from MRI," *Cerebral Cortex*, vol. 18, pp. 2374–2381, Oct. 2008.

[61] K. Friston, "Causal Modelling and Brain Connectivity in Functional Magnetic Resonance Imaging," *PLoS Biol*, vol. 7, p. e1000033, Feb. 2009.

[62] M. Rubinov and O. Sporns, "Complex network measures of brain connectivity: Uses and interpretations," *NeuroImage*, vol. 52, pp. 1059–1069, Sept. 2010.

[63] Y. He, Z. J. Chen, and A. C. Evans, "Small-World Anatomical Networks in the Human Brain Revealed by Cortical Thickness from MRI," *Cerebral Cortex*, vol. 17, pp. 2407–2419, Oct. 2007.

[64] V. Neuschmelting, C. Weiss Lucas, G. Stoffels, A.-M. Oros-Peusquens, H. Lockau, N. J. Shah, K.-J. Langen, R. Goldbrunner, and C. Grefkes, "Multimodal Imaging in Malignant Brain Tumors: Enhancing the Preoperative Risk Evaluation for Motor Deficits with a Combined Hybrid MRI-PET and Navigated Transcranial Magnetic Stimulation Approach," *American Journal of Neuroradiology*, Oct. 2015.

[65] S. Lu, D. Ahn, G. Johnson, M. Law, D. Zagzag, and R. I. Grossman, "Diffusion-Tensor MR Imaging of Intracranial Neoplasia and Associated Peritumoral Edema: Introduction of the Tumor Infiltration Index1," *Radiology*, vol. 232, pp. 221–228, July 2004.

[66] T. J. D. Byrnes, T. R. Barrick, B. A. Bell, and C. A. Clark, "Diffusion tensor imaging

discriminates between glioblastoma and cerebral metastases in vivo," *NMR in Biomedicine*, vol. 24, pp. 54–60, Jan. 2011.

[67] W. Wang, C. Steward, and P. Desmond, "Diffusion Tensor Imaging in Glioblastoma Multiforme and Brain Metastases: The Role of p, q, L, and Fractional Anisotropy," *American Journal of Neuroradiology*, vol. 30, pp. 203–208, Aug. 2008.

[68] H. Herzog, K.-J. Langen, C. Weirich, E. Rota Kops, J. Kaffanke, L. Tellmann, J. Scheins, I. Neuner, G. Stoffels, K. Fischer, L. Caldeira, H. H. Coenen, and N. J. Shah, "High resolution BrainPET combined with simultaneous MRI," *Nuklearmedizin. Nuclear Medicine*, vol. 50, no. 2, pp. 74–82, 2011.

[69] K. Hamacher and H. H. Coenen, "Efficient routine production of the 18F-labelled amino acid O-(2-[18F]fluoroethyl)-l-tyrosine," *Applied Radiation and Isotopes*, vol. 57, pp. 853–856, Dec. 2002.

[70] B. Fischl, "FreeSurfer," *NeuroImage*, vol. 62, pp. 774–781, Aug. 2012.

[71] B. Fischl, D. H. Salat, E. Busa, M. Albert, M. Dieterich, C. Haselgrove, A. Van Der Kouwe, R. Killiany, D. Kennedy, S. Klaveness, and others, "Whole brain segmentation: automated labeling of neuroanatomical structures in the human brain," *Neuron*, vol. 33, no. 3, pp. 341–355, 2002.

[72] R. S. Desikan, F. Ségonne, B. Fischl, B. T. Quinn, B. C. Dickerson, D. Blacker, R. L. Buckner, A. M. Dale, R. P. Maguire, B. T. Hyman, M. S. Albert, and R. J. Killiany, "An automated labeling system for subdividing the human cerebral cortex on MRI scans into gyral based regions of interest," *NeuroImage*, vol. 31, pp. 968–980, July 2006.

[73] J.-L. Hsu, A. Leemans, C.-H. Bai, C.-H. Lee, Y.-F. Tsai, H.-C. Chiu, and W.-H. Chen, "Gender differences and age-related white matter changes of the human brain: A diffusion tensor imaging study," *NeuroImage*, vol. 39, pp. 566–577, Jan. 2008.

[74] C. D. Good, I. Johnsrude, J. Ashburner, R. N. Henson, K. J. Friston, and R. S. Frackowiak, "Cerebral asymmetry and the effects of sex and handedness on brain structure: A voxel-based morphometric analysis of 465 normal adult human brains," *NeuroImage*, vol. 14, pp. 685–700, Sept. 2001.

[75] R. A. Kanaan, C. Chaddock, M. Allin, M. M. Picchioni, E. Daly, S. S. Shergill, and P. K. McGuire, "Gender Influence on White Matter Microstructure: A Tract-Based Spatial Statistics Analysis," *PLoS ONE*, vol. 9, p. e91109, Mar. 2014.

[76] A. Pfefferbaum, E. Adalsteinsson, and E. V. Sullivan, "Frontal circuitry degradation marks healthy adult aging: Evidence from diffusion tensor imaging," *NeuroImage*, vol. 26, pp. 891–899, July 2005.

[77] A. Stadlbauer, C. Nimsky, S. Gruber, E. Moser, T. Hammen, T. Engelhorn, M. Buchfelder, and O. Ganslandt, "Changes in fiber integrity, diffusivity, and metabolism of the pyramidal tract adjacent to gliomas: a quantitative diffusion tensor fiber tracking and MR spectroscopic imaging study," *American Journal of Neuroradiology*, vol. 28, no. 3, pp. 462–469, 2007.

[78] T. P. Roberts, F. Liu, A. Kassner, S. Mori, and A. Guha, "Fiber density index correlates with reduced fractional anisotropy in white matter of patients with glioblastoma," *American Journal of Neuroradiology*, vol. 26, no. 9, pp. 2183–2186, 2005.

[79] A. L. Alexander, J. E. Lee, M. Lazar, and A. S. Field, "Diffusion Tensor Imaging of the Brain," *NeuroTherapeutics*, vol. 4, no. 3, pp. 316–329, 2007.

[80] M. Ingalhalikar, A. Smith, D. Parker, T. D. Satterthwaite, M. A. Elliott, K. Ruparel, H. Hakonarson, R. E. Gur, R. C. Gur, and R. Verma, "Sex differences in the structural connectome of the human brain," *Proceedings of the National Academy of Sciences*, vol. 111, pp. 823–828, Jan. 2014.

[81] R. Bonavia, M.-d.-M. Inda, W. K. Cavenee, and F. B. Furnari, "Heterogeneity Maintenance in Glioblastoma: A Social Network," *Cancer Research*, vol. 71, pp. 4055–4060, June 2011.

Appendices

A. Additional results - control variability by gender

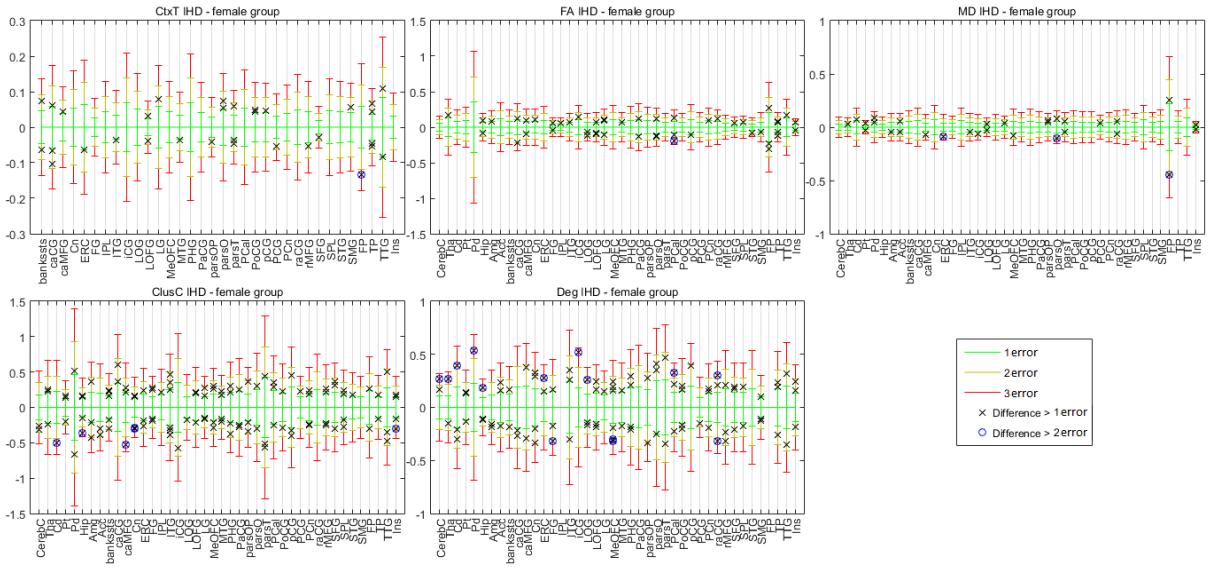

Figure A.1.: The asymmetry index (AI) calculated from the mean value for each metric, by structure, of the female control group ($N = 11$), was subtracted from each corresponding individual subject AI value. Then, the resultant value was plotted against intervals comprised the calculated error in the form $[-n \times error; n \times error]$, with $n = 1, 2, 3$.
Black and blue markers represent differences larger than 1 and 2 times the calculated error, respectively. Green, yellow and red error bars match the usage of 1, 2 and 3 times the calculated error.
Cortical thickness (CtxT) values are represented in mm and mean diffusivity (MD) values in mm^2/s.

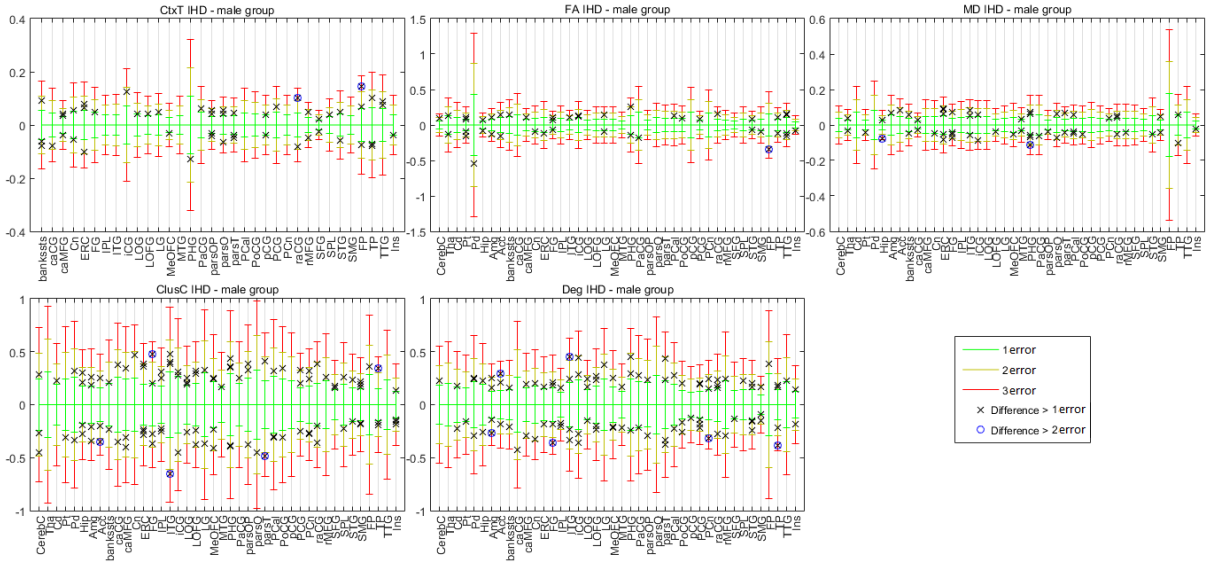

Figure A.2.: The asymmetry index (AI) calculated from the mean value for each metric, by structure, of the male control group ($N = 11$), was subtracted from each correspondent individual subject AI value. Then, the resultant value was plotted against intervals which comprised the calculated error in the form $[-n \times error; n \times error]$, with $n = 1, 2, 3$. Black and blue markers represent differences larger than 1 and 2 times the calculated error, respectively. Green, yellow and red error bars match the usage of 1, 2 and 3 times the calculated error.

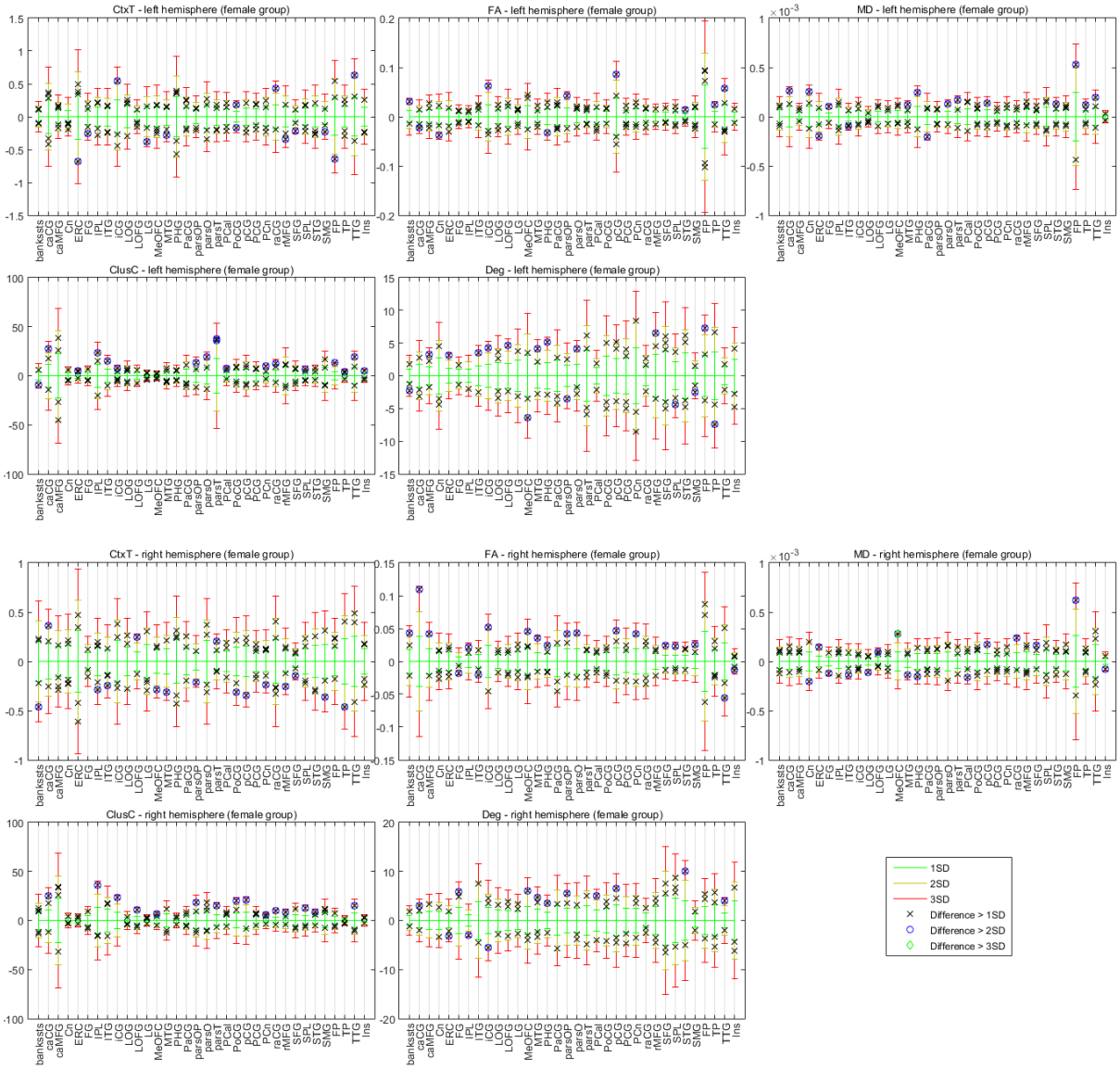

Figure A.3.: The mean value for each metric, by structure, of the female control group ($N = 11$), was subtracted by each correspondent individual subject value. Then, the resultant value was plotted against intervals which comprised the structures' standard deviation (SD) in the form $[-n \times SD; n \times SD]$, with $n = 1, 2, 3$.
Black and blue markers represent differences larger than 1 and 2 times the SD, respectively. Green, yellow and red error bars match the usage of 1, 2 and 3 times the SD. In the top two rows we have the representation of left-hand structures and in the bottom two, right-hand structures.

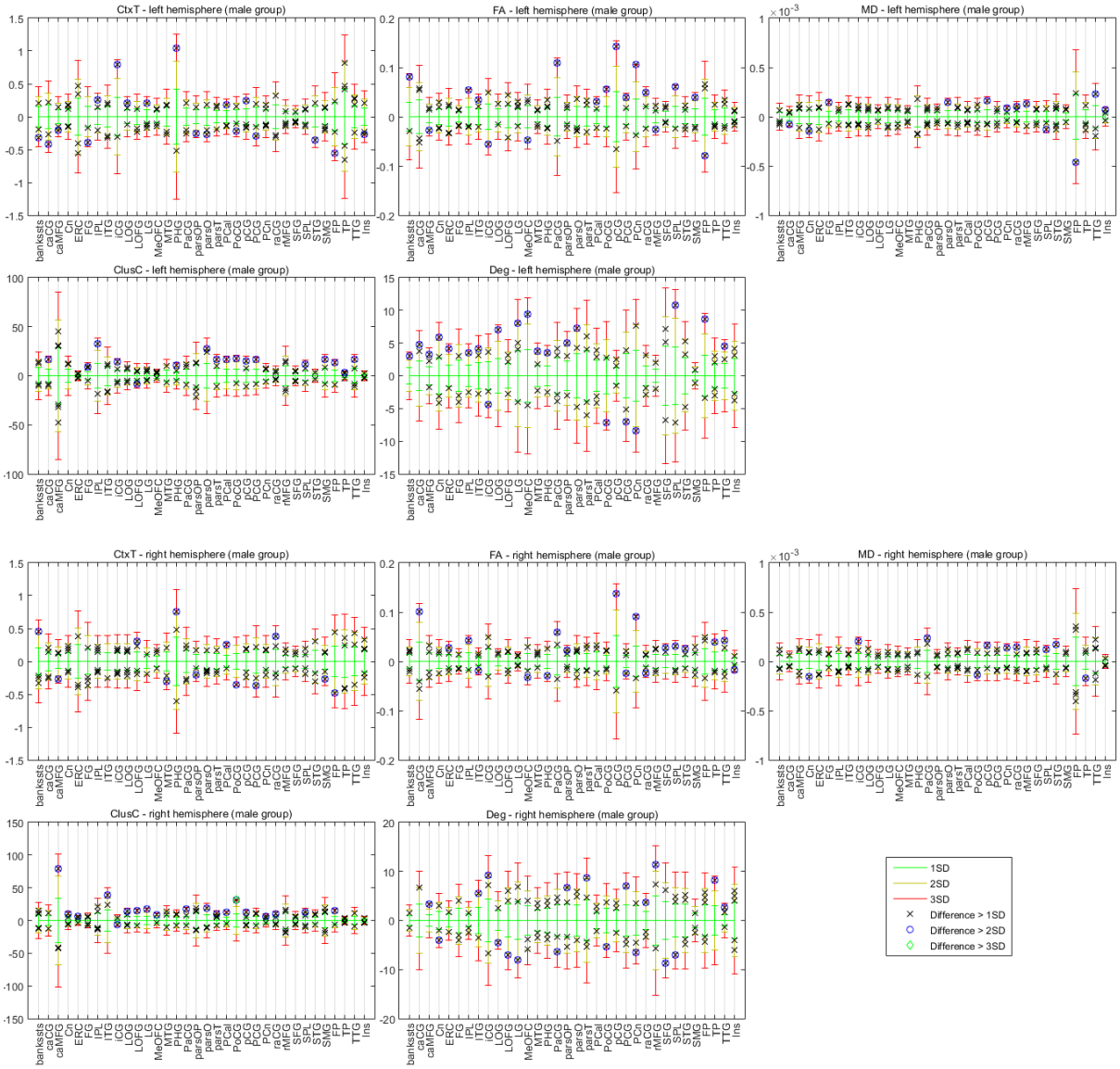

Figure A.4.: The mean value for each metric, by structure, of the male control group ($N = 11$), was subtracted by each correspondent individual subject value. Then, the resultant value was plotted against intervals which comprised the structures' standard deviation (SD) in the form $[-n \times SD; n \times SD]$, with $n = 1, 2, 3$.
Black and blue markers represent differences larger than 1 and 2 times the SD, respectively. Green, yellow and red error bars match the usage of 1, 2 and 3 times the SD. In the top two rows we have the representation of left-hand structures and in the bottom two, right-hand structures.

B. FreeSurfer labeling and atlases

Table B.1.: List of cortical and subcortical structures, according the atlases from figures B.1 and B.2.

Subcortical structures

CerebC	cerebellum	Pd	pallidum
Tha	thalamus	Hip	hippocampus
Cd	caudate	Am	amygdala
Pt	putamen	Acc	accumbens

Cortical structures

bankssts	banks of the temporal sulcus	parsO	pars orbitalis
caCG	caudal anterior cingulate	parsT	pars triangularis
cMFG	caudal middle frontal	Pcal	pericalcarine
Cn	cuneus	PoCG	postcentral
ERC	entorhinal	pCG	posterior cingulate
FG	fusiform	PCG	precentral
IPL	inferior parietal	PCn	precuneus
ITG	inferior temporal	raCG	rostral anterior cingulate
iCG	isthmus of the cingulate	rMFG	rostral middle frontal
LOG	lateral occipital	SFG	superior frontal
LOFG	lateral orbitofrontal	SPL	superior parietal
LG	lingual	STG	superior temporal
MeOFC	medial orbitofrontal	SMG	supra marginal
MTG	middle temporal	FP	frontal pole
PHG	parahippocampal	TP	temporal pole
PaCG	paracentral	TTG	transverse temporal
parsOp	pars opercularis	Ins	insula

C - cortex; **G** - gyrus; **L** - lobule

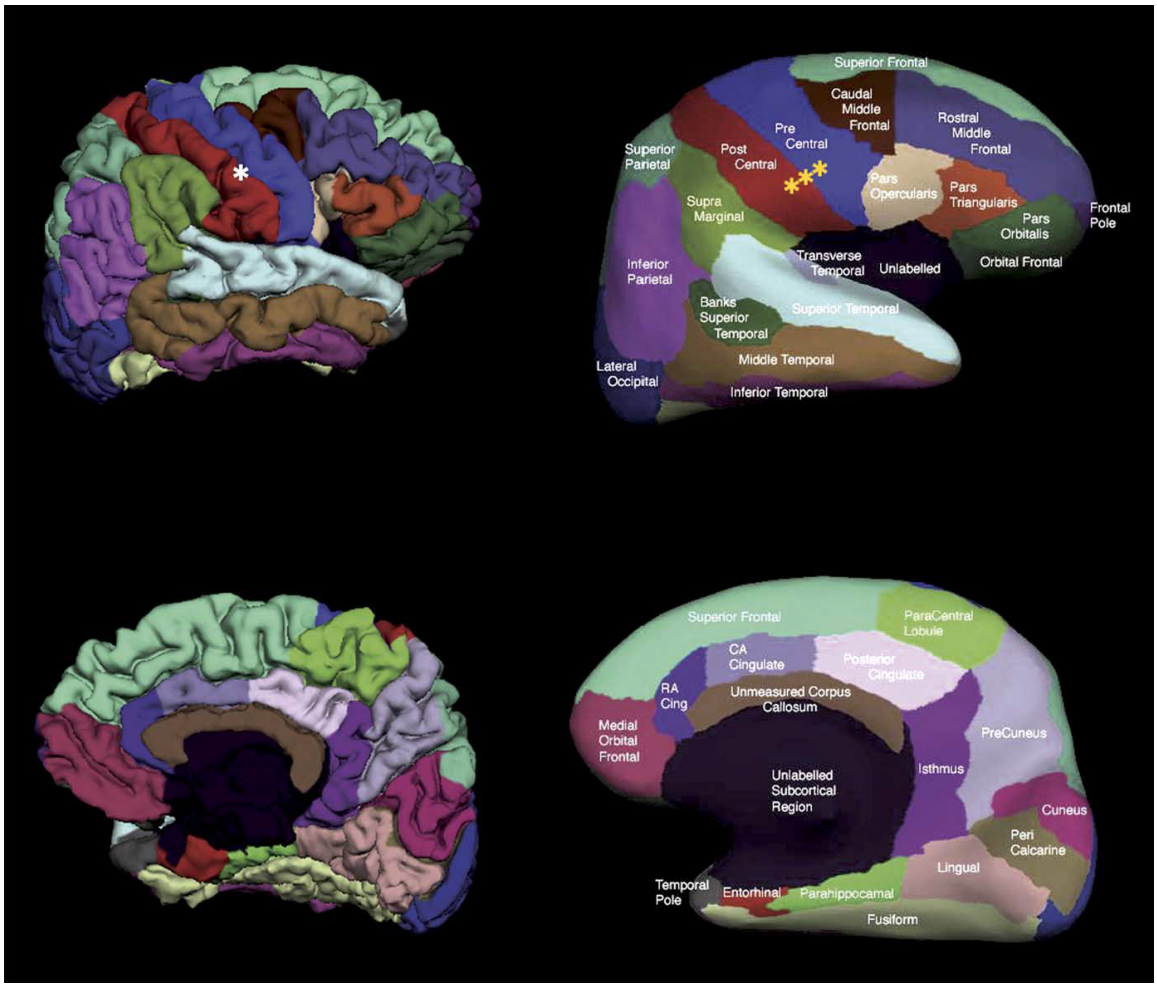

Figure B.1.: Pial (left) and inflated (right) cortical representation of one hemisphere's regions-of-interest ROI. Top row illustrates lateral view, while bottom row the medial view [72].

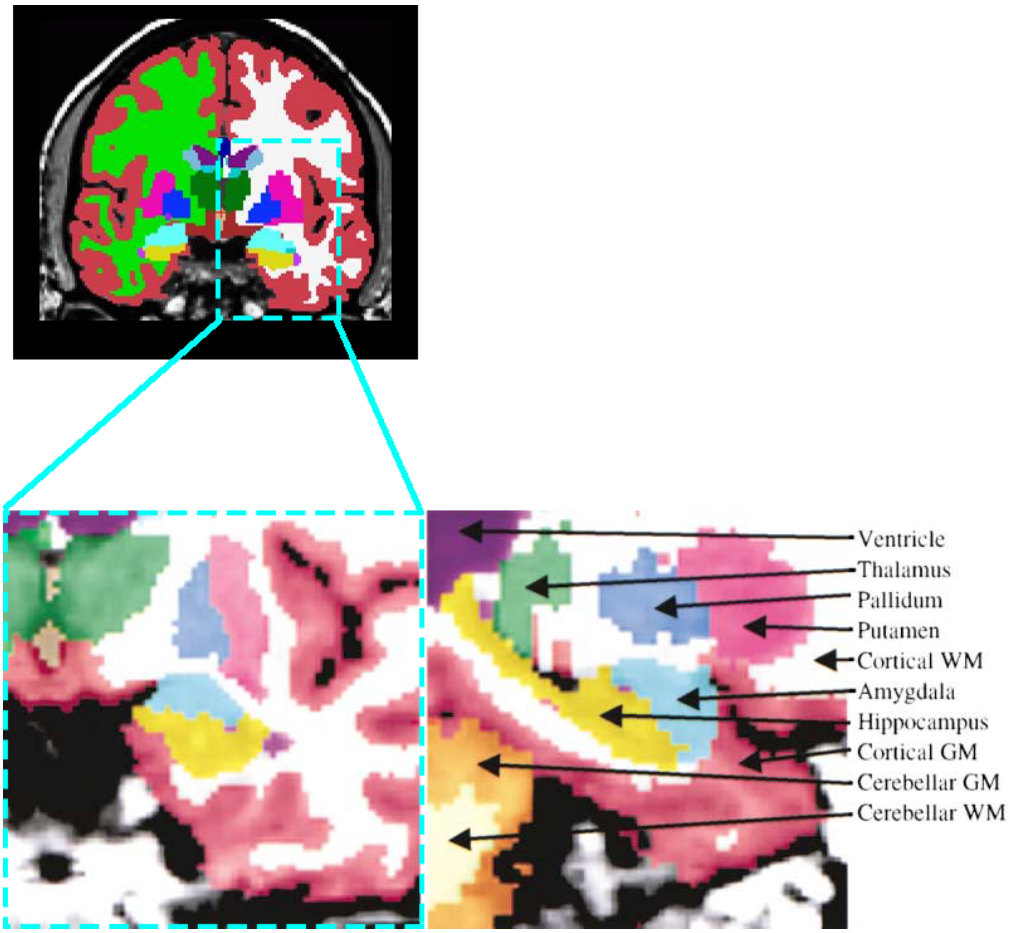

Figure B.2.: Segmentation in the temporal lobe (coronal and sagittal views on the left and right, respectively). Adapted from [71].

C. Additional results - patient images

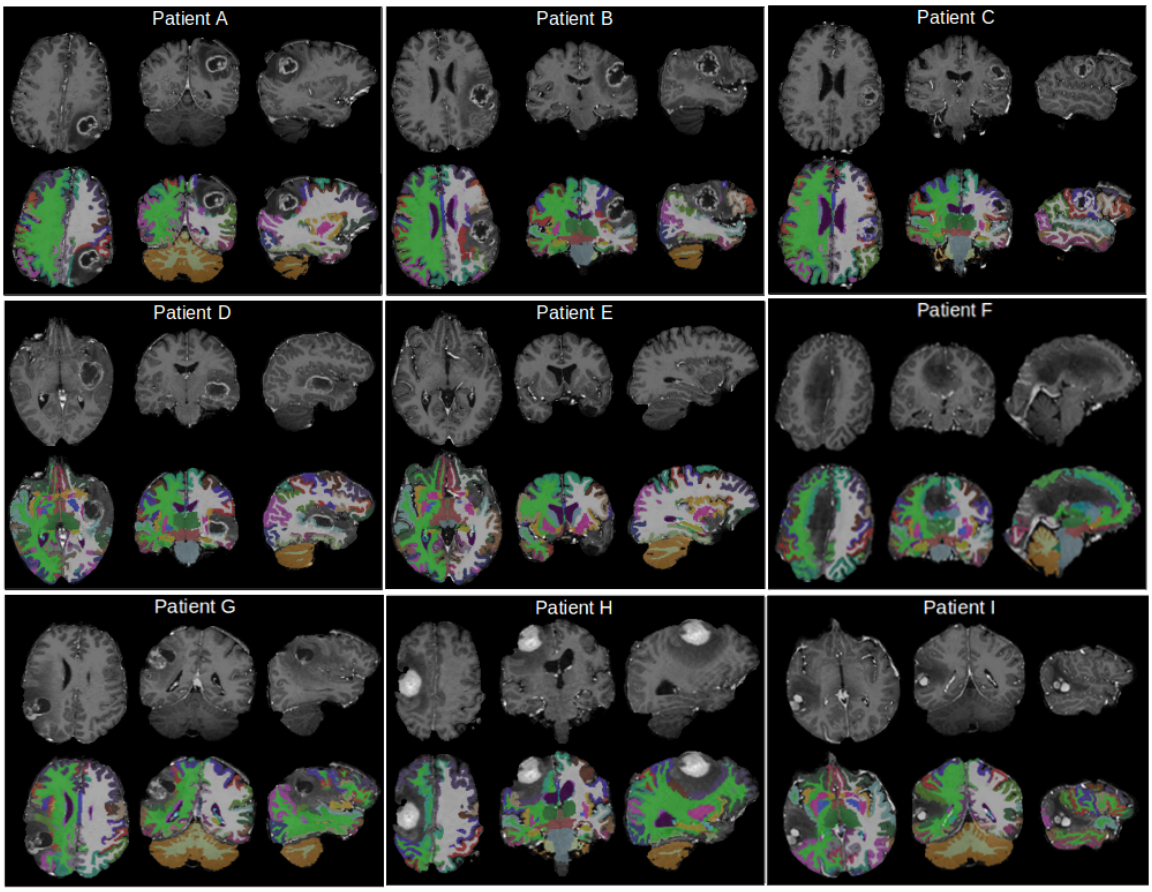

Figure C.1.: T1-weighted axial, coronal and sagittal cuts for all patients, showing the region affected by the tumour. In the first row plain T1-weighted images are shown and in the second row the correspondent parcellation obtained with freesurfer is displayed.

D. Additional results - connectograms

D. Additional results - connectograms

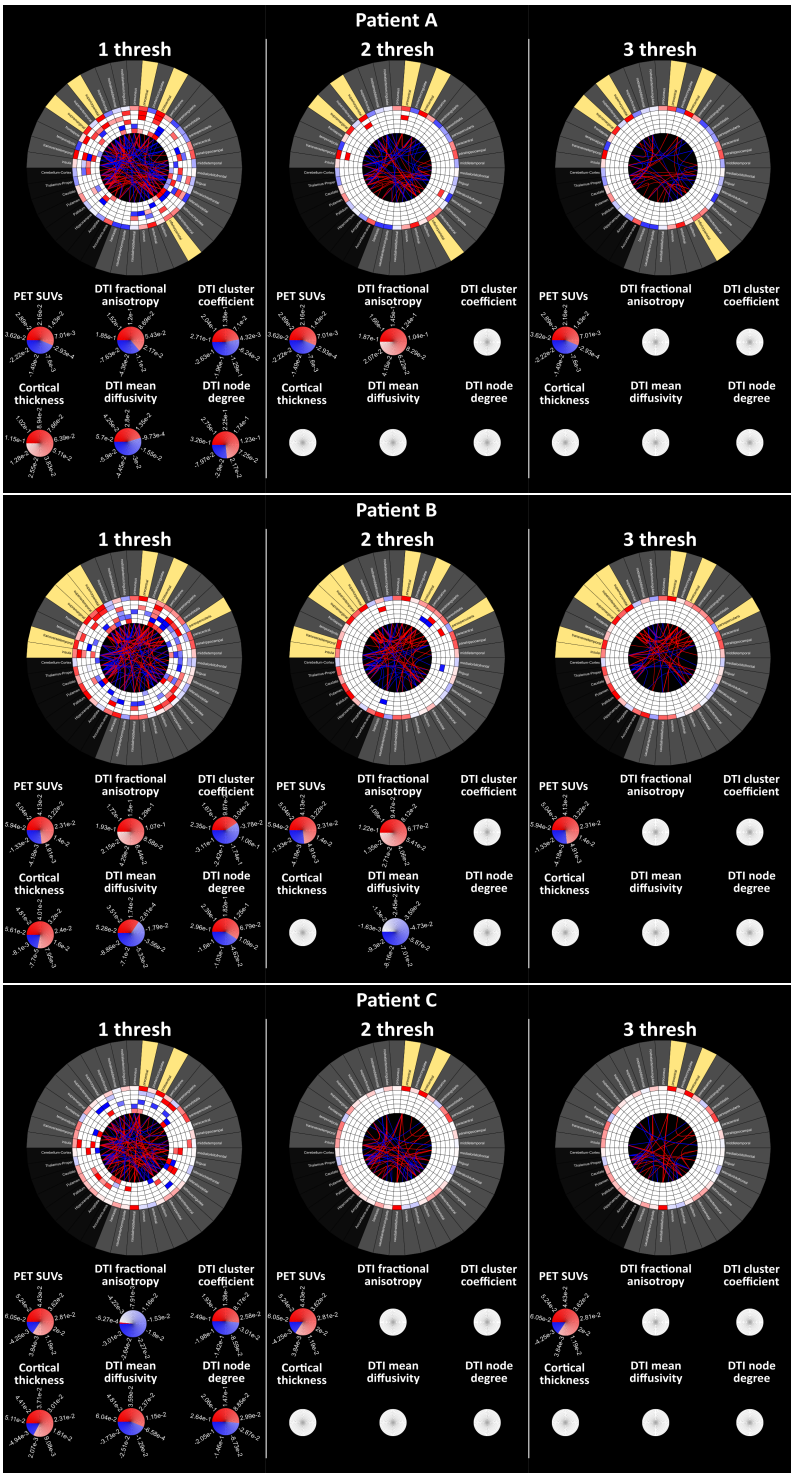

Figure D.1: Figure is continued in the next page.

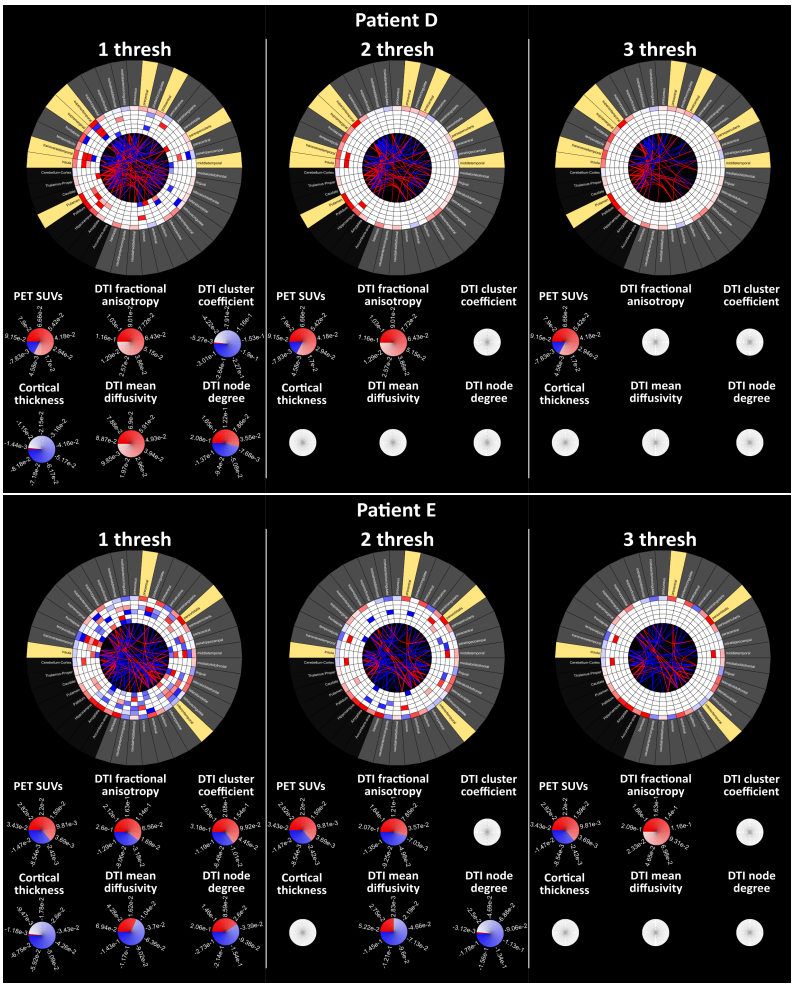

Figure D.1 ***(previous page)*:** Connectograms with the patients' asymmetry indices (AIs) data using the whole control group (p-val (unc.): 0.159, 0.025, 0.0015, for the application of three threshold levels, 1thres, 2thres and 3thres [one, two and three times the calculated value]). These connetograms correspond to patients with left-sided lesions. From the outer to the inner rings we have: cortical (dark grey) and subcortical (black) regions/ structures; SUV; CtxT; FA; MD; Deg and ClusC. Connections in the middle correspond to DTI tractography. Regions in yellow correspond to peritumoural sites.
Values presented in these connectograms represent the differences between right and left structures, regarding studied imaging and connectivity metrics.
Red/Blue blocks/lines - left hemispherical ROI presents higher/ lower values than the right hemispherical ROI; White - differences are within the normal variation range, obtained from section 4.2.1.

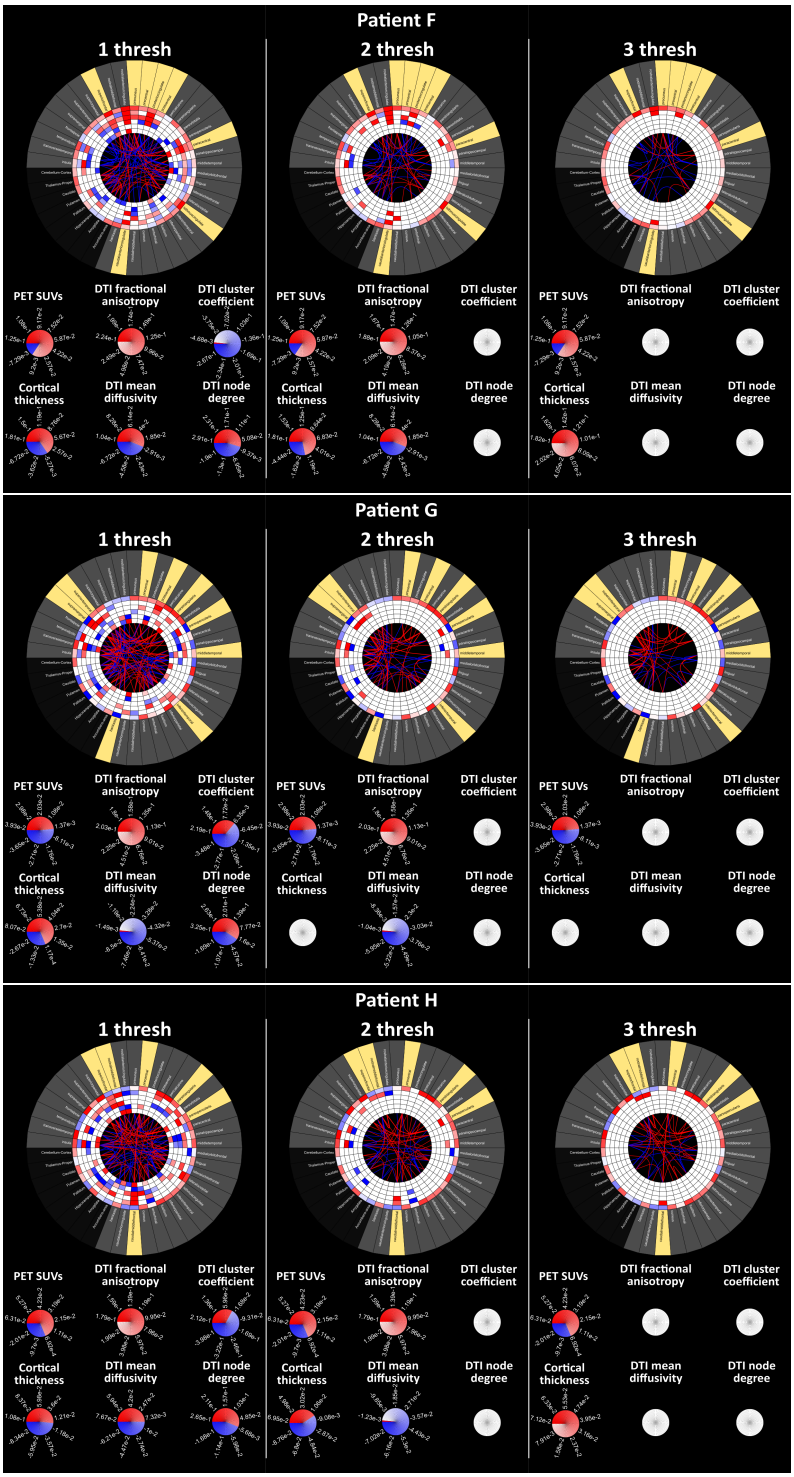

Figure D.2: Figure is continued in the next page.

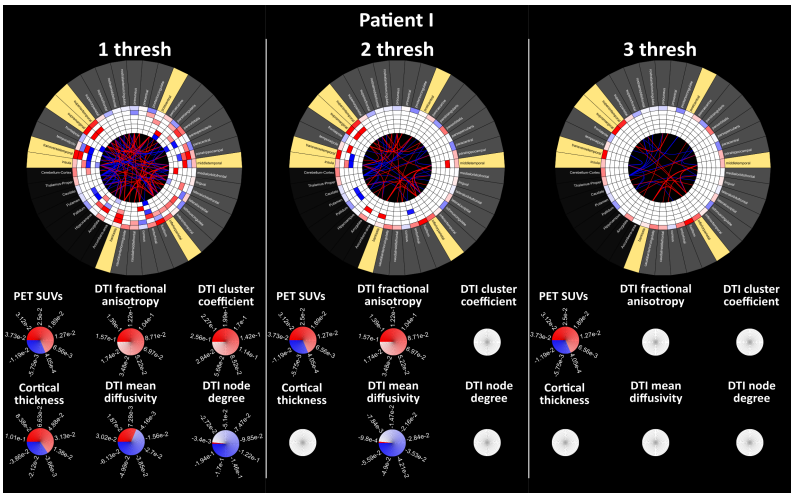

Figure D.2 ***(previous page)*****:** Connectograms with the patients' asymmetry indices (AIs) data using the whole control group (p-val (unc.): 0.159, 0.025, 0.0015, for the application of three threshold levels, 1thres, 2thres and 3thres [one, two and three times the calculated value]). These connetograms correspond to patients with right-sided lesions. From the outer to the inner rings we have: cortical (dark grey) and subcortical (black) regions/ structures; SUV; CtxT; FA; MD; Deg and ClusC. Connections in the middle correspond to DTI tractography. Regions in yellow correspond to peritumoural sites.
Values presented in these connectograms represent the differences between left and right structures, regarding studied imaging and connectivity metrics.
Red/Blue blocks/lines - right hemispherical ROI presents higher/ lower values than the left hemispherical ROI; White - differences are within the normal variation range, obtained from section 4.2.1.

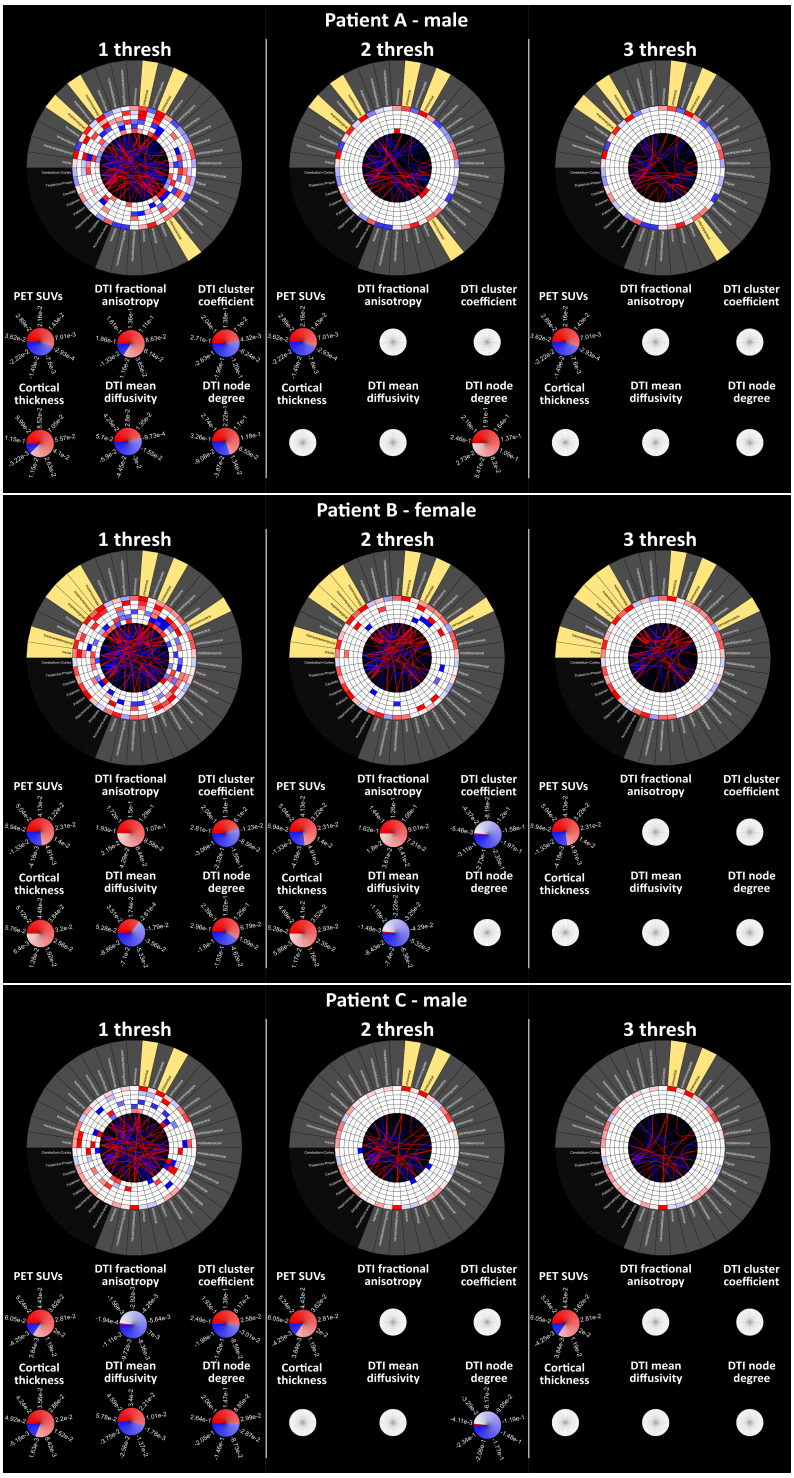

Figure D.3: Figure is continued in the next page.

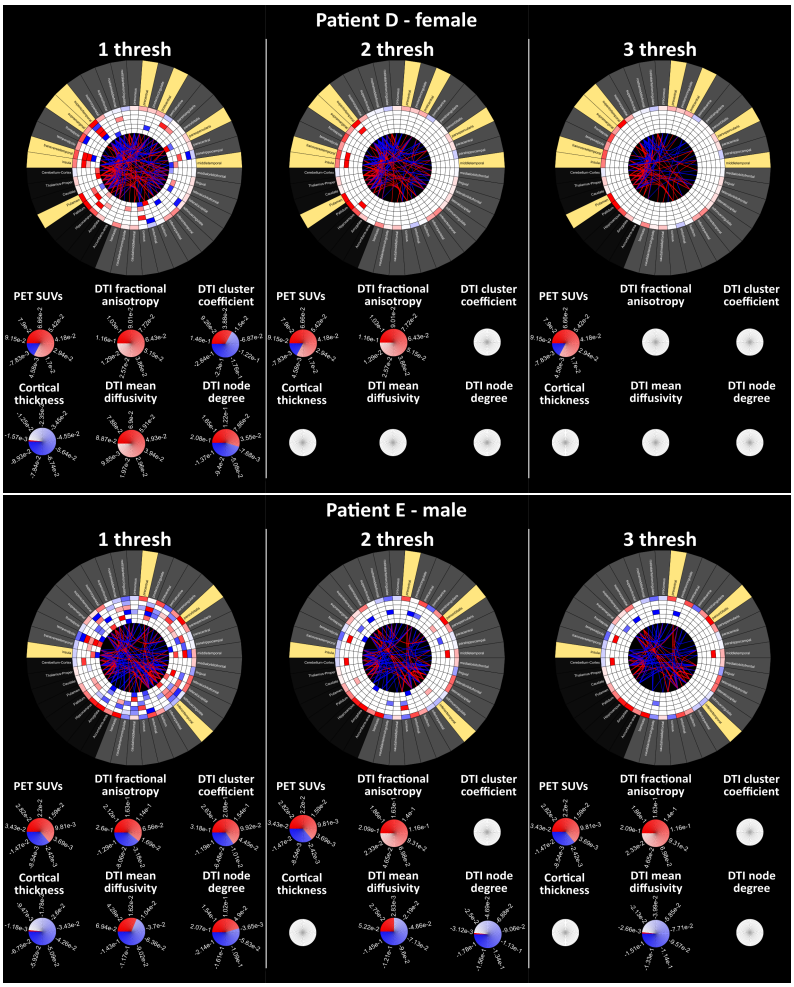

Figure D.3 ***(previous page)*:** Connectograms with the patients' asymmetry indices (AIs) data using the gender-matched control groups data (p-val (unc.): 0.159, 0.025, 0.0015, for the application of three threshold levels, 1thres, 2thres and 3thres [one, two and three times the calculated value]). These connetograms correspond to patients with left-sided lesions. From the outer to the inner rings we have: cortical (dark grey) and subcortical (black) regions/structures; SUV; CtxT; FA; MD; Deg and ClusC. Connections in the middle correspond to DTI tractography. Regions in yellow correspond to peritumoural sites.
Values presented in these connectograms represent the differences between left and right structures, regarding studied imaging and connectivity metrics.
Red/Blue blocks/lines - left hemispherical ROI presents higher/ lower values than the right hemispherical ROI; White - differences are within the normal variation range, obtained from section 4.2.1 (built with gender-matched data).

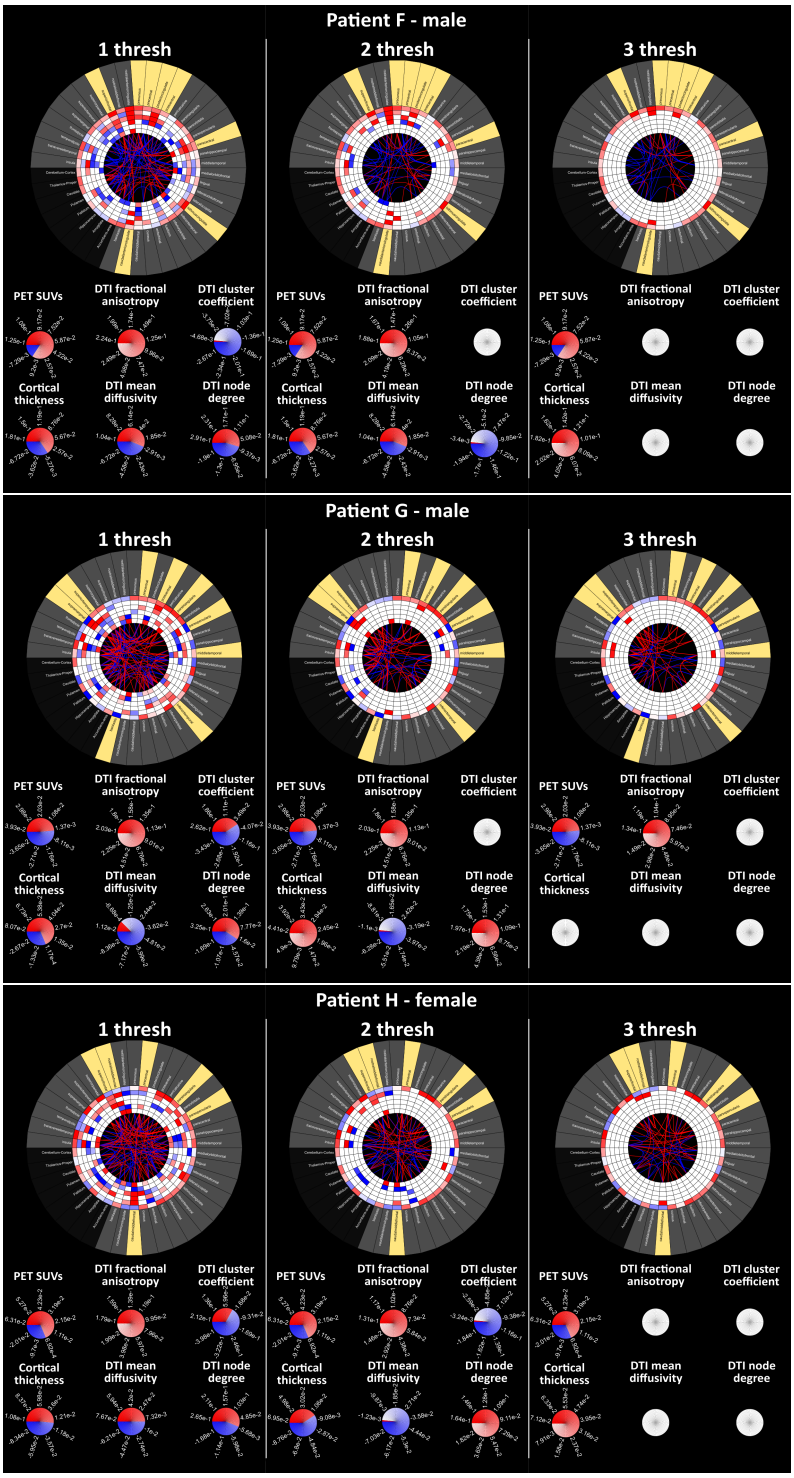

Figure D.4: Figure is continued in the next page.

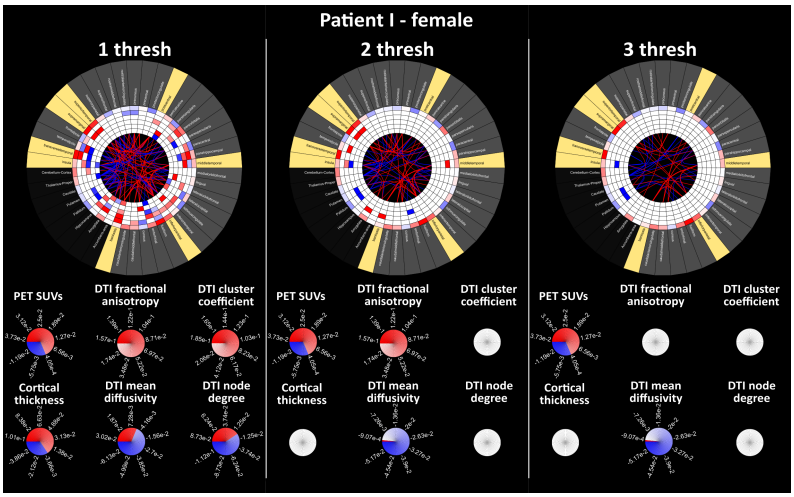

Figure D.4 ***(previous page)*****:** Connectograms with the patients' asymmetry indices (AIs) data using the gender-matched control groups data (p-val (unc.): 0.159, 0.025, 0.0015, for the application of three threshold levels, 1thres, 2thres and 3thres [one, two and three times the calculated value]). These connetograms correspond to patients with right-sided lesions. From the outer to the inner rings we have: cortical (dark grey) and subcortical (black) regions/structures; SUV; CtxT; FA; MD; Deg and ClusC. Connections in the middle correspond to DTI tractography. Regions in yellow correspond to peritumoural sites.
Values presented in these connectograms represent the differences between right and left structures, regarding studied imaging and connectivity metrics.
Red/Blue blocks/lines - right hemispherical ROI presents higher/ lower values than the left hemispherical ROI; White - differences are within the normal variation range, obtained from section 4.2.1 (built with gender-matched data).

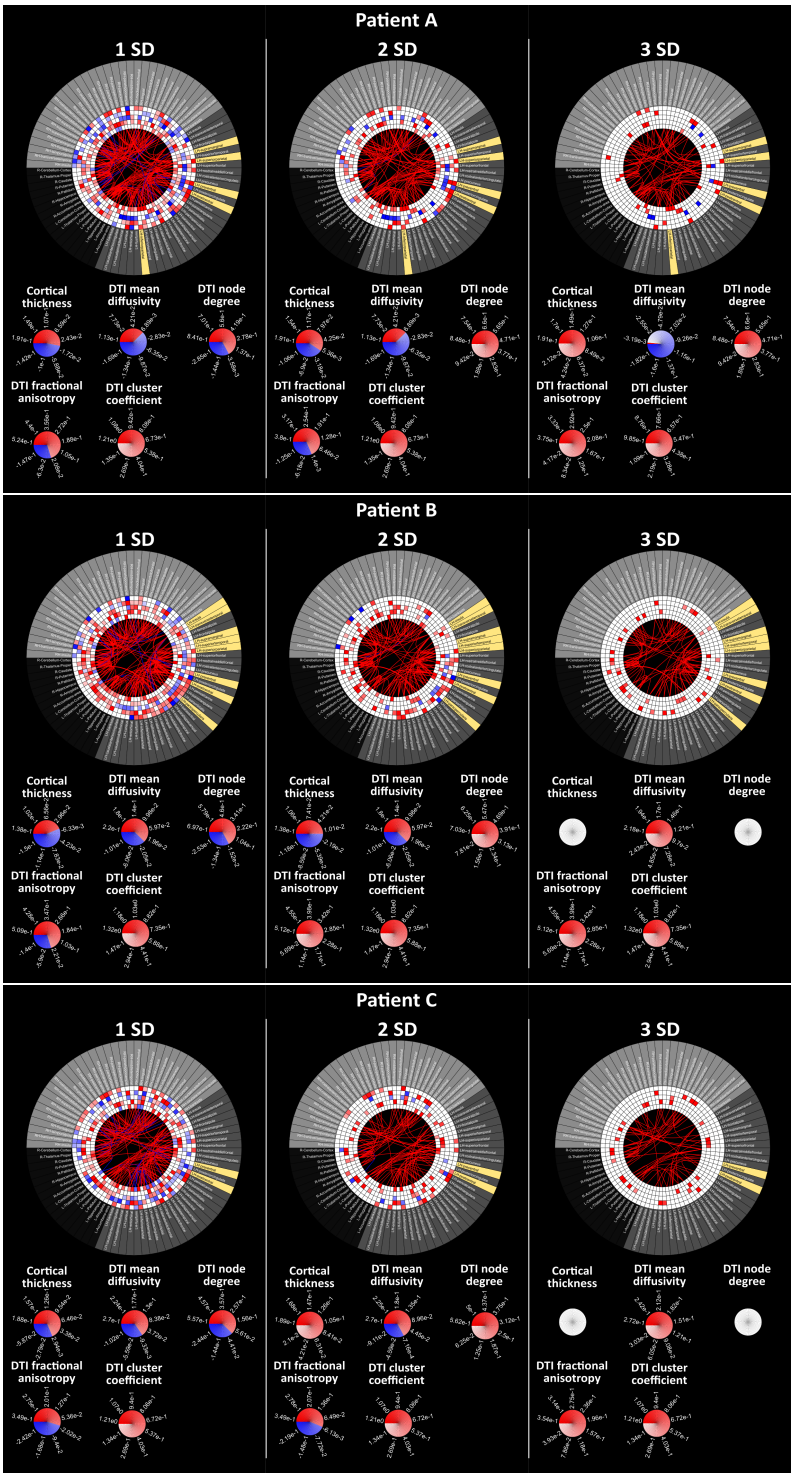

Figure D.5: Figure is continued in the next page.

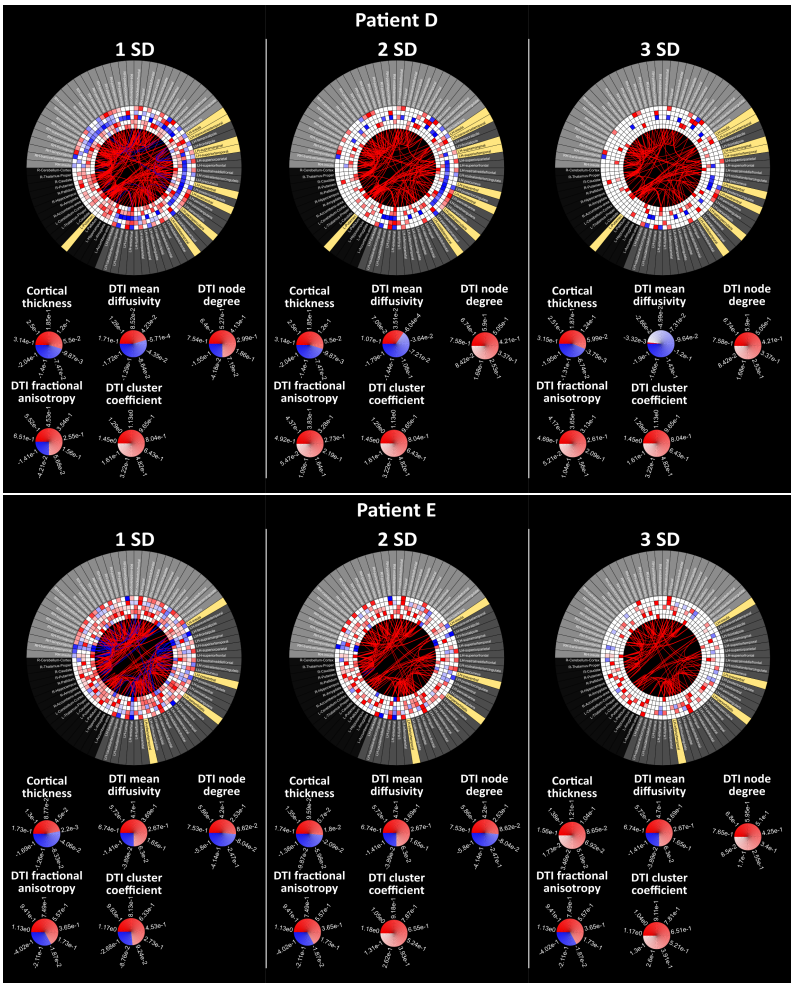

Figure D.5 ***(previous page)*****:** Connectograms with data for patients, with left-sided lesions, using the whole control group (p-val (unc.): 0.16, 0.025, 0.0015, for the application of one, two and three times the standard deviation value [1SD, 2SD and 3SD, respectively]). From the outer to the inner rings we have: left (dark grey) and right (light grey) cortical and subcortical (black) regions/structures; SUV; CtxT; FA; MD; Deg and ClusC. Connections in the middle correspond to DTI tractography. Regions in yellow correspond to peritumoural sites.
Values presented in these connectograms represent the increased or decreased ratio of the patient values related to the mean value of the control group. Red/Blue blocks/lines - ROI presents higher/lower values than the mean value of the control group; White - values are within the normal variation range. In each of these images, each column correspond to a different applied threshold in the normal variation range construction, obtained from section 4.2.2.

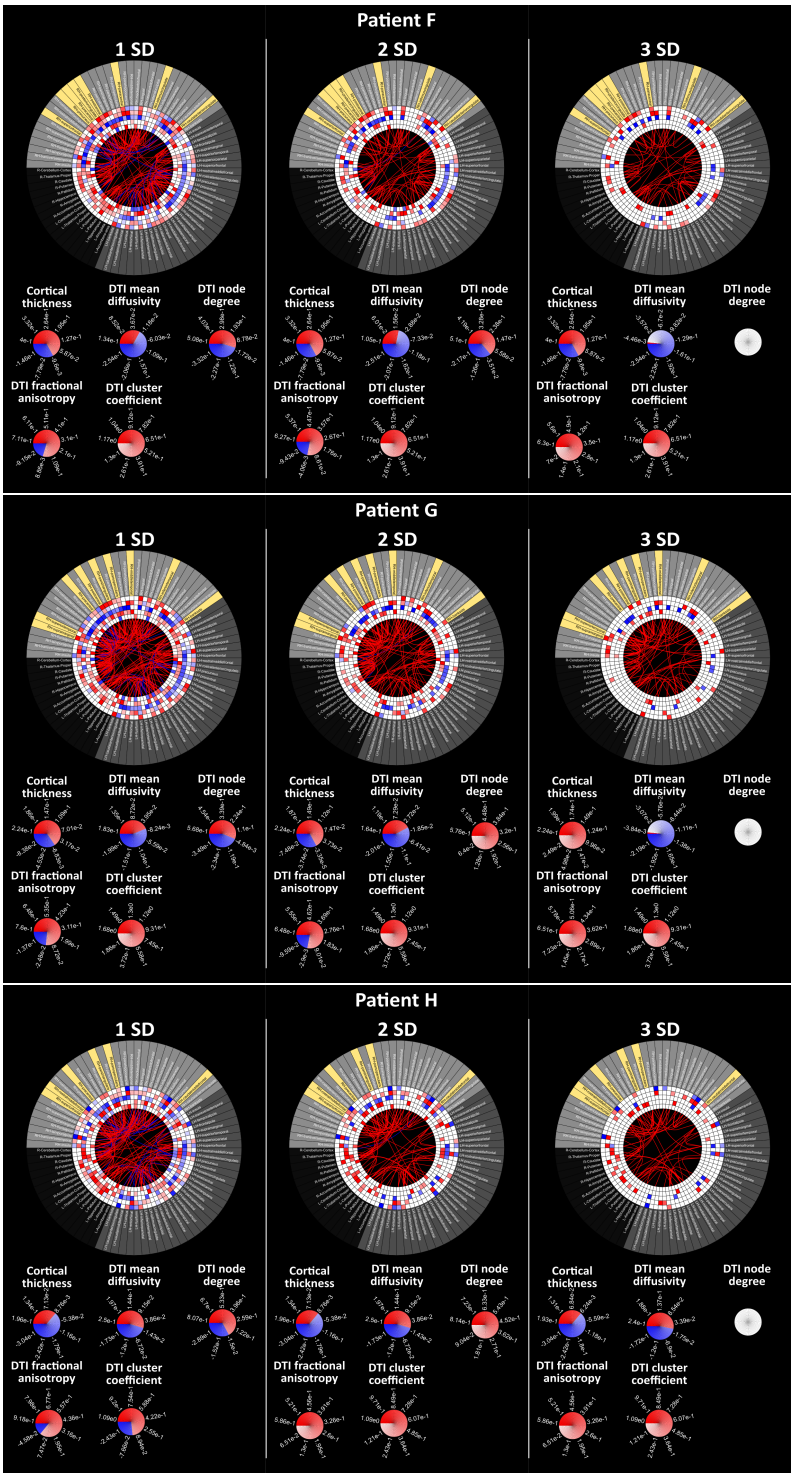

Figure D.6: Figure is continued in the next page.

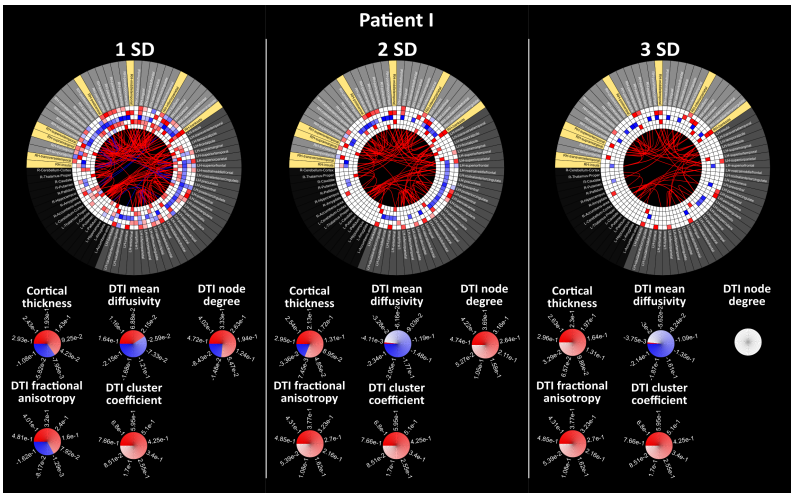

Figure D.6 ***(previous page)*****:** Connectograms with data for patients, with right-sided lesions, using the whole control group (p-val (unc.): 0.16, 0.025, 0.0015, for the application of one, two and three times the standard deviation value [1SD, 2SD and 3SD, respectively]). From the outer to the inner rings we have: left (dark grey) and right (light grey) cortical and subcortical (black) regions/structures; SUV; CtxT; FA; MD; Deg and ClusC. Connections in the middle correspond to DTI tractography. Regions in yellow correspond to peritumoural sites.
Values presented in these connectograms represent the increased or decreased ratio of the patient values related to the mean value of the control group. Red/Blue blocks/lines - ROI presents higher/lower values than the mean value of the control group; White - values are within the normal variation range. In each of these images, each column correspond to a different applied threshold in the normal variation range construction, obtained from section 4.2.2.

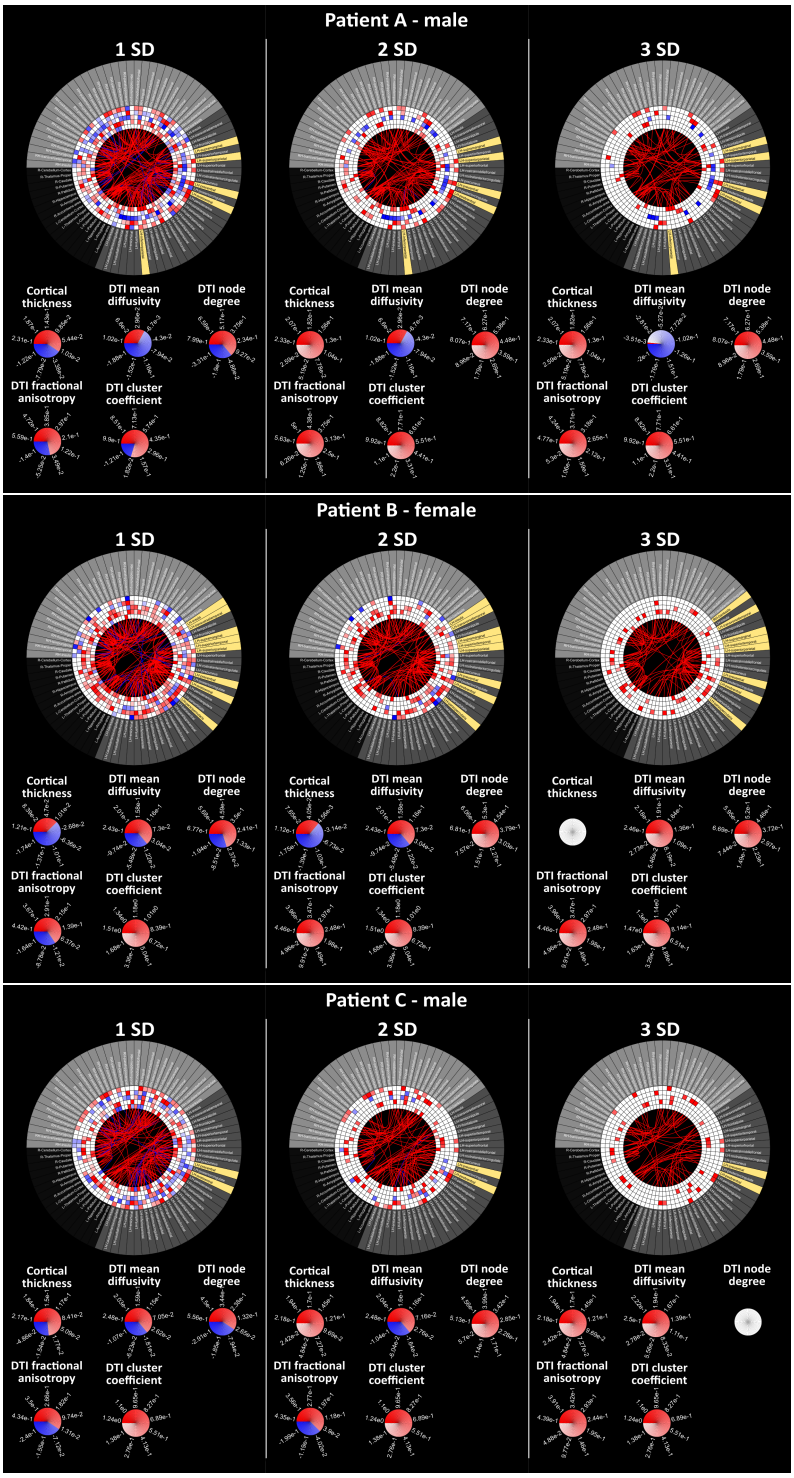

Figure D.7: Figure is continued in the next page.

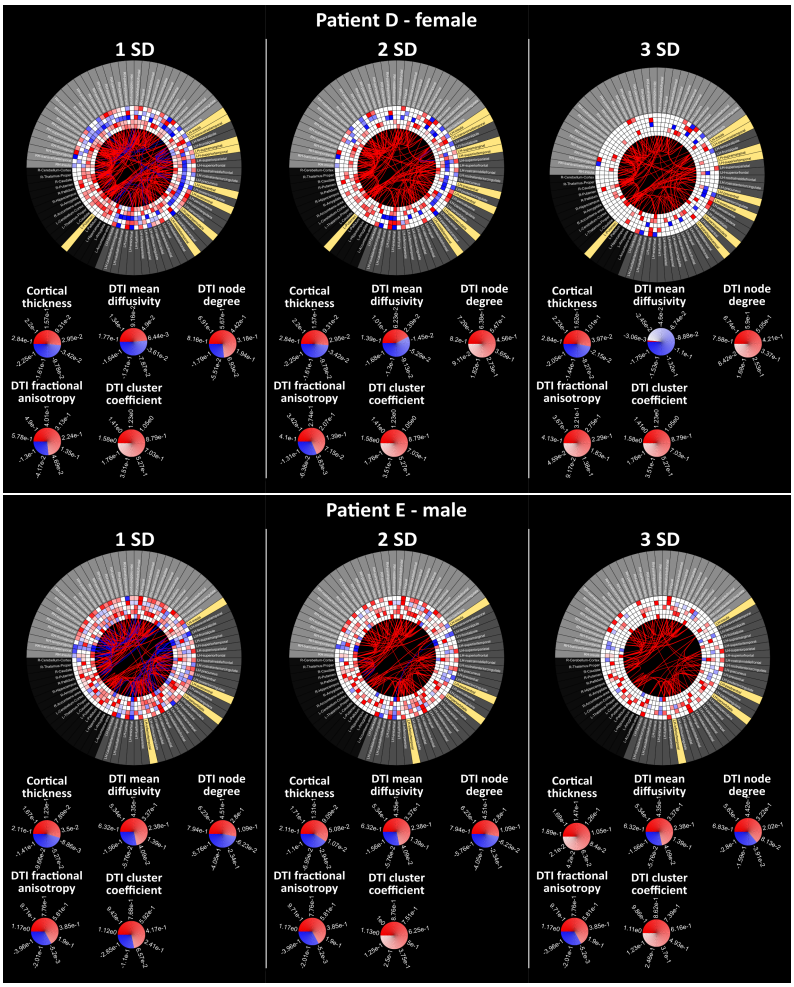

Figure D.7 ***(previous page)*****:** Connectograms with data for patients, with left-sided lesions, using the gender-matched control groups (p-val (unc.): 0.16, 0.025, 0.0015, for the application of one, two and three times the standard deviation value [1SD, 2SD and 3SD, respectively]). From the outer to the inner rings we have: left (dark grey) and right (light grey) cortical and subcortical (black) regions/ structures; SUV; CtxT; FA; MD; Deg and ClusC. Connections in the middle correspond to DTI tractography. Regions in yellow correspond to peritumoural sites.
Values presented in these connectograms represent the increased or decreased ratio of the patient values related to the mean value of the control group. Red/Blue blocks/lines - ROI presents higher/lower values than the mean value of the control group; White - values are within the normal variation range. In each of these images, each column correspond to a different applied threshold in the normal variation range construction, obtained from section 4.2.2.

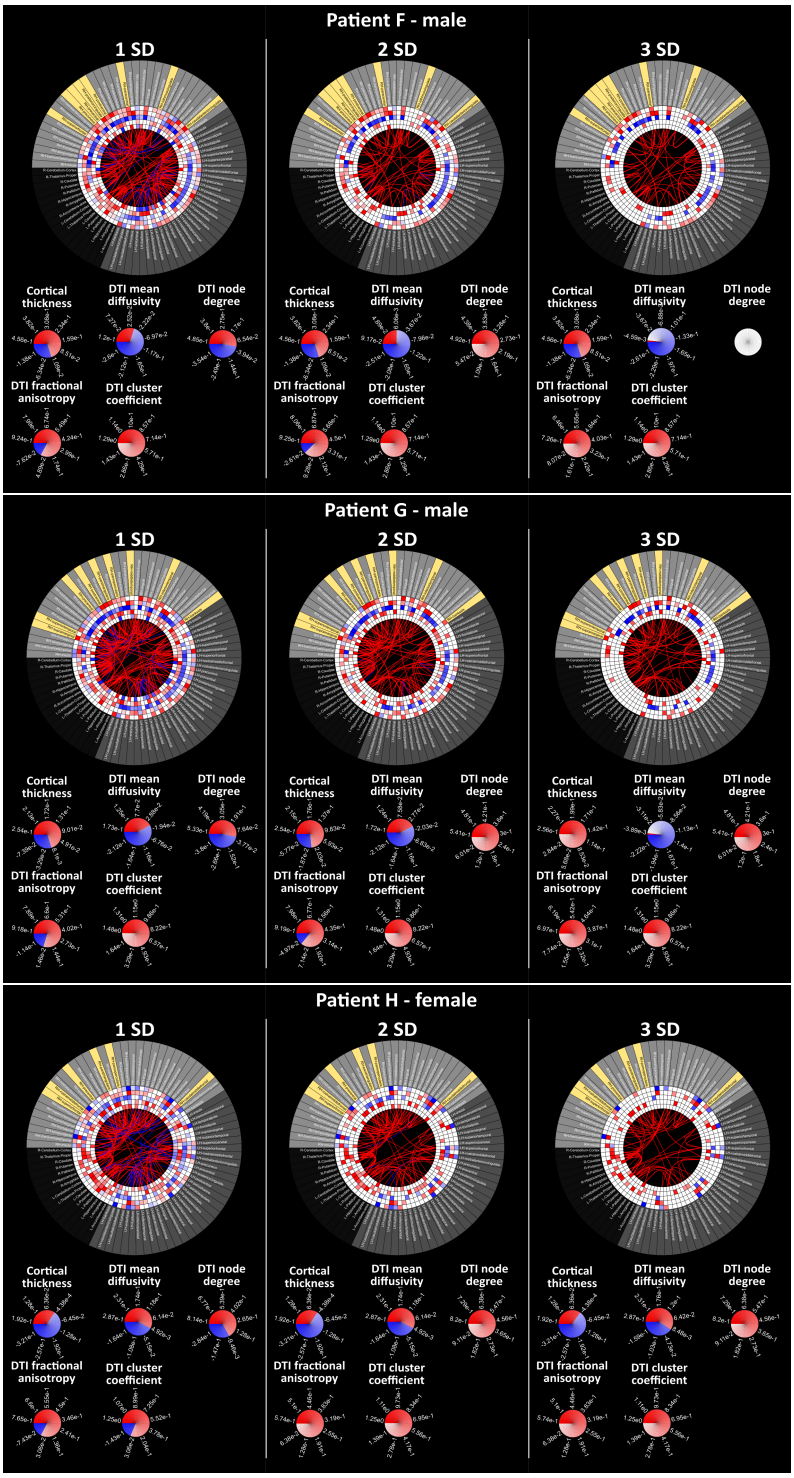

Figure D.8: Figure is continued in the next page.

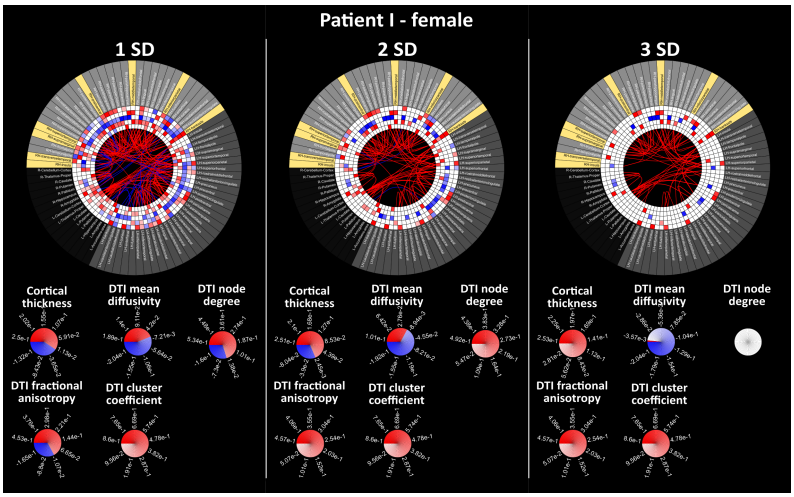

Figure D.8 ***(previous page)*****:** Connectograms with data for patients, with right-sided lesions, using the gender-matched control groups (p-val (unc.): 0.16, 0.025, 0.0015, for the application of one, two and three times the standard deviation value [1]SD, 2SD and 3SD, respectively]). From the outer to the inner rings we have: left (dark grey) and right (light grey) cortical and subcortical (black) regions/ structures; SUV; CtxT; FA; MD; Deg and ClusC. Connections in the middle correspond to DTI tractography. Regions in yellow correspond to peritumoural sites.
Values presented in these connectograms represent the increased or decreased ratio of the patient values related to the mean value of the control group. Red/Blue blocks/lines - ROI presents higher/lower values than the mean value of the control group; White - values are within the normal variation range. In each of these images, each column correspond to a different applied threshold in the normal variation range construction, obtained from section 4.2.2.

E. Additional results - tables

Table E.1.: Presented alterations correspond to data in figure D.1 and D.2 at 1thres (applied threshold correspondent to the calculated error [equation 4.3] times a factor of 1).
Bold and underlined regions correspond to two or more affected intrahemispheric metric values, respectively. For this table construction only distant regions with more than two affected metrics were reported.

Patient - Lesion	Peritumour regions	Distant regions
A – Left Parietal Lobe	Lh-PoCG, Lh-SPL, **Lh-IPL**, Lh-PCG, **Lh-SMG**	**CerebC**, **Pt**, **Hip**, **caMFG**, **ERC**, **ITG**, **iCG**, LOG, **LOFC**, LG, **MeOFC**, **PHG**, PCal, **PCn**, **raCG**, rMFG, **STG**, TTG, **Ins**
B – Left Parietal Lobe	Lh-PoCG, Lh-PCG, Lh-SMG, **Lh-parsOP**, Lh-STG, Lh-Ins, **Lh-SPL**, Lh-TTG	**Pt**, **Pd**, **Acc**, **caMFG**, **IPL**, **ITG**, **iCG**, LOG, **MeOFC**, MTG, PaCG, **parsO**, parsT, **PCal**, **raCG**, rMFG, SFG, **TP**
C – Left Parietal Lobe	Lh-PCG, Lh-PoCG	**CerebC**, **Am**, **Acc**, LOG, **LOFC**, **MeOFC**, **parsO**, **parsT**, **PCn**, **SPL**, **TP**, **Ins**
D – Left Temporal Lobe	Lh-STG, Lh-SMG, Lh-PoCG, Lh-PCG, Lh-parsOP, Lh-MTG, Lh-Pt, **Lh-Ins**, Lh-TTG	**Hip**, **Cn**, **IPL**, **PHG**, **pCG**
E – Left Temporal Lobe	**Lh-Ins**, Lh-parsO, Lh-PCG, Lh-ITG	Am, bankssts, **caCG**, caMFG, **Cn**, ERC, iCG, **LOG**, LOFC, MTG, **PHG**, **PaCG**, **parsT**, **PoCG**, **pCG**, raCG, rMFG, **SPL**, **STG**, **SMG**, TP
F – Right Frontal Lobe	Rh-SFG, **Rh-PCG**, Rh-pCG, **Rh-PoCG**, Rh-PaCG, **Rh-PCn**, Rh-iCG, **Rh-caCG**	**CerebC**, **Pt**, Hip, **bankssts**, caMFG, FG, ITG, **LOFC**, **LG**, MeOFC, MTG, **parsOP**, raCG, **rMFG**, SPL, STG, TP, Ins
G – Right Temporal Lobe	Rh-SMG, Rh-PCG, **Rh-parsOP**, **Rh-PoCG**, **Rh-ITG**, Rh-MTG, Rh-bankssts, **Rh-STG**, **Rh-parsT**	**Pt**, Hip, caCG, ERC, **PHG**, **pCG**, **raCG**, **rMFG**, SPL, TTG, **Ins**
H – Right Frontal Lobe	Rh-PCG, Rh-caMFG, Rh-rMFG, Rh-SFG, **Rh-parsT**, Rh-parsOP	**Pt**, **Pd**, **Hip**, Am, Acc, **bankssts**, caCG, **Cn**, ERC, **ITG**, LOFC, LOG, MTG, PHG, **PoCG**, raCG, **SPL**, **STG**, **SMG**, **TP**, Ins
I – Right Temporal Lobe	Rh-SMG, Rh-bankssts, **Rh-MTG**, Rh-PoCG, Rh-IPL, Rh-STG, Rh-Ins, **Rh-TTG**	**Hip**, **Am**, **Cn**, ERC, **FG**, **LOFC**, PHG, **parsOP**, **parsO**, **PCal**, TP

Lh – Left hemisphere; Rh – Right hemisphere; G – Gyrus; L- Lobule; C – Cortex.
ITG – inferior temporal; MTG – medial temporal; STG – superior temporal; TTG – transverse temporal; SMG – supramarginal; SPL – superior parietal; IPL – inferior parietal; SFG – superior frontal; LOFC – lateral orbitofrontal; MeOFC – medial orbitofrontal; rMFG – rostral middle frontal; caMFG – caudal middle frontal; LOG – lateral occipital; FG – frontal; TP – temporal; PHG – parahippocampal; pCG – posterior cingulate; iCG – isthmus of the cingulate; caCG – caudal anterior cingulate; raCG – rostral anterior cingulate; PCG – precentral; PoCG – postcentral; PaCG – paracentral; PCal - pericalcarine; parsT – pars triangularis; parsO – pars otbitalis; parsOP – pars opercularis; ERC – entorhinal; PCn – precuneus; Cn – cuneus; bankssts – banks of the superior temporal sulcus; CerebC – cerebellar; Am – amygdala; Pt – putamen; Pd – pallidum; Hip – hippocampus; Ins – insula.

Table E.2.: Presented alterations correspond to data in figure D.3 and D.4 at 1thres (applied threshold correspondent to the calculated error [equation 4.3] times a factor of 1.
Bold and underlined regions correspond to two or more affected intrahemispheric metric values, respectively. For this table construction only distant regions with more than two affected metrics were reported.

Patient - Lesion	Peritumour regions	Distant regions
A (male) – Left Parietal Lobe	Lh-PoCG, Lh-SPL, Lh-IPL, Lh-PCG, Lh-SMG	**CerebC**, **Hip**, **Am**, **caMFG**, IPL, **ITG**, **iCG**, LOG, **LOFC**, LG, MeOFC, MTG, **PHG**, PCal, PCn, **raCG**, rMFG, **FP**, TTG, Ins
B (female) – Left Parietal Lobe	Lh-PoCG, **Lh-PCG**, Lh-SMG, Lh-parsOP, Lh-STG, Lh-Ins, **Lh-SPL**, Lh-TTG	**CerebC**, **Pt**, **Pd**, **Am**, **caMFG**, **FG**, **IPL**, **ITG**, **iCG**, LOG, LOFC, **LG**, **PaCG**, parsO, parsT, PCal, raCG, rMFG, **SFG**, **TP**
C (male) – Left Parietal Lobe	Lh-PCG, Lh-PoCG	**CerebC**, **Am**, **Acc**, LOG, LOFC, **MTG**, **parsO**, **PCn**, **SPL**, **TP**, **Ins**
D (female) – Left Temporal Lobe	Lh-STG, Lh-SMG, Lh-PoCG, Lh-PCG, **Lh-parsOP**, **Lh-MTG**, Lh-Pt, **Lh-Ins**, Lh-TTG	**Pt**, **Hip**, Cn, **ERC**, **MTG**, **PHG**
E (male) – Left Temporal Lobe	**Lh-Ins**, Lh-parsO, Lh-PCG, Lh-ITG	Am, **bankssts**, **caCG**, caMFG, **Cn**, ERC, ITG, iCG, **LOG**, **LOFC**, MTG, **PHG**, **PaCG**, **parsT**, **PoCG**, pCG, raCG, **rMFG**, **SPL**, **STG**, **SMG**, TP
F (male) – Right Frontal Lobe	Rh-SFG, **Rh-PCG**, Rh-pCG, **Rh-PoCG**, Rh-PaCG, **Rh-PCn**, **Rh-iCG**, **Rh-caCG**	**CerebC**, **Pt**, Hip, bankssts, **caCG**, caMFG, FG, ITG, **LOFC**, **LG**, MeOFC, MTG, **parsOP**, **parsT**, raCG, **rMFG**, SPL, STG, **SMG**, TP, Ins
G (male) – Right Temporal Lobe	Rh-SMG, Rh-PCG, **Rh-parsOP**, **Rh-PoCG**, **Rh-ITG**, Rh-MTG, **Rh-bankssts**, **Rh-STG**, **Rh-parsT**	**Pt**, Hip, caCG, ERC, FG, **iCG**, **PHG**, **pCG**, **raCG**, **rMFG**, SPL, TTG, **Ins**
H (female) – Right Frontal Lobe	**Rh-PCG**, Rh-caMFG, Rh-rMFG, Rh-SFG, Rh-parsT, Rh-parsOP	**CerebC**, **Cd**, **Pt**, **Pd**, **Hip**, **Am**, Acc, **bankssts**, caCG, caMFG, **Cn**, ERC, **FG**, **ITG**, LOFC, **LOG**, MTG, PHG, **PoCG**, raCG, **SMG**, TP, Ins
I (female) – Right Temporal Lobe	Rh-SMG, Rh-bankssts, **Rh-MTG**, Rh-PoCG, Rh-IPL, Rh-STG, Rh-Ins, **Rh-TTG**	**Hip**, Am, **Cn**, ERC, FG, **ITG**, **LOG**, **LOFC**, PHG, **parsO**, **PCal**, TP

Lh – Left hemisphere; Rh – Right hemisphere; G – Gyrus; L- Lobule; C – Cortex.
ITG – inferior temporal; MTG – medial temporal; STG – superior temporal; TTG – transverse temporal; SMG – supramarginal; SPL – superior parietal; IPL – inferior parietal; SFG – superior frontal; LOFC – lateral orbitofrontal; MeOFC – medial orbitofrontal; rMFG – rostral middle frontal; caMFG – caudal middle frontal; LOG – lateral occipital; FG – frontal; TP – temporal; PHG – parahippocampal; pCG – posterior cingulate; iCG – isthmus of the cingulate; caCG – caudal anterior cingulate; raCG – rostral anterior cingulate; PCG – precentral; PoCG – postcentral; PaCG – paracentral; PCal - pericalcarine; parsT – pars triangularis; parsO – pars otbitalis; parsOP – pars opercularis; ERC – entorhinal; PCn – precuneus; Cn – cuneus; bankssts – banks of the superior temporal sulcus; CerebC – cerebellar; Am – amygdala; Pt – putamen; Pd – pallidum; Hip – hippocampus; Ins – insula.

Table E.3.: Presented alterations correspond to data in figure D.5 and D.6at 3SD (3 times the standard deviation).
Bold and underlined regions correspond to two or more affected intrahemispheric metric values, respectively. For this table construction only distant regions with more than two affected metrics were reported.

Patient - Lesion	Peritumour regions	Distant regions
A – Left Parietal Lobe	Lh-PoCG, Lh-SPL, Lh-IPL, Lh-PCG, Lh-SMG	**Lh-LG**, **Lh-SFG**, **Rh-ERC**, **Rh-parsT**
B – Left Parietal Lobe	Lh-PoCG, Lh-PCG, Lh-SMG, Lh-parsOP, Lh-STG, **Lh-Ins**, Lh-SPL, Lh-TTG	**Lh-CerebC**, **Rh-Pt**
C – Left Parietal Lobe	Lh-PCG, Lh-PoCG	**Rh-LOFC**
D – Left Temporal Lobe	Lh-STG, Lh-SMG, **Lh-PoCG**, Lh-PCG, **Lh-parsOP**, Lh-MTG, Lh-Pt, Lh-Ins, Lh-TTG	***Rh-Pt***, **Lh-bankssts**, **Lh-caCG**, Lh-ERC, **Lh-LG**, **Lh-parsT**, **Lh-pCG**, **Lh-SFG**, Rh-ERC, **Rh-IPL**, **Rh-LG**, **Rh-parsT**
E – Left Temporal Lobe	Lh-Ins, Lh-parsO, Lh-PCG, Lh-ITG	**Rh-Pt**, Lh-bankssts, **Lh-ERC**, **Lh-iCG**, **Lh-LOFC**, **Lh-LG**, **Lh-MeOFC**, **Lh-PoCG**, **Lh-rMFG**, **Rh-ERC**, **Rh-FG**, Rh-LOG, **Rh-LG**, **Rh-PHG**, **Rh-parsOP**, Rh-parsT, ***Rh-PCG***, **Rh-raCG**, **Rh-SPL**, **Rh-TP**, *Rh-Ins*
F – Right Frontal Lobe	Rh-SFG, Rh-PCG, Rh-pCG, **Rh-PoCG**, **Rh-PaCG**, Rh-PCn, Rh-iCG, Rh-caCG	**Lh-IPL**, **Lh-parsOP**, **Lh-parsO**, **Lh-parsT**, Lh-rMFG, Rh-ERC, **Rh-FG**, Rh-LG, **Rh-PHG**, Rh-parsT, **Rh-TP**, **Rh-Ins**
G – Right Temporal Lobe	Rh-SMG, **Rh-PCG**, **Rh-parsOP**, Rh-PoCG, Rh-ITG, **Rh-MTG**, Rh-bankssts, Rh-STG, Rh-parsT	*Lh-bankssts*, **Rh-ERC**, **Rh-FG**, **Rh-PHG**, **Rh-SFG**, **Rh-Ins**, **Rh-SMG**, **Rh-STG**
H – Right Frontal Lobe	Rh-PCG, **Rh-caMFG**, Rh-rMFG, Rh-SFG, Rh-parsT, Rh-parsOP	**Rh-Pd**, **Lh-caCG**, **Lh-parsO**, Lh-raCG, ***Lh-SFG***, **Lh-TP**, Rh-ERC, **Rh-FG**, **Rh-PHG**, **Rh-PoCG**, **Rh-raCG**, **Rh-TP**, **Rh-Ins**
I – Right Temporal Lobe	Rh-SMG, Rh-bankssts, Rh-MTG, Rh-PoCG, Rh-IPL, Rh-STG, Rh-Ins, Rh-TTG	***Lh-bankssts***, **Lh-LG**, **Rh-ERC**, **Rh-MTG**, **Rh-PHG**, **Rh-PCal**

Lh – Left hemisphere; Rh – Right hemisphere; G – Gyrus; L- Lobule; C – Cortex.
ITG – inferior temporal; MTG – medial temporal; STG – superior temporal; TTG – transverse temporal; SMG – supramarginal; SPL – superior parietal; IPL – inferior parietal; SFG – superior frontal; LOFC – lateral orbitofrontal; MeOFC – medial orbitofrontal; rMFG – rostral middle frontal; caMFG – caudal middle frontal; LOG – lateral occipital; FG – frontal; TP – temporal; PHG – parahippocampal; pCG – posterior cingulate; iCG – isthmus of the cingulate; caCG – caudal anterior cingulate; raCG – rostral anterior cingulate; PCG – precentral; PoCG – postcentral; PaCG – paracentral; PCal - pericalcarine; parsT – pars triangularis; parsO – pars otbitalis; parsOP – pars opercularis; ERC – entorhinal; PCn – precuneus; Cn – cuneus; bankssts – banks of the superior temporal sulcus; CerebC – cerebellar; Am – amygdala; Pt – putamen; Pd – pallidum; Hip – hippocampus; Ins – insula.

Table E.4.: Presented alterations correspond to data in figure D.7 and D.8 at 3SD (3 times the standard deviation).
Bold and underlined regions correspond to two or more affected intrahemispheric metric values, respectively. For this table construction only distant regions with more than two affected metrics were reported.

Patient - Lesion	Peritumour regions	Distant regions
A (male) – Left Parietal Lobe	**Lh-PoCG**, Lh-SPL, Lh-IPL, Lh-PCG, Lh-SMG	**Lh-Cn**, **Lh-LG**, **Lh-PCal**, Lh-rMFG, **Lh-TP**, **Rh-ERC**, **Rh-parsOP**, **Rh-parsT**
B (female) – Left Parietal Lobe	Lh-PoCG, Lh-PCG, Lh-SMG, **Lh-parsOP**, Lh-STG, **Lh-Ins**, Lh-SPL, Lh-TTG	**Lh-CerebC**, **Lh-Tha**, **Lh-raCG**, **Lh-Ins**, **Rh-PHG**, **Rh-Pt**
C (male) – Left Parietal Lobe	Lh-PCG, Lh-PoCG	**Lh-parsT**, **Lh-SPL**, **Rh-LOFC**
D (female) – Left Temporal Lobe	Lh-STG, Lh-SMG, **Lh-PoCG**, **Lh-PCG**, **Lh-parsOP**, Lh-MTG, Lh-Pt, Lh-Ins, Lh-TTG	**Lh-Hip**, **Lh-bankssts**, Lh-Cn, Lh-ERC, **Lh-parsT**, **Lh-pCG**, **Lh-SFG**, **Rh-caCG**, Rh-ERC, **Rh-IPL**, **Rh-PHG**, **Rh-parsT**, *Rh-Pt*
E (male) – Left Temporal Lobe	Lh-Ins, Lh-parsO, Lh-PCG, Lh-ITG	Lh-bankssts, Lh-ERC, **Lh-FG**, **Lh-iCG**, **Lh-LG**, **Lh-parsT**, **Lh-pCG**, **Lh-PCn**, **Lh-rMFG**, **Lh-SPL**, **Lh-TP**, **Rh-bankssts**, **Rh-ERC**, **Rh-FG**, Rh-LOG, **Rh-LG**, **Rh-PHG**, Rh-parsT, **Rh-raCG**, **Rh-rMFG**, **Rh-SPL**, Rh-TP, *Rh-Ins*, **Rh-Hip**
F (male) – Right Frontal Lobe	Rh-SFG, **Rh-PCG**, Rh-pCG, **Rh-PoCG**, **Rh-PaCG**, Rh-PCn, Rh-iCG, Rh-caCG	***Lh-caCG***, **Lh-Cn**, **Lh-FG**, **Lh-IPL**, **Lh-LG**, **Lh-MeOFC**, **Lh-parsOP**, Lh-parsO, **Lh-parsT**, **Lh-PCal**, ***Lh-PoCG***, **Lh-rMFG**, *Lh-SFG*, **Lh-SPL**, **Rh-Cn**, Rh-ERC, **Rh-FG**, Rh-LG, **Rh-PHG**, **Rh-parsOP**, Rh-parsT, **Rh-PCal**, **Rh-raCG**, **Rh-SPL**, **Rh-STG**, **Rh-TP**, **Rh-TTG**, **Rh-Ins**

Lh – Left hemisphere; Rh – Right hemisphere; G – Gyrus; L- Lobule; C – Cortex.
ITG – inferior temporal; MTG – medial temporal; STG – superior temporal; TTG – transverse temporal; SMG – supramarginal; SPL – superior parietal; IPL – inferior parietal; SFG – superior frontal; LOFC – lateral orbitofrontal; MeOFC – medial orbitofrontal; rMFG – rostral middle frontal; caMFG – caudal middle frontal; LOG – lateral occipital; FG – frontal; TP – temporal; PHG – parahippocampal; pCG – posterior cingulate; iCG – isthmus of the cingulate; caCG – caudal anterior cingulate; raCG – rostral anterior cingulate; PCG – precentral; PoCG – postcentral; PaCG – paracentral; PCal - pericalcarine; parsT – pars triangularis; parsO – pars otbitalis; parsOP – pars opercularis; ERC – entorhinal; PCn – precuneus; Cn – cuneus; bankssts – banks of the superior temporal sulcus; CerebC – cerebellar; Am – amygdala; Pt – putamen; Pd – pallidum; Hip – hippocampus; Ins – insula.

Patient - Lesion	Peritumour regions	Distant regions
G (male) – Right Temporal Lobe	**Rh-SMG**, **Rh-PCG**, Rh-parsOP, Rh-PoCG, Rh-ITG, **Rh-MTG**, Rh-bankssts, Rh-STG, **Rh-parsT**	***Lh-bankssts***, **Lh-caCG**, **Lh-FG**, **Lh-LOG**, **Lh-LG**, **Lh-PCal**, **Lh-rMFG**, **Lh-SFG**, **Lh-SPL**, **Rh-ERC**, Rh-FG, **Rh-iCG**, Rh-LG, **Rh-PHG**, Rh-PCal, **Rh-SFG**, **Rh-TTG**
H (female) – Right Frontal Lobe	Rh-PCG, Rh-caMFG, **Rh-rMFG**, Rh-SFG, Rh-parsT, Rh-parsOP	**Lh-Tha**, **Lh-Acc**, **Lh-ERC**, **Lh-FG**, **Lh-PHG**, **Lh-PaCG**, **Lh-parsO**, Lh-raCG, ***Lh-SFG***, **Lh-TP**, Rh-ERC, **Rh-FG**, **Rh-PHG**, **Rh-TP**, **Rh-Ins, Rh-Pd**, **Rh-Pt**
I (female) – Right Temporal Lobe	Rh-SMG, Rh-bankssts, **Rh-MTG**, Rh-PoCG, Rh-IPL, Rh-STG, Rh-Ins, Rh-TTG	***Lh-bankssts***, **Lh-LG**, **Rh-ERC**, **Rh-LG**, **Rh-PHG**, **Rh-PCal**

Lh – Left hemisphere; Rh – Right hemisphere; G – Gyrus; L- Lobule; C – Cortex.
ITG – inferior temporal; MTG – medial temporal; STG – superior temporal; TTG – transverse temporal; SMG – supramarginal; SPL – superior parietal; IPL – inferior parietal; SFG – superior frontal; LOFC – lateral orbitofrontal; MeOFC – medial orbitofrontal; rMFG – rostral middle frontal; caMFG – caudal middle frontal; LOG – lateral occipital; FG – frontal; TP – temporal; PHG – parahippocampal; pCG – posterior cingulate; iCG – isthmus of the cingulate; caCG – caudal anterior cingulate; raCG – rostral anterior cingulate; PCG – precentral; PoCG – postcentral; PaCG – paracentral; PCal - pericalcarine; parsT – pars triangularis; parsO – pars otbitalis; parsOP – pars opercularis; ERC – entorhinal; PCn – precuneus; Cn – cuneus; bankssts – banks of the superior temporal sulcus; CerebC – cerebellar; Am – amygdala; Pt – putamen; Pd – pallidum; Hip – hippocampus; Ins – insula.

F. Oral Communications and Awards

F.1. Oral Communications

The work developed throughout this thesis gave origin to the following communications:

1. Ana Carina Mendes, Ana-Maria Oros-Peusquens, André Santos Ribeiro, Karl-Josef Langen, Carolin Weiß Lucas, Nadim Jon Shah, Hugo Alexandre Ferreira, "Brain connectivity of glioblastoma patients using MR-PET and DTI data", ISMRM 24th Annual Meeting, 7 to 13 May, 2016, Singapore.

2. A. C. Mendes, A. Santos-Ribeiro, A.-M. Oros-Peusquens, K.-J. Langen, N. J. Shah, H.A. Ferreira, "Brain connectivity study of brain tumor patients using MR-PET data: preliminary results", 4th Conference on PET/MR and SPECT/MR, 17 to 21 May, 2015, Elba, Italy.

F.2. Awards

For the communication in the 24th ISMRM:

- **Magna Cum Laude** - awarded to the top 15% abstracts within a major subject review category.